Master's thesis

NTNU
Norwegian University of Science and Technology
Faculty of Engineering
Department of Marine Technology

Brynhild Resell Igland

Low- and Zero-Emission Hybrid-Electric Power Systems for Passenger Ferries

Master's thesis in Marine Technology
Supervisor: Roger Skjetne
June 2021

NTNU
Norwegian University of
Science and Technology

Brynhild Resell Igland

Low- and Zero-Emission Hybrid-Electric Power Systems for Passenger Ferries

Master's thesis in Marine Technology
Supervisor: Roger Skjetne
June 2021

Norwegian University of Science and Technology
Faculty of Engineering
Department of Marine Technology

NTNU
Norwegian University of
Science and Technology

NTNU Trondheim
Norwegian University of Science and Technology
Department of Marine Technology

MASTER OF TECHNOLOGY THESIS DEFINITION (30 SP)

Name of the candidate:	Igland, Brynhild Resell
Field of study:	Marine cybernetics
Thesis title (Norwegian):	Lav- og nullutslipp hybrid-elektrisk kraft system for passasjerbåter
Thesis title (English):	Low- and zero-emission hybrid-electric power systems for passenger ferries

Background

During the last decade, enabling technologies in energy storage, especially battery-based systems, have resulted in new hybrid-electric and pure battery-electric solutions, in shipboard power systems, to reduce and possibly eliminate fuel consumption and emissions. Mixing diesel-generators and battery energy storage systems (BESS) in a hybrid power system enables various control strategies, such as power smoothing, peak-shaving, strategic loading, start-stop operation of the prime movers, etc. How then to optimally design and operate the power plant to minimize the fuel consumption and the environmental footprint of the vessel have become even more important research questions.

Due to the reliability of the diesel-engine, and its fast response to load changes, this is still the dominating power producer in ships. These advantages cannot be matched well by alternative zero-emission (ZE) power producers such as fuel cells (FCs) or gas-driven engines. This may, however, be mitigated by fast (high power) discharge of energy from BESS during fast load increases in order to ensure voltage and frequency stability of the power bus (under dynamic load variations). It follows that zero- and low-emission hybrid power system architectures are of interest to be explored with respect to technical feasibility and potential for fuel and emission reduction.

In this project, ZE high-speed passenger ferry will be explored w.r.t. power and propulsion solutions. The objectives are to define a relevant case study, consider different power configurations, implement control strategies for zero/low emission, and evaluate the resulting performance and needed capacities.

Scope of Work

1) Perform a background and literature review to provide information and relevant references on:
   - Relevant high-speed passenger ferry applications and technologies, also for ZE operation.
   - Emerging technologies for zero-emission power production in ships, relevant technologies for energy storage, and shoreside charging and refueling systems.
   - Relevant optimization and control of shipboard hybrid power systems, incl. power losses/efficiency, and control strategies for loadsharing.
   - Relevant optimization methods for both offline studies and online optimization.
   - Data on fuel consumption, emissions, efficiencies, and operational constraints of relevant units.

   Write a list with abbreviations and definitions of terms and symbols, relevant to the literature study and project report.
2) Investigate emerging zero-emission power producers for marine electrical systems, such as hydrogen engines, ammonia engines, relevant fuel cell solutions, etc. Give an overview on state-of-the-art and feasibility of the different technologies for selected ship types and operations, as well as development status of the promising solutions. Provide more in-depth details on the most relevant units in terms of working principles, parameters, and features that are important for 1) design of the power system (ratings, weight, volume, need of infrastructure, etc.), and 2) energy and emission optimal control of the equipment (important states, magnitude and rate constraints, SOAs, etc.)
3) Give an overview of relevant BESS products for ships, and provide details important for their design and operation. Describe SoC, DoD, SoH, C-rate, energy efficiency, and SOA.
4) Define a case study in terms of a high-speed passenger ferry: Catamaran and/or hydrofoil vessel (weight, payload capacity, speed), voyage schedule/stages, overall load profile along the stages – incl. acceleration, cruising, deceleration, and slow-speed maneuvering, and required power capacity. Establish a simplified, high-level, numerical model to use for KPI evaluations and analysis. The model should include the main power flow with typical power losses in relevant components.

5) Diesel-Mechanical (DM; baseline model): Specify DM prime mover solution, featured by a single-line-diagram (SLD), incl. weight, volume, power. Define a KPI on fuel consumption and optionally on emissions if data exist on this. Perform computations on the single/multi-stage load profile and plot the KPI trends.
6) Diesel-Electric (DE): Consider using DGs on a DC bus, and compute optimal loadsharing. Evaluate the KPIs on fuel consumption (and emissions) and compare/contrast results with DM baseline.
7) Battery-Electric (BE): Specify a BESS as only power source (show SLD). Model and parameterize the SoC dynamics. Define a KPI on the energy supplied by the battery based on the SoC. Perform computations on the single/multi-stage load profile and plot the trend in SoC. Discuss necessary battery capacity, c-rate, weight, and volume for pure BE operation.
8) Hybrid (Diesel/Battery)-Electric: Design and implement an optimization method enabling strategic loading based on a given load profile. Perform computations on the single/multi-stage load profile and present the trend in fuel and energy KPIs. Study impact on KPIs for varying capacity of BESS. Discuss resulting fuel reductions, weight, and volume.
9) ZE Hybrid-Electric Ship (ZEHES): Study a hybrid combination of FC and BESS as power sources on main bus. Propose loadsharing control strategy for how to keep the FC and battery each within their SOAs. Discuss the optimal sizing of the battery relative to the FC to handle necessary transients and power boosts in the load profile.

Specifications

Every weekend throughout the project period, the candidate shall send a status email to the supervisor and co-advisors, providing two brief bulleted lists: 1) work done recent week, and 2) work planned to be done next week.

The scope of work may prove to be larger than initially anticipated. By the approval from the supervisor, described topics may be deleted or reduced in extent without consequences with regard to grading.

The candidate shall present personal contribution to the resolution of problems within the scope of work. Theories and conclusions should be based on mathematical derivations and logic reasoning identifying the steps in the deduction.

The report shall be organized in a logical structure to give a clear exposition of background, problem/research statement, design/method, analysis, and results. The text should be brief and to the point, with a clear language. Rigorous mathematical deductions and illustrating figures are preferred over lengthy textual descriptions. The report shall have font size 11 pts., and it is not expected to be longer than 70 A4-pages, 100 B5-pages, from introduction to conclusion, unless otherwise agreed. It shall be written in English (preferably US) and contain the elements: Title page, abstract, preface (incl. description of help, resources, and internal and external factors that have affected the project process), acknowledgement, project definition, list of symbols and acronyms, table of contents, introduction (project background/motivation, objectives, scope and delimitations, and contributions), technical background and literature review, problem formulation, method, results and analysis, conclusions with recommendations for further work, references, and optional appendices. Figures, tables, and equations shall be numerated. The original contribution of the candidate and material taken from other sources shall be clearly identified. Work from other sources shall be properly acknowledged using quotations and a Harvard citation style (e.g. natbib Latex package). The work is expected to be conducted in an honest and ethical manner, without any sort of plagiarism and misconduct, which is taken very seriously by the university and will result in consequences. NTNU can use the results freely in research and teaching by proper referencing, unless otherwise agreed.

The thesis shall be submitted with an electronic copy to the main supervisor and department according to NTNU administrative procedures. The final revised version of this thesis definition shall be included after the title page. Computer code, pictures, videos, dataseries, etc., shall be included electronically with the report.

Start date: 15 January, 2021 **Due date:** As specified by the administration.
Supervisor: Roger Skjetne
Co-advisor(s): John Martin Godø and Daeseong Park

Signature: Roger Skjetne

Digitally signed by rskjetne
Date: 2021.06.09 11:26:29 +02'00'

Preface

This thesis constitutes the concluding submission of my master's degree in Marine Cybernetics written at the Norwegian University of Science and Technology (NTNU) in the spring of 2021. The work is a continuation of my project thesis from the fall of 2020.

The thesis is motivated by the need to reduce the environmental footprint of the maritime industry. With this in mind and an interest in marine power systems, I was inspired to write a thesis working towards low- and zero-emission solutions for high-speed passenger ferries, which have a significant emission intensity. The main focus has been selecting optimal dimensions of the power sources and energy storage devices in different power plant configurations and optimization of the loadsharing.

I have found it inspirational working with the novel and fast-developing fields of maritime power system technology. However, one challenge I have faced working with emerging low- and zero-emission technologies is the restricted access to relevant data. Thus, most of the data considering fuel cells and ammonia engines used in this thesis are approximate values based on general characteristics or information from people in the industry.

The work direction and ambition of the thesis have been shaped together with Professor Roger Skjetne, my supervisor. Professor Skjetne has provided clear guidelines that have contributed to structured progress, and our constructive discussions have been valuable for the development of the thesis. John Martin Kleven Godø has provided insight into important aspects concerning high-speed passenger ferries. Daeseong Park has been a helpful discussion partner whenever I have encountered problems in my optimization code.

The work has been conducted during the ongoing pandemic Covid-19. This has affected the guidance meetings with supervisor, which have all been held digitally. For the most part, this has been unproblematic, but I believe that physical meetings may have a more efficient outcome, and it is easier to obtain a common understanding. With some unpredictable conditions in the form of local and national regulations, I am grateful that I have had the opportunity to stay on campus for most of the semester. This has given me the opportunity to communicate with other students whenever small questions have arisen.

Brynhild Resell Igland
Trondheim, June 10, 2021

Aknowledgements

First and foremost, I would like to thank Professor Roger Skjetne, my supervisor, for his guidance and support throughout the work of this thesis. Professor Skjetne's genuine interest in the field of study has been inspirational, and valuable clarifications have been given when questions have arisen.

I would also like to thank my co-supervisors, John Martin Kleven Godø and Daeseong Park, and Associate Professor Mehdi Zadeh for insightful discussions and good advice along the way.

I am grateful for the help and interest shown by people in the industry. Great thanks are directed to Tore Kallevåg for putting me in touch with relevant resources within zero-emission technologies. Further, Egil Hystad and Kaj Portin in Wärtsilä and Tjalve Magnusson Svendsen in Prototech are offered thanks for providing information on their work related to zero-emission power sources. Also, I would like to thank Paal Erlend Strand and Ørjan Flenstad in FosenNamsos Sjø for providing relevant data on Trondheimsfjord I, which has been essential in the case study.

I want to thank my dear friends whom I have shared an office with the previous year. Thank you for many pleasant moments and good memories both in the office and at other social events. Also, my friend Jon Magnus Moen deserves gratitude for his good inputs when revising the thesis draft. Lastly, I would like to thank my family for their unconditional love and support.

Abstract

The maritime industry has been encouraged to significantly reduce its greenhouse gas emissions, aiming for a 50% emission reduction by 2050 compared to 2008 levels. This motivates exploring novel low- and zero-emission technologies and the fields of optimization and control of hybrid-electric marine power systems. One critical vessel type is the high-speed passenger ferries, which have the largest energy consumption and emissions per passenger distance compared to passenger cars and airplanes. Based on the need for reduced emissions, the feasibility of obtaining low- and zero-emission solutions for high-speed passenger ferries is explored.

This thesis presents a state-of-the-art overview of emerging low- and zero-emission technologies. It provides an in-depth study of ammonia engines, proton exchange membrane (PEM) fuel cells, and batteries. This involves the design specifications of these power sources and energy storage devices, including dimensions, capacities, and operational constraints. However, due to the immature technical development of ammonia engines, they are not considered further in the thesis.

Concerning diesel- and hybrid-electric power configurations, fuel reductions can be obtained through optimal loadsharing. In this thesis, high-level models of diesel engines, PEM fuel cells, and batteries are defined. The models are simplified, only concerning power transmission, and are established for implementation in energy optimization algorithms. The proposed energy optimization problems utilized in this thesis are: linear optimization with the objective of minimizing specific fuel consumption, and nonlinear optimization with the objective of minimizing fuel consumption. The problems are defined for both instantaneous optimization and optimization over a horizon.

A case study is conducted where the high-speed passenger ferry Trondheimsfjord I is used as a baseline. With knowledge of the engine configuration and route table, a synthetic load profile is established. From the estimated load demand, the alternative power configurations are defined. The alternatives evaluated are diesel-electric, battery-electric, hybrid-electric, and zero-emission hybrid-electric power plants. Key performance indicators are defined for performance evaluation and analysis concerning fuel consumption, weight, and volume. The battery-electric dimensioning problem yielded a large weight and volume increase. The hybrid-electric power system showed promising results from nonlinear optimization over a horizon with the objective to minimize the fuel consumption, yielding the best performance among the power systems involving a diesel engine. The zero-emission hybrid-electric power system also showed good results regarding weight, but the low energy density is a major drawback concerning fuel tank volume.

Sammendrag

Den maritime industrien er blitt oppfordret til å redusere klimagassutslippene betydelig, med et mål om en reduksjon på 50% innen 2050 sammenliknet med 2008-nivåene. Dette har oppmuntret til utvikling av nye lav- og nullutslippsteknologier og optimerings- og reguleringsalgoritmer innen marine hybrid-elektriske kraftsystemer. Høyhastighets passasjerferger, også kalt hurtigbåter, er den fartøytypen som har størst energiforbruk og utslipp per passasjerdistanse sammenliknet med personbiler og fly. Basert på behovet for reduserte utslipp, undersøkes mulighetene for å realisere lav- og nullutslippsløsninger for høyhastighets passasjerferger.

Denne rapporten presenterer en oversikt over lav- og nullutslippsteknologier. Her er ammoniakkmotorer, protonledende mebran (PEM) brenselceller og batterier studert i detalj. Dette involverer kraftprodusentenes og energilagringsenhetenes designspesifikasjoner, inkludert dimensjoner, kapasitet og operasjonelle begrensninger. På grunn av at teknologien rundt amoniakkmotorer er umoden, blir ikke dette arbeidet med videre i oppgaven.

Når det gjelder diesel- og hybrid-elektriske kraftkonfigurasjoner kan drivstoffreduksjon oppnås ved optimal lastdeling. I denne oppgaven er modeller av dieselmotorer, PEM-brenselceller og batterier definert på høynivå. Modellene er forenklet og tar kun hensyn til effekt. De etablerte modellene kan implementeres i algoritmer for energioptimering. De foreslåtte optimeringsproblemene som brukes i denne oppgaven er: lineær optimering med objektivfunksjon som minimerer spesifikt drivstofforbruk og ulineær optimering med mål om å minimere drivstofforbruk. Problemene er definert for både momentan optimering og optimering over en tidshorisont.

En casestudie er gjennomført med grunnlag i høyhastighetspassasjerfergen Trondheimsfjord I. Med kunnskap om motorkonfigurasjonen og rutetabellen, etableres en syntetisk lastprofil. Fra estimert kraftbehov defineres alternative kraftsystemer. Kraftsystemalternativene som blir vurdert er diesel-elektrisk, batteri-elektrisk, hybrid-elektrisk og nullutslipps hybrid-elektrisk. Ytelsesindikatorer blir definert med hensyn på evaluering og analyse av drivstofforbruk, vekt og volum. Dimensjoneringsstudiet for batteri-elektrisk kraftsystem ga en stor vekt- og volumøkning sammenliknet med det konvensjonelle kraftsystemet. I den ulineære optimeringen over en tidshorisont, viste det hybrid-elektriske kraftsystemet lovende resultater. Blant kraftsystemene som involverte en dieselmotor hadde den best ytelse med hensyn på drivstofforbruk. Det hybrid-elektriske kraftsystemet for nullutslipp viste også gode resultater med tanke på vekt, men den lave energitettheten til hydrogen medfører en stor utfordring når det gjelder tankvolum for drivstoff.

Table of Contents

Preface i

Aknowledgements ii

Abstract iii

Sammendrag iv

Table of Contents vii

List of Figures x

List of Tables xi

Abbreviations xiii

1 Introduction 1
- 1.1 Background and Motivation . . . 1
- 1.2 Objectives . . . 2
- 1.3 Scope and Delimitations . . . 2
- 1.4 Contributions . . . 3
- 1.5 Thesis Outline . . . 3

2 Background and Literature 5
- 2.1 High-Speed Passenger Ferries . . . 5
- 2.2 Maritime Zero-Emission Technologies . . . 7
  - 2.2.1 Future Fuel Types . . . 8
  - 2.2.2 Fuel Infrastructure . . . 9
- 2.3 Energy Storage Technologies . . . 10
  - 2.3.1 Shore-to-Ship Charging . . . 12
  - 2.3.2 Relevant Ship Projects . . . 13
- 2.4 Optimization and Control . . . 13
  - 2.4.1 Power Management System . . . 13
  - 2.4.2 Battery Management System . . . 14
  - 2.4.3 Energy and Emission Management System . . . 14
  - 2.4.4 Vessel Mission Management System . . . 15
  - 2.4.5 Optimization Strategies to Minimize Energy Consumption and Gas Emissions . . . 15
- 2.5 Optimization Methods . . . 16

2.5.1 Interior-Point Method . . . 16
2.5.2 Genetic Algorithm . . . 19
2.5.3 Model Predictive Control . . . 20
2.6 Data for Hybrid-Electric Power Systems . . . 22
2.6.1 Specific Fuel Consumption . . . 23
2.6.2 Typical Losses in Hybrid-Electric Power Plants . . . 23

3 Emerging Zero-Emission Technologies 25
3.1 Internal Combustion Engines . . . 25
3.1.1 Basic Knowledge . . . 25
3.1.2 Relevant Projects . . . 26
3.1.3 Relevant Products and Characteristics . . . 26
3.1.4 Emissions . . . 27
3.2 Fuel Cells . . . 28
3.2.1 Fuel Cell Technology . . . 28
3.2.2 Efficiency . . . 29
3.2.3 Lifetime . . . 30

4 Battery Energy Storage Systems 31
4.1 Battery Technologies . . . 31
4.1.1 Present Maritime Li-ion Batteries . . . 31
4.1.2 Emerging Solid-State Battery Technology . . . 32
4.2 Battery Working Principles . . . 32
4.2.1 State of Charge . . . 33
4.2.2 Depth of Discharge . . . 33
4.2.3 C-rate . . . 33
4.2.4 Safe Operating Area . . . 34
4.2.5 State of Health . . . 34
4.2.6 Efficiency . . . 35

5 Power Plant Models and Optimization Methods 37
5.1 Genset Model . . . 37
5.1.1 Piecewise Linear SFOC Curve . . . 38
5.1.2 Piecewise Quadratic FOC Curve . . . 38
5.2 Fuel Cell Model . . . 39
5.3 Battery Model . . . 39
5.4 Instantaneous Optimization . . . 40
5.4.1 Genset Optimization . . . 40
5.4.2 Hybrid-Electric Optimization . . . 42
5.5 Optimization Over a Horizon . . . 43
5.5.1 Genset SFOC-Optimization . . . 43
5.5.2 FOC-Optimization . . . 44
5.5.3 Hybrid-Electric Optimization . . . 44
5.5.4 Slack Variables . . . 45

6 Case Study: Trondheimsfjord I 47
6.1 Trondheimsfjord I . . . 47
6.2 Route and Load Profile . . . 48
6.3 Key Performance Indicators . . . 50
6.4 Diesel-Mechanical Power System . . . 50

7 Suggested Power System Alternatives for Trondheimsfjord I **53**
7.1 Diesel-Electric Power System . . . 53
7.1.1 SFOC- and FOC-curves . . . 54
7.1.2 Power Transmission Losses . . . 55
7.2 Battery-Electric Power System . . . 56
7.2.1 Battery Dimensioning Limiting Factors . . . 56
7.2.2 Power Transmission Losses . . . 59
7.3 Hybrid-Electric Power System . . . 59
7.3.1 Power Transmission Losses . . . 60
7.4 Zero-Emission Hybrid-Electric Power System . . . 61
7.4.1 Power Transmission Losses . . . 62

8 Results **63**
8.1 Interior-Point Method versus Genetic Algorithm . . . 63
8.2 Instantaneous Optimization Concerning DM and DE Power Systems . . . 65
8.2.1 Equal Loadsharing . . . 65
8.2.2 Variable Speed Optimization . . . 65
8.2.3 Variable-Speed Optimization Considering Component Losses . . . 66
8.3 Battery-Electric Power System Dimensions . . . 67
8.3.1 Single-Stage Load Profile . . . 67
8.3.2 Multi-Stage Load Profile . . . 69
8.4 Optimization Over a Horizon Concerning DE, HE, and ZEHE Power Systems . . . 71
8.4.1 Diesel-Electric . . . 71
8.4.2 Hybrid-Electric . . . 72
8.4.3 Zero-Emission Hybrid-Electric . . . 73
8.4.4 Total Fuel Consumption . . . 74
8.5 Weight and Volume of the Power Systems . . . 75

9 Analysis and Discussion **77**
9.1 Solver Selection . . . 77
9.2 Conversion to Diesel-Electric High-Speed Passenger Ferries . . . 77
9.3 Analysis of Battery Dimensions . . . 78
9.4 Performance of the Optimization Over a Horizon . . . 78
9.5 Weight and Volume Considerations . . . 80

10 Conclusion **81**
10.1 Concluding remarks . . . 81
10.2 Recommendations for Further Work . . . 82

Bibliography **83**

Appendix **I**
A Example of Hybrid-Electric Power System Model . . . I
A.1 Instantaneous optimization . . . I
A.2 Example of Optimization Over a Horizon . . . I
B Matlab Code . . . III
B.1 Hybrid-Electric Power System: FOC-Optimization Over a Horizon . . . III
C Specific Fuel Consumption Data . . . IX
C.1 Lookup Tables from Performance Diagram . . . IX
C.2 Fixed Speed SFC Data . . . X
C.3 Specific Hydrogen Consumption . . . X

List of Figures

2.1 Submerged hull, air cushion, and foil supported high-speed vessels (Illustration: Bjarne Stensberg, (Faltinsen, 2005)) . . . 5
2.2 Energy consumption for different means of transport (Courtesy: Godø and Vinje (2019)) 6
2.3 Illustration of one of the Flying Foil vessel solutions (Courtesy: Godø and Vinje (2019)) 6
2.4 Fuel cell system for ships (Courtesy: ABB (2020)) . . . 7
2.5 Alternative fuel types (Illustration: MAN Energy Solutions (2020a)) . . . 8
2.6 Illustration of the ZEEDS initiative (Illustration: Nordic Innovation (2020)) . . . 9
2.7 Hydrogen bunkering vessel design (Courtesy: Wilhelmsen (2019)) . . . 10
2.8 Energy Storage Technologies (Zadeh, 2020a) . . . 11
2.9 Energy vs. Power density of different ESDs (Othman et al., 2019) . . . 12
2.10 Induction charger for ship applications (Courtesy: Wärtsilä (2020b)) . . . 12
2.11 Control layer architecture of an autonomous vessel (Illustration: Reddy et al. (2019)) . . 13
2.12 Main objectives of the EEMS (Courtesy: Reddy et al. (2019)) . . . 14
2.13 GA optimization (Illustration: Deland (2015)) . . . 19
2.14 Bit-string crossover (Courtesy: Sivanandam and Deepa (2008)) . . . 20
2.15 Bit-string mutation (Courtesy: Sivanandam and Deepa (2008)) . . . 20
2.16 Principle of MPC (Illustration: Foss and Heirung (2016)) . . . 21
2.17 Specific fuel consumption curves . . . 23
2.18 Power efficiencies in a DE power plant (Illustration: Zadeh (2020a)) . . . 24
2.19 Converter efficiencies as a function of output power (Courtesy: Ghimire et al. (2019)) . . 24

3.1 Ammonia classifications (DNV GL, 2020) . . . 25
3.2 Wärtsilä's engine for chamber tests (Courtesy: Wärtsilä (2020d)) . . . 26
3.3 Fuel cell illustration (Illustration: Prototech (2020)) . . . 28
3.4 Chemical flow in a fuel cell (Illustration: ABB (2020)) . . . 28
3.5 Theoretical and real efficiency as a function of temperature for PEMFC systems (Courtesy: Wenzl (2009)) . . . 30
3.6 PEMFC system efficiency curve compared to an ICE and a single FC stack (Courtesy: Wenzl (2009)) . . . 30

4.1 Cycle life as function of DOD for NMC-batteries (Courtesy: Godø and Vinje (2019)) . . 33
4.2 Battery SOA (Andrea, 2010) . . . 34

6.1 Trondheimsfjord I (Marine Traffic, 2021) . . . 47
6.2 Route of operation for Trondheimsfjord I (Marine Traffic, 2021) . . . 48
6.3 Synthetic load profiles . . . 49
6.4 Single-stage load profile for mission guidance . . . 50

6.5 SLD of diesel-mechanical configuration 51
6.6 Load and engine speed profiles 51

7.1 SLD of diesel-electric configuration 53
7.2 Fixed-speed fuel consumption curve 54
7.3 Contour plot illustrating loadsharing for fixed speed SFOC-curve 55
7.4 Variable speed SFOC- and FOC-curves 55
7.5 Load profiles for battery dimensioning 56
7.6 SLD of battery-electric configuration with Corvus Dolphin Energy packs 58
7.7 SLD of battery-electric configuration with Corvus Dolphin Power packs 58
7.8 SLD of hybrid-electric configuration 60
7.9 SLD of Zero-Emission Hybrid-Electric Configuration 61

8.1 Fixed-speed optimization with interior-point algorithm 63
8.2 Zoomed in view of fixed-speed optimization with interior-point algorithm 64
8.3 Fixed-speed optimization with genetic algorithm 64
8.4 Equal loadsharing concerning single- and multi-stage load profiles 65
8.5 Variable speed optimization with interior-point algorithm 66
8.6 Variable speed optimization considering losses 66
8.7 SOC-plot of the feasible BESS configurations for single-stage load profile 68
8.8 SOC-plot of the feasible BESS configurations for single-stage load profile concerning losses 69
8.9 SOC-plot of the feasible BESS configurations for multi-stage load profile 70
8.10 Diesel-electric SFOC-optimization over a horizon 71
8.11 Diesel-electric FOC-optimization over a horizon 72
8.12 Hybrid-electric SFOC-optimization over a horizon 72
8.13 Hybrid-electric FOC-optimization over a horizon 73
8.14 Zero-emission diesel-electric SFOC-optimization over a horizon 74
8.15 Zero-emission hybrid-electric FOC-optimization over a horizon 74

List of Tables

2.1 Typical properties of ESDs used in marine applications (Mutarraf et al., 2018) 11

3.1 Engine specifications of Wärtsilä's 6L34DF engine (Wärtsilä, 2020c) 27
3.2 Energy density of ammonia compared to diesel 27
3.3 Comparison of SOFC and PEMFC 29
3.4 Energy density of hydrogen compared to ammonia and diesel 29

4.1 Comparison of battery characteristics 31

5.1 Control input parameters 37

6.1 Trondheimsfjord I: Design parameters (Brødrene Aa (2021), MTU (2019)) 48
6.2 MTU 12V 2000 M72 Specifications (MTU, 2019) 48
6.3 Voyage schedule for Trondheimsfjord I (AtB, 2021) 49
6.4 Load profile characteristics 49

7.1 Case specific parameter values for DE power system 54
7.2 Component losses in DE power system 56
7.3 BESS specifications 57
7.4 Component losses in BE power system 59
7.5 Case specific parameter values for BE power system 59
7.6 Ballard FCWave specifications 61
7.7 Case specific parameter values for ZEHE power system 62

8.1 Total fuel consumption for diesel-mechanical power system 65
8.2 Total fuel consumption for diesel-electric power system 67
8.3 Battery systems satisfying energy demand 67
8.4 Battery systems satisfying power demand 68
8.5 Battery systems satisfying energy demand concerning losses 68
8.6 Battery systems satisfying power demand concerning losses 69
8.7 Battery systems satisfying energy demand 70
8.8 Battery systems satisfying energy demand concerning losses 71
8.9 Resulting fuel consumption from optimization over a horizon with SFOC-curve for fixed-speed configuration 74
8.10 Weight and Volume of the Power Systems 75

Abbreviations

AC	=	Alternating Current
BE	=	Battery-Electric
BESS	=	Battery Energy Storage System
BMS	=	Battery Management System
C-rate	=	Charge/Discharge Rate
DC	=	Direct Current
DE	=	Diesel-Electric
DM	=	Diesel-Mechanical
DP	=	Dynamic Positioning
EEMS	=	Energy and Emission Management System
EPV	=	Energy Providing Bunkering Vessel
ESD	=	Energy Storage Device
ESS	=	Energy Storage System
FC	=	Fuel Cell or Fuel Consumption
FOC	=	Fuel Oil Consumption
GA	=	Genetic Algorithm
Genset	=	Generator Set
GHG	=	Greenhouse Gas
HE	=	Hybrid-Electric
HSPF	=	High-Speed Passenger Ferry
ICE	=	Internal Combustion Engine
IP	=	Interior-Point Method
KPI	=	Key Performance Indicator
Li-ion	=	Lithium-Ion
LNG	=	Liquefied Natural Gas
LP	=	Linear Programming
MCR	=	Maximum Continuous Rating
MGO	=	Marine Gas Oil
MILP	=	Mixed-Integer Linear Programming
MPC	=	Model Predictive Control
NH_3	=	Chemical Formula for Ammonia
NLP	=	Nonlinear Programming
OSV	=	Offshore Support Vessel
PEMFC	=	Proton Exchange Membrane Fuel Cell
PMS	=	Power Management System
PWL	=	Piecewise Linear
SFC/SFOC	=	Specific Fuel (Oil) Consumption
SLD	=	Single-Line Diagram
SOA	=	Safe Operating Area
SOC	=	State of Charge
SOFC	=	Solid Oxide Fuel Cell
SOH	=	State of Health
VMMS	=	Vessel Mission Management System
ZE	=	Zero Emission
ZEHES	=	Zero Emission Hybrid-Electric Ship

Chapter 1

Introduction

The project's background and motivation are outlined herein. Further, the objectives, scope and delimitations, contributions, and structure are defined.

1.1 Background and Motivation

In 2016 the Paris Agreement entered into force, aiming to keep the global temperature rise below two degrees Celsius compared to pre-industrial levels (UNFCCC, 2020). As a contribution to lowering greenhouse gas (GHG) emissions, the International Maritime Organization (IMO) has introduced an "Initial strategy on reduction of GHG emissions from ships". One of the ambitions of the strategy is to reduce GHG emissions by 50% by 2050 compared to 2008 levels (IMO, 2020). In addition to global measures, regulations such as carbon taxes and emission control areas are examples of local regulations. These regulations encourage the maritime industry to develop low- and zero-emission (ZE) technologies utilizing alternative fuels and hybrid power system architectures.

The development of energy storage technologies has improved significantly during the last decade, enabling new hybrid-electric power system solutions. This has resulted in hybrid-electric and battery-electric vessels with reduction, or even elimination, of fuel consumption and emissions. Here, hybrid means that two or more different power sources and energy storage devices are installed in the power system. The hybridization of power systems has enabled the implementation of control strategies to optimally configure the connection of power producers and energy storage devices (ESDs) and optimal loadsharing among these. The control algorithms are implemented to enhance the performance of the shipboard power plant. In the energy and emission management system (EEMS), a typical aim is to optimize fuel consumption and emissions. When encountering dynamically demanding loads, the power management system (PMS) overrules the EEMS to ensure enough power is provided to avoid blackout. Including a vessel mission management system (VMMS), a predicted load profile can be provided as input to the EEMS control algorithms, which can improve the connection scheduling and loadsharing further. Optimal utilization of the onboard power system is also important from a shipowner's view since it reduces operational and maintenance costs.

Improvements of the battery energy storage system (BESS) properties ensure high power density, providing a fast response to rapid load changes. This enables the utilization of power sources with slower dynamics, such as fuel cells and gas engines, in a hybrid configuration. Hence, the zero-emission hybrid-electric ships (ZEHESs) can match the reliability of conventional ships with diesel-engine propulsion.

High-speed passenger ferries (HSPF) have the largest energy consumption and emissions per passenger distance among all transport alternatives. This encourages the development of enhanced high-speed passenger ferry power systems, aiming for low- or zero-emission solutions.

1.2 Objectives

Based on the need for lower fuel consumption and reduced emissions, the feasibility of obtaining low- and zero-emission solutions for high-speed passenger ferries is explored. Through energy optimization with different key performance indicators (KPIs), a performance analysis is conducted. In order to evaluate the feasibility, the following list presents the main objectives of the thesis:

- Review literature within emerging ZE power producers and energy storage systems and novel optimization-based algorithms for energy management control.
- Define a case study in terms of an HSPF to consider different power plant configurations and implement algorithms for energy optimization.
- Evaluate the performance of the energy optimization and needed capacities to have a feasible low/zero-emission solution.

1.3 Scope and Delimitations

The scope of work involves performing a literature review and obtaining relevant references on high-speed passenger ferry applications and technologies, emerging ZE technologies, and energy storage technologies, as well as performing a background study of control strategies for loadsharing in hybrid-electric ships and optimization methods for energy control. Further, relevant data for hybrid-electric power systems are presented.

By investigating emerging ZE technologies for marine power systems, a state-of-the-art overview is provided. For the promising solutions, a more in-depth study is provided. This involves studying the specifications of these power producers, including dimensions, capacities, and operational constraints. A similar investigation is conducted for BESSs.

In the case study, the high-speed passenger ferry Trondheimsfjord I is used as a baseline. With knowledge of the engine configuration and route table, a synthetic load profile is established. From the known load demand, the alternative power configurations are defined. The alternatives evaluated are diesel-electric (DE), battery-electric (BE), hybrid-electric (HE), and zero-emission hybrid-electric power plants. A high-level, simplified power system model is established for implementation in energy optimization algorithms for each alternative. The KPIs are defined for performance evaluation and analysis.

Some of the delimitations of the project are:

- Ammonia and hydrogen are the only fuel alternatives considered for a more in-depth description.
- Ammonia engines and solid oxide fuel cells (SOFCs) are still under development, yielding only approximate characteristics.
- Hydrogen and battery are the only fuel and ESD alternatives considered in the case study.
- The power plants considered in the case study are simplified, only considering active power. Further, the component efficiencies are included as constant factors, not concerning the realistic curves depending on the power output. Degradation of the fuel cells and batteries is not considered in the optimization.

- The specific fuel oil consumption (SFOC) curves are approximated from a piecewise linearization between measured datapoints. The SFOC-curves of the MTU engine are based on datapoints obtained manually from a performance diagram.

1.4 Contributions

The contributions in this project are:

- An insight into the state-of-the-art of emerging zero-emission technologies.
- An overview of control and optimization approaches in marine vessel power systems.
- High-level models of marine power system alternatives.
- Optimization algorithms for loadsharing in hybrid-electric power plants.

1.5 Thesis Outline

The remaining report is divided into nine chapters, which are briefly described below.

- **Chapter 2:** Provides information and relevant references on high-speed passenger ferry applications and technologies, zero-emission and energy storage technologies, optimization and control strategies of shipboard hybrid power systems, and relevant data for hybrid-electric applications.
- **Chapter 3:** Presents state-of-the-art of relevant zero-emission power producers for ship application, providing more in-depth details on design and control parameters.
- **Chapter 4:** Gives an overview of battery energy storage systems, their working principles, and important properties for design and operation.
- **Chapter 5:** Introduces the models and optimization problem formulations used to optimize the loadsharing in different power plant configurations with the aim to reduce fuel consumption. The models established are high-level, simplified models concerning power transmission. The optimization problems concern both linear SFOC-optimization and nonlinear FOC-consumption, and are defined for both a single load instance and multiple instances over a horizon.
- **Chapter 6:** A case study is defined in terms of a high-speed passenger ferry with a fixed voyage schedule. The vessel Trondheimsfjord I is chosen for the case study, with diesel-mechanical propulsion as a basis. First, the design properties are presented, and the route-specific load profiles are synthesized. Then, the power configuration is presented in an SLD. Finally, based on the load profile, an engine speed profile is defined to enable fuel consumption calculations.
- **Chapter 7:** Presents the alternative power plant configurations suggested to replace the conventional DM solution in Trondheimsfjord I and the power transmission losses related to these.
- **Chapter 8:** Presents the results from the different methods of optimization and the results from the design calculations for battery-electric configuration. First, the instantaneous FOC-optimization was run for the diesel-electric power system with two different solvers to test their performance. The best performing solver was selected for the other optimizations. Then, the fuel consumption of the conventional configuration and the diesel-electric power system were calculated for a short, single-stage load profile. Subsequently, the battery dimensions were calculated for the battery-electric power system concerning both a single-stage and a multi-stage load profile. Lastly, the SFOC- and FOC-optimization results over a horizon for the DE, HE, and ZEHE configurations with a fixed-speed SFOC-curve were calculated.

- **Chapter 9:** Presents the analysis and discussion of the results from the previous chapter.
- **Chapter 10:** Presents conclusion and proposal for further work.

Chapter 2

Background and Literature

In this chapter, information and relevant references on high-speed passenger ferry applications and technologies are presented. Further, zero-emission and energy storage technologies and optimization and control strategies of shipboard hybrid power systems are outlined. Lastly, data of relevant applications are provided. Parts of this chapter are based on my project thesis (Igland, 2020), written at NTNU in the autumn of 2020 as a prestudy for this master thesis.

2.1 High-Speed Passenger Ferries

There are three main categories of high-speed marine vehicles; vessels supported by submerged hulls, air cushions, or foils, as shown in Figure 2.1. The most common high-speed craft for passenger transportation is the catamaran. Typically, the vessels are 30-40 meters long, have a transom stern and a center of gravity at approximately 40-48 % of the length between perpendiculars from the stern (Faltinsen, 2005). Compared to the hydrofoil vessels, the catamaran construction is simple. In the '80s, their energy consumption was significantly reduced, which had been the main drawback compared to the hydrofoil vessels. Due to this, the catamarans overtook the high-speed passenger ferry market, and the development of hydrofoil vessels stagnated (Godø and Vinje, 2019).

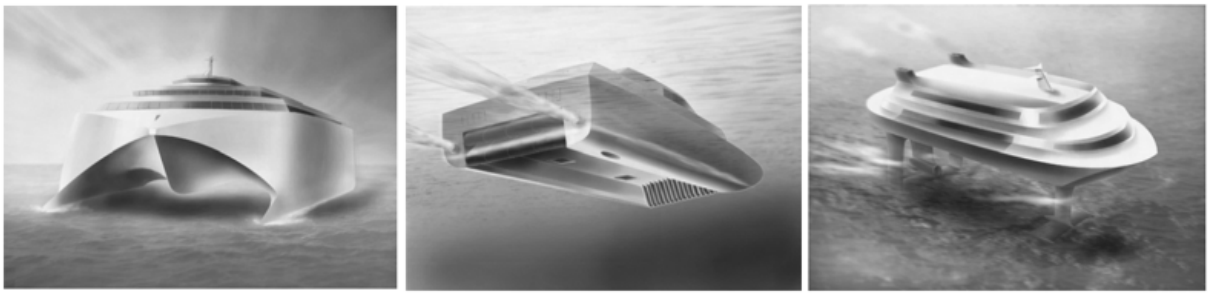

Figure 2.1: Submerged hull, air cushion, and foil supported high-speed vessels (Illustration: Bjarne Stensberg, (Faltinsen, 2005))

One of the main challenges concerning high-speed passenger ferries is their high energy consumption per passenger distance. Figure 2.2 illustrates the energy consumption of different means of transport. It shows that the catamaran consumes approximately 50% more energy than the airplane and 300% more than a passenger car. This implies that with a conventional diesel-mechanical propulsion system, the emissions per passenger distance also are high. This encourages the development of enhanced high-speed passenger ferry power systems, aiming for low- or zero-emission solutions.

Figure 2.2: Energy consumption for different means of transport (Courtesy: Godø and Vinje (2019))

In 2017, the Trøndelag county council announced a project aiming to develop zero-emission solutions for the high-speed passenger ferry routes in the county (Miljødirektoratet, 2019). One of the participating companies was Flying Foil AS, which suggested two battery-electric hydrofoil vessels as a solution to the project. The suggested design of the vessels is illustrated in Figure 2.3. As specified in the report, HSPFs are extremely weight-sensitive, and the energy consumption is directly related to weight changes. Hence, the weight-energy relation must be carefully considered. Two important factors of the project solution are a large reduction in energy consumption by the reduced resistance related to the hydrofoil vessel and increased speed to release time for charging while maintaining the current schedule. The reduced energy consumption is essential when a ZE solution is considered due to the fact that the systems are heavier per energy unit compared to the standard diesel-mechanical system. The report concludes that both hydrogen and battery systems are feasible power solutions both for conventional and hydrofoil vessels. It is mainly a question of expenses (Godø and Vinje, 2019).

Figure 2.3: Illustration of one of the Flying Foil vessel solutions (Courtesy: Godø and Vinje (2019))

A study done by IFE (Aarskog and Danebergs, 2020) maps the feasibility of zero-emission solutions for 96 routes in the Norwegian HSPF sector towards 2030. In the study, battery solutions are considered preferred as long as it is technically viable. Otherwise, a hydrogen solution should be applied. The study concludes that out of the routes investigated, 30 could be powered by batteries and 51 of them by hydrogen. The remaining 15 routes were not applicable due to intermittent routes or very low fuel consumption.

Another relevant project is ZEVS (2021), enabling zero-emission passenger vessel services. It is an interdisciplinary project aiming to create knowledge and expertise related to zero-emission passenger vessels through mapping the technological and economic feasibility, infrastructural obstacles, and wel-

fare effects. The overall objective of the project is to fill research gaps of ZE passenger vessels while providing needed resources for decision-makers. One of the work packages involves estimating energy use and emissions in a prediction model, considering both existing and future high-speed ferries.

2.2 Maritime Zero-Emission Technologies

Due to the increasing demand for a greener maritime industry, research and development of zero-emission technologies have become a large field of interest. Dependent on the operational profile of the maritime vessels, various zero-emission solutions may be applied. Fuel cells, ammonia engines, and batteries are examples of power sources and energy storage devices that can be installed in a shipboard power system to achieve low- and zero-emission operations.

There are already battery-electric ferries operating along the coast of Norway, implying short-distance zero-emission vessel's feasibility. However, batteries have a high gravimetric density and are too heavy to provide enough power for long-distance shipping alone (CPNETZEROSHIP, 2020). Among the emerging development of other low-emission power sources, there is an uncertainty of which solution will be the preferred one in the future. Since risk mitigation is an important factor for a shipowner, this uncertainty discourages investment in new ships, as the vessel should last for 20-30 years. The uncertainty is connected to local infrastructure, fuel availability, storage technology, and flexibility of the energy converters.

As part of the development of zero-emission technologies, MAN Energy Solutions (2020c) is developing a two-stroke ammonia engine. The engine will go through engine tests in 2021, and delivery of the first ammonia engine to yard is scheduled to 2024. In September 2021, Wärtsilä (2020d) will test an internal combustion engine fueled by ammonia, which will go through field tests in ship applications in 2022.

Proton exchange membrane fuel cells (PEMFCs) are among the technologies under development for shipboard power supply. Figure 2.4 illustrates the conceptual fuel cell solution proposed by ABB (2020). The system utilizes PEM fuel cells fueled by hydrogen, which can be included in a hybrid arrangement with batteries or engines to obtain a wider application range. Further description of ammonia engines and fuel cells will be covered in Chapter 3.

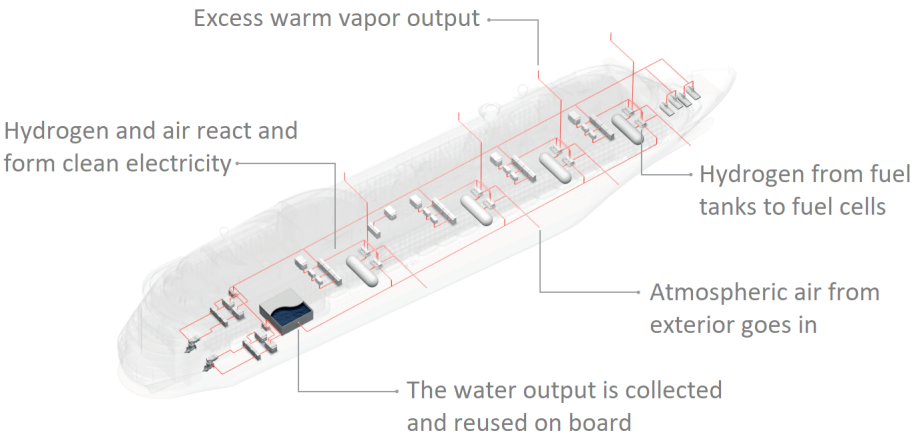

Figure 2.4: Fuel cell system for ships (Courtesy: ABB (2020))

Two relevant fuel cell projects are related to the Norwegian-owned vessels Viking Energy and MF Hidle. ShipFC is a collaborative project coordinated by NCE Maritime CleanTech. The platform supply vessel Viking Energy, owned by Eidesvik, will go through a retrofit to operate on ammonia fuel cells. After the retrofit, the vessel should be ready for zero-emission deep-sea operation. The fuel cells will be developed by Prototech and are supposed to provide 2MW by 2024. Viking Energy already has a battery installed, with a capacity of 653 kWh (Eidesvik, 2020). The FLAGSHIPS project concerning contributes to the development of a hydrogen ferry, MF Hidle, supposed to operate in Stavanger. The vessel is owned by Norled and is currently under construction in Turkey at ADA Yard (FLAGSHIPS, 2020). The power system will consist of three fuel cell modules of 200 kW, supplied by Ballard Power Systems Europe.

2.2.1 Future Fuel Types

Figure 2.5: Alternative fuel types (Illustration: MAN Energy Solutions (2020a))

Figure 2.5 illustrates the possible future fuels either suited for two-stroke combustion, four-stroke combustion, or both. Each fuel's main advantages and challenges are listed below. Some of the fuels are not emission-free but are relevant as a bridging fuel in the energy transition or due to better availability (MAN Energy Solutions, 2020a).

- **Ammonia (NH_3):** A synthetic fuel with no CO_2-emissions from combustion. Needs pilot fuel for ignition.
- **Biofuel:** Fuel produced from biomass, considered fully renewable. It is mixed with fossil fuels, which reduce emissions. Bacterial growth is an issue if the fuel interacts with water.
- **Hydrogen (H_2):** A fuel with high specific energy and no GHG emissions from combustion. It needs to be compressed at 350-700 bar or liquefied at -253 °C.
- **LNG:** A low-emission, clean-burning fossil fuel, which is liquefied at -162°C. The fuel is methane-based, which requires management of potential methane slip.
- **SNG/Biogas:** A low-emission fuel, considered as a good bridging fuel in the energy transition. A challenge, however, is the bunker fuel availability.
- **LPG:** An energy-dense fuel containing no sulfur. The fuel is relatively easy to store. Better energy density, but more emissions, compared to LNG.
- **Methanol (CH_3OH):** A clean-burning liquid fuel that can be produced from renewable energy. It can be stored at ambient conditions. The fuel has a low ignition point, below ship safety regulations.
- **Synthetic diesel:** Fuel made by reconfiguration of hydrocarbon fuels, such as LNG. This provides a cleaner-burning than crude-oil diesel. A challenge is the availability as a large-scale bunker fuel.

In this thesis, only ammonia and hydrogen are studied in more detail due to the current development within the fields of these fuels.

2.2.2 Fuel Infrastructure

Concerning ammonia and hydrogen, there is a need for technological development of refueling and storage systems in order to establish a sustainable expansion of these zero-emission solutions. In addition to ensuring green production, i.e., using renewable energy in the production phase, transport and storage logistics are the main challenges to using hydrogen and ammonia as fuels.

Ammonia Infrastructure

According to Yara Norge (2020) ammonia is mainly produced from natural gas, i.e., brown ammonia. This means that there is still a need to improve ammonia production to consider it a zero-emission fuel. One of the advantages concerning ammonia as a fuel is that there are already large quantities of ammonia transported around the world, implying that an infrastructure exists (MAN Energy Solutions, 2020b). Since ammonia can be stored as a liquid at -33 °C in ambient pressure conditions or at 10 bar pressure at ambient temperature, it is anticipated that the storage and refueling will not require advanced technological modifications. However, ammonia is highly corrosive and toxic, and handling requirements and safe storage must be established for marine application.

In February 2021, Yara, Statkraft, and Aker Horizons signed a letter of intent with the aim to establish Europe's first large-scale production of green ammonia (Yara, 2021). The collaboration's first project is to electrify and decarbonize the ammonia production site at Herøya in Norway. With funds from the government, it is anticipated that the project will be realized within 5-7 years.

The ZEEDS initiative has investigated the possibilities of creating an infrastructure for distributing zero-emission fuels by designing offshore production and distribution hubs (Wärtsilä, 2020a). The first concept investigated was an offshore plant for ammonia production and storage. An illustration of the concept is shown in Figure 2.6, which involves a production platform, a wind farm, subsea storage, and energy providing bunkering vessels (EPVs).

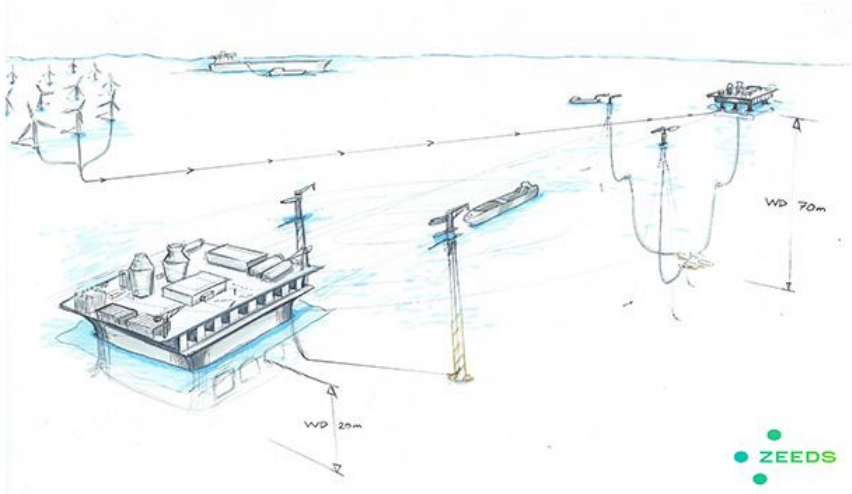

Figure 2.6: Illustration of the ZEEDS initiative (Illustration: Nordic Innovation (2020))

From the wind farm, renewable energy is provided to the platform where ammonia production takes place. The platform is a two-story plant, where hydrogen is produced from electrolysis of water on the first floor. On the second floor, nitrogen is extracted from the air and is utilized to produce ammonia. The ammonia can be stored in fiberglass tanks at 70 meters depth, utilizing seawater for cooling. At this

depth, the ambient pressure ensures that the ammonia is stored as a liquid. Looking at hydrogen storage for comparison would require a storage depth of 8000 meters. A safety concern is keeping most vessels away from the production compound. Hence, EPVs are proposed for ship-to-ship bunkering.

Hydrogen Infrastructure

Today's hydrogen production is mainly from natural gas and is related to land-based infrastructure. However, the main challenges to using hydrogen as a fuel are transport logistics and safe storage. As the relevance of hydrogen as a marine fuel increases, the need for standards and regulations must be developed. Both storage and bunkering need to be taken into account. Liquefied hydrogen can be distributed to ships in large volumes, while pressurized hydrogen is well suited for local production in port (ABB, 2020). According to Hirscher (2010) it is anticipated that refueling time for hydrogen is approximately the same as for diesel. This is a relevant factor considering that the number of voyages depends on the time spent bunkering and loading/unloading at the port.

A limiting factor when investigating hydrogen as a future fuel is its energy density. Hydrogen is very light and has high specific energy. However, the energy density is very low at ambient conditions. Hence, the hydrogen must be liquefied or pressurized to be a fuel option (Hofstad, 2020). Hydrogen is stored as a liquid at -253°C or as a compressed gas at a pressure of 350 to 700 bar. In liquefied form, the hydrogen requires 4.2 times the volume of the marine diesel, while in compressed gas form, it requires about 8 times the volume.

According to DNV GL (2018), hydrogen can be produced locally at port from electrolysis if the local electrical power supply is adequate. This eliminates the current need for hydrogen to be transported over long distances, which implies better availability for hydrogen as a marine fuel. The HyInfra project, led by Arena Ocean Hyway Cluster (2020), investigates future demand, technological solutions, uncertainty, and risks related to marine hydrogen infrastructure. Further, Moss Maritime has developed a liquefied hydrogen bunkering vessel designed to provide merchant ships with liquefied hydrogen (Wilhelmsen, 2019). The vessel design is illustrated in Figure 2.7.

Figure 2.7: Hydrogen bunkering vessel design (Courtesy: Wilhelmsen (2019))

2.3 Energy Storage Technologies

Energy storage devices are installed in a shipboard power plant to enhance the generator set (genset) loadings or to enable zero-emission operations. Through charging and discharging of the ESDs, the gensets can operate at optimal loading or even be disconnected. Hence, the total fuel consumption is reduced. The ESDs can be classified into three main categories: electrical, chemical, and mechanical

energy storage. Further separation and examples of the categories are shown in the figure below.

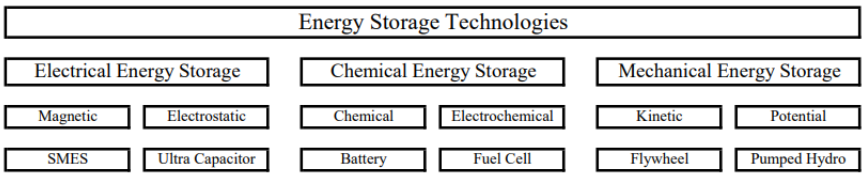

Figure 2.8: Energy Storage Technologies (Zadeh, 2020a)

The characteristics that must be considered when installing an ESD are capacity, charge rates (C-rates), cost and maintenance, expected lifetime, and volume and weight (Skjong et al., 2017). The lifetime can be defined in two ways, calendar lifetime and cycle lifetime. The calendar life describes the lifetime of the ESD in terms of expected calendar years, while cycle life is related to capacity degradation due to the number of charge and discharge cycles. Table 2.1 compares some of the typical characteristics of the most applied ESDs: batteries, capacitors, and flywheels.

Table 2.1: Typical properties of ESDs used in marine applications (Mutarraf et al., 2018)

	Power density [kW/kg]	**Energy density** [kWh/kg]	**Cost** [$/kW]	**Efficiency** [%]	**Calendar lifetime** [years]	**Response time**
Li-ion battery	150-315	75-200	1200-4000	90-97	5-100	[ms]
Flywheel	400-1500	10-30	250-350	90-95	15-20	[ms]-[s]
Super-capacitor	100 000 +	20 +	100-300	85-98	4-12	[ms]

Batteries are the most common ESDs, and with their improving chemistry and cooling solutions, the range of application increases. They are chemical energy storage devices, which can store large amounts of energy. Batteries are suited for energy-intensive applications, have relatively fast dynamics and high specific power. The lifetime of the batteries is also good. However, the batteries have slower dynamics than the supercapacitor (Gundersen and Hansen, 2014).

Supercapacitors have a high dynamic range and are favored for power-intensive applications. They are electrostatic energy storage devices with a large cycle lifetime. Compared to a Li-ion battery, the specific power of a supercapacitor is 10-100 times larger. The supercapacitor's main disadvantage is its low specific energy, from 10-100 times less than a Li-ion battery (Zadeh, 2020b). Supercapacitors also have a shorter calendar life compared to Li-ion batteries (Mutarraf et al., 2018).

Flywheels are rotating devices storing kinetic energy. The energy is stored and provided through the utilization of its moment of inertia. Similar to the supercapacitor, the flywheel is a power-dense device with a low energy density. However, the calendar life of the flywheel is larger than for the supercapacitor (Mutarraf et al., 2018).

Figure 2.9 shows a range of power density compared to energy density for different ESDs and energy sources in a logarithmic scale. It illustrates that the fuel cell has a higher energy density but lower power density than a battery, while the supercapacitor has higher power density and lower energy density. The ESDs should be installed based on functionality demand and provide enhanced performance of the hybrid power system.

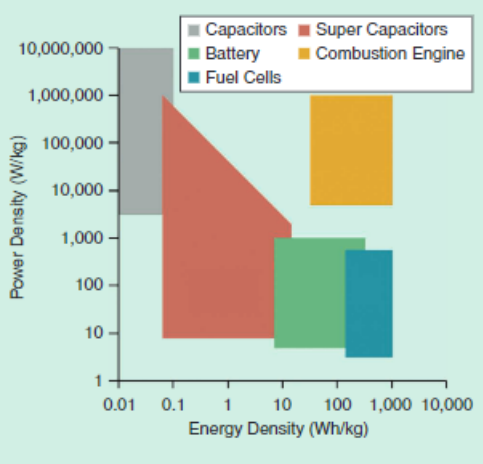

Figure 2.9: Energy vs. Power density of different ESDs (Othman et al., 2019)

2.3.1 Shore-to-Ship Charging

Battery-electric vessels and plug-in hybrids are dependent on shore chargers for energy supply. These chargers can be AC, DC, or wireless chargers (Karimi et al., 2020). Wärtsilä has developed an induction charging system for easy transfer of power from shore to ship, suitable for battery electric vessels with short charging periods during docking. The charger installed to provide power to MF Folgefonn is shown in Figure 2.10.

Figure 2.10: Induction charger for ship applications (Courtesy: Wärtsilä (2020b))

DNV GL (2015b) states that a crucial factor for plug-in hybrid and battery-electric ships is sufficient and reliable power supply. One infrastructural challenge related to the expansion of these types of vessels is the local grid at shore. In some areas, the power delivery is limited, which is a challenge due to the shipboard system's requirement for stable voltages and fixed frequencies. One approach to this issue is to install battery banks at shore to ensure power access when the vessel is docking.

2.3.2 Relevant Ship Projects

We can divide battery-powered ships into battery-electric, plug-in hybrid, and hybrid ships. MF Ampere was the first battery-electric car ferry, built in 2014 (Norled, 2020). In a battery-electric vessel, all onboard power is provided from batteries. In addition to battery storage systems installed in new-build vessels, it is possible to have vessels retrofitted. Two ForSea owned vessels, Tycho Brahe and Aurora, underwent a conversion to battery-electric power. Through the retrofit, the previously diesel engine-operated vessels operate emission-free (ABB, 2018). An example of a plug-in hybrid ship is Color Hybrid, built in 2019 (Ulstein, 2019). A plug-in hybrid ship differs from a hybrid ship due to the possibility to charge the battery by connecting to a charger at shore. In a hybrid ship, another shipboard power supply charges the battery.

2.4 Optimization and Control

The control system of a modern power and propulsion system has several layers, from low-level control, such as governors and automatic voltage regulators on component level, to the user interface, which handles operator commands. Figure 2.11 shows the proposed control layers of an autonomous vessel (Reddy et al., 2019). The different system-level control layers involve the power management system, energy and emission management system, and the vessel mission management system. In power configurations where batteries are involved, a battery management system (BMS) is included in parallel with the PMS.

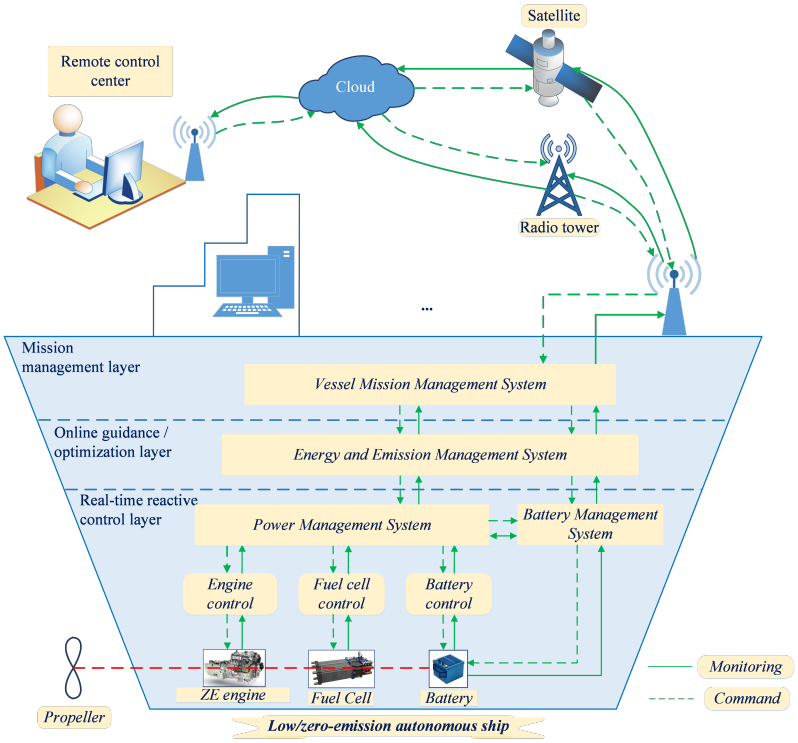

Figure 2.11: Control layer architecture of an autonomous vessel (Illustration: Reddy et al. (2019))

2.4.1 Power Management System

The PMS is integrated to ensure that enough power is available for the operational loads. The system shall prevent the occurrence of blackout, and if a blackout occurs, the PMS shall quickly restore the power system (Zadeh, 2020b). Traditionally, the PMS has handled the start/stop of engines to meet the changing power demands. For the future, this is proposed to be lifted to the EEMS, where commands

are based on current and predicted loads. This will potentially result in energy savings and minimized emissions. When fast action is required to reduce power, the PMS disconnects low priority loads. This is referred to as load shedding and is the last resort to prevent blackouts. The PMS also handles power limitations and loadsharing (Bø et al., 2015).

2.4.2 Battery Management System

When a battery system is installed in the power system, the BMS works in parallel to the PMS. The BMS ensures an optimal, safe, and reliable operation of the batteries. To ensure safety, avoiding the risk of fire, the BMS protects the battery from overcharging, overcurrent and overvoltage. This is achieved by monitoring the measurable battery states such as current, voltage, temperature, and impedance. From these measurements, the battery's state of charge (SOC) and state of health (SOH) are estimated. These states are used to maximize the battery's performance within its safe operating area (SOA) (Andrea, 2010). By implementing batteries, different strategies for utilizing the available power can be applied, which will be further discussed in the next paragraph.

2.4.3 Energy and Emission Management System

The higher control level, above the real-time reactive control layer of the PMS and BMS, is the online optimization and guidance layer. In this layer, the EEMS provides references to the PMS and BMS to minimize fuel consumption and emissions while safety and resilience requirements are satisfied. In other words, the EEMS is an extension of the PMS and BMS objectives. Figure 2.12 shows the objectives of the EEMS, which results in optimized system performance.

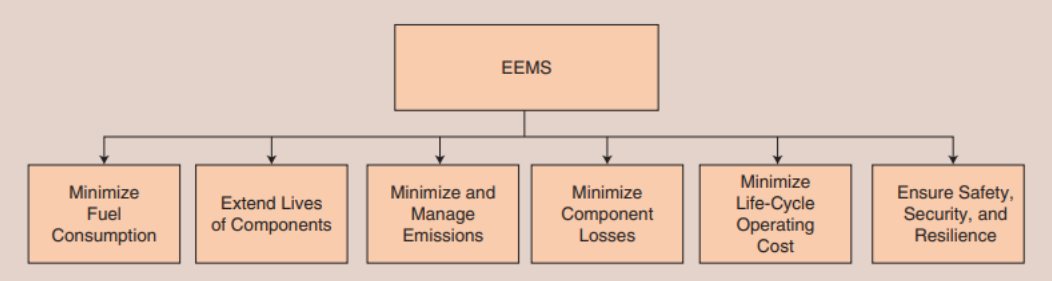

Figure 2.12: Main objectives of the EEMS (Courtesy: Reddy et al. (2019))

The most common loadsharing strategies for hybrid configurations involving BESSs are listed below (Sorensen et al., 2017).

- **Peak shaving:** A strategy for reducing fuel consumption by leveling the demanded engine power between an upper and lower limit. The battery discharges to provide the power required above the upper bound and consumes the excess power when the required power is below the lower limit.
- **Enhanced dynamic performance:** The battery handles an instant load change, preventing the occurrence of blackout from a too rapid load change on the generator. Hence, the generator can gradually ramp up its load. This enables the installation of power sources with slower dynamics, such as fuel cells and LNG engines. For drilling vessels, this can reduce the required backup power supply when the operations are expected to involve large and rapid load changes.
- **Strategic loading:** A strategy where the aim is to optimize the operational point of the engines by charging/discharging the ESDs. This leads to an average reduction in fuel consumption. Strategic loading is a vessel-specific strategy dependent on the fuel consumption curve of the engine.

- **Enhanced ride through:** In the event of a fault of the running generators, the battery provides a short time backup power.

- **Spinning reserve:** A BESS with high energy density can work as a redundant power supply, such that the number of connected generators can be reduced. This allows for a more optimal working condition of the generators, which reduces emissions and fuel consumption.

- **Zero-emission operation:** In this case, the power system is fully powered by the ESDs, while all generators are shut down. This strategy ensures no emissions and is very relevant for future regulations in some harbors and coastal areas. For battery-electric vessels, this is the only operational mode.

2.4.4 Vessel Mission Management System

The VMMS is the top level of the control architecture. It provides the EEMS with information on the operation mode and external conditions, including data from forecasting services. Thus, the information can be both prevailing and predictive. Based on this information, the EEMS estimates load demands, further used to optimize and command the power system. The VMMS receives feedback signals from the EEMS in order to ensure that new vessel operations are not started before the EEMS gives a ”ready” signal (Reddy et al., 2019).

2.4.5 Optimization Strategies to Minimize Energy Consumption and Gas Emissions

Zahedi et al. (2014) proposed an optimization algorithm to minimize fuel consumption of shipboard power systems through detailed efficiency analysis and studying the effect of DC distribution and ESDs. The optimization algorithm concerns hybrid-electric ship applications running on multiple gensets, with objective to calculate the optimal average power of the DC sources and to find the optimal value of the power ripple. Power ripple is a periodic variation of voltage levels that may occur when the power supply from an AC source has been converted to DC. Also, the optimization model contains detailed low-level models of power losses in different units of the electrical system. The optimization solution is a weighted compromise between minimum fuel consumption and optimal utilization of the ESS. The proposed algorithm was utilized in simulations of an offshore support vessel for online optimization of different operation modes.

With the aim to present new ideas on how to improve the efficiency of a hybrid-electric power plant, Bø (2016) proposed methods for optimization and control for a simulation model including the power plant, a hydrodynamic model, and control systems. This differed from earlier marine vessel simulators, which did not consider the interaction effects between the systems. The motivation for the thesis was to reduce the environmental footprint of diesel-electric propulsion by reducing the number of gensets needed during dynamic positioning by modeling and control. A scenario-based model predictive controller (MPC) was presented for generator configuration concerning fault scenarios. By utilizing dynamic constraints, the plant can be maintained within the nominal constraints after a fault scenario occurs. This yields a more flexible optimization since the safety constraints can be applied to the fault trajectories instead of the nominal trajectory, which is a less conservative alternative to conventional static safety constraints. Also, a controller based on MPC was introduced in combination with a power spectrum analysis for peak-shaving control, with the objective to cancel out as much of the load fluctuations as possible while keeping the battery temperature within the safe operating area (SOA). By combining the proposed methods, the number of running gensets could be reduced while maintaining or increasing the safety level.

Miyazaki (2017) studied the viability of strategic loading on hybrid marine systems to reduce average fuel consumption and GHG emissions. In the thesis, two models of the hybrid power system were derived to analyze the power plant performance: a high-fidelity model including the system dynamics, describing the real system accurately, and a steady-state model for real-time applications, validated with the hybrid dynamic model. The aim of the thesis was to produce a simple and intuitive model that can be used to model existing plants, optimize the ESD usage, and develop new optimization algorithms.

A comparison of fuel consumption on a hybrid marine power plant with low-power versus high-power engines was performed by Wu et al. (2018). By using a genetic algorithm method, an optimal operating point for the gensets was found for the different configurations, with regard to fuel consumption and NO_x-emissions. The optimization is based on static load requirements, neglecting fuel consumption and emissions caused by transient loads and the start/stop of engines. The optimization was run with and without an ESS to evaluate the effect of including an ESS. However, the SOC of the ESS is not taken into account, which would yield a better result than in real operation.

Thorat and Skjetne (2018) proposed three methods for optimal online genset scheduling with subsequent loadsharing optimization using mixed-integer linear programming (MILP). The three scheduling methods increase in complexity, starting with minimizing online capacity, then scheduling with redundancy margin for the largest genset, and finally schedule with runtime and connection/disconnection penalties. The loadsharing is based on a piecewise linearization of the SFOC-curves and forms the basis for the model derived in Chapter 5.

2.5 Optimization Methods

Optimization methods can be applied for either offline studies or online optimization. In online optimization problems, the solutions are found without considering the whole problem, i.e., all information about the future is not available when the decision is made. On the contrary, an offline optimization algorithm holds all information of the problem instances from the beginning. Thus, the solution at one instance is dependent on the instances before and after. In shipboard real-time applications concerning load demand, an online optimization algorithm must be applied due to unpredictable conditions, such as weather forecasts or failure of components. In the following subsections, the theory of the optimization methods used in this thesis is presented.

2.5.1 Interior-Point Method

The interior-point (IP) methods have proven to be successful for both linear and nonlinear programming (NLP), and according to Nocedal and Wright (2006) the methods are considered one of the most powerful algorithms for large-scale NLP. The main challenges that arise when the problem is nonlinear are the treatment of nonconvexities, finding a strategy for updating the barrier parameter when there are nonlinearities present, and the need to ensure progress towards the solution. From numerical experience, the IP methods have been observed as faster than other methods, such as active-set sequential quadratic programming methods, for large problems, especially when there are numerous free variables.

The nonlinear problem considered is presented in Equation 2.1.

$$\min_{x,s} \quad f(x) \tag{2.1a}$$
$$\text{s.t.} \quad c_E(x) = 0, \tag{2.1b}$$
$$c_I(x) - s = 0, \tag{2.1c}$$
$$s \leq 0. \tag{2.1d}$$

Here, c_I and c_E are matrices containing all inequality constraints, c_i, and equality constraints, c_e, respectively. A vector of slack variables, s, is included to transform the inequality constraints, $c_I \geq 0$ to equality constraints.

The IP methods can have two different interpretations, the continuous or the barrier method. The main difference between them is that the barrier problem includes a logarithmic term in the objective function of the NLP. Focusing on the barrier method used in Matlab's nonlinear solver *fmincon*, the problem is expressed as

$$\min_{x,s} \quad f(x) - \mu \sum_{i=1}^{m} \ln s_i \tag{2.2a}$$
$$\text{s.t.} \quad c_E(x) = 0, \tag{2.2b}$$
$$c_I(x) - s = 0, \tag{2.2c}$$

where $\ln$ is the natural logarithm and μ is a positive parameter referred to as the barrier parameter. Since $\ln s \to -\infty$ when $s \to 0$, the last constraint in Equation 2.1 can be neglected. By solving the approximate problem for a sequence of barrier parameters $\{\mu_k\}$ that converges to zero, the minimum of 2.2 should converge to a solution of the NLP in 2.1. The KKT conditions for the barrier problem are

$$\nabla f(x) - A_E^T(x)y - A_I^T(x)z = 0, \tag{2.3a}$$
$$-\mu S^{-1}e + Z = 0, \tag{2.3b}$$
$$c_E(x) = 0, \tag{2.3c}$$
$$c_I(x) - s = 0. \tag{2.3d}$$

Here A_E(x) is the Jacobian matrix of the equality constraint matrix, c_E, and A_I(x) is the Jacobian for the inequality constraint matrix, c_I. y and z are their Lagrange multipliers. S and Z are diagonal matrices where the elements are given by the vectors s and z. The vector e is a column vector of ones. Since the second KKT condition becomes more nonlinear as $s \to 0$, the equation is multiplied by S, transforming it into a quadratic equation. This does not change the solution since S consists of positive elements. Hence, the KKT conditions become

$$\nabla f(x) - A_E^T(x)y - A_I^T(x)z = 0, \tag{2.4a}$$
$$SZ - \mu e = 0, \tag{2.4b}$$
$$c_E(x) = 0, \tag{2.4c}$$
$$c_I(x) - s = 0. \tag{2.4d}$$

Which are equal to the KKT conditions of the initial problem in Equation 2.1. From these equations a primal-dual system is obtained, for the variables x, s, y, z, by applying Newton's method. That is,

$$\begin{bmatrix} \nabla^2_{xx}\mathcal{L} & 0 & -A_E^T(x) & -A_I^T(x) \\ 0 & Z & 0 & S \\ A_E(x) & 0 & 0 & 0 \\ A_I(x) & -I & 0 & 0 \end{bmatrix} \begin{bmatrix} p_x \\ p_s \\ p_y \\ p_z \end{bmatrix} = - \begin{bmatrix} \nabla f(x) - A_E^T(x)y - A_I^T(x)z \\ SZ - \mu e \\ c_E(x) \\ c_I(x) - s \end{bmatrix}, \tag{2.5}$$

where $\mathcal{L}$ is the Lagrangian of 2.1a - 2.1c. When the step p is calculated, the next iterate can be calculated. The new iterate becomes

$$x^+ = x + \alpha_s^{max} p_x, \quad s^+ = s + \alpha_s^{max} p_s, \tag{2.6a}$$
$$y^+ = y + \alpha_z^{max} p_y, \quad z^+ = z + \alpha_z^{max} p_z, \tag{2.6b}$$

where α prevents the iterates from approaching zero too fast. The parameters are defined as:

$$\alpha_s^{max} = max\{\alpha \in (0,1] : s + \alpha p_s \geq (1-\tau)s\}, \tag{2.7a}$$
$$\alpha_z^{max} = max\{\alpha \in (0,1] : z + \alpha p_z \geq (1-\tau)z\}, \tag{2.7b}$$

with $\tau \in (0,1)$. Typically, the value of τ is set to 0.995.

In addition to iterating using the Newton method, the barrier parameter sequence must be selected. This can be done either by holding μ fixed over multiple iterations until the KKT conditions are sufficiently satisfied or by updating μ at each iteration.

The implementation of a basic IP algorithm is presented in Algorithm 1, obtained from Nocedal and Wright (2006). In this algorithm, the barrier parameter is updated at each iteration.

Algorithm 1 Basic Interior-Point Algorithm

Choose x_0 and $s_0 > 0$ and compute the initial values for the multipliers y_0 and $z_0 > 0$. Select an initial barrier parameter $\mu_0 > 0$ and parameters $\sigma, \tau \in (0,1)$. Set k $\leftarrow$ 0.
repeat
  repeat
    Solve 2.5 to obtain the search direction $p = (p_x, p_s, p_y, p_z)$
    Compute α_s^{max}, α_z^{max} using 2.7
    Compute (x_{k+1},s_{k+1},y_{k+1},$zk+1$) using 2.6
    set $\mu_{k+1} \leftarrow \mu_k$ and $k \leftarrow k+1$
  until E(x_k,s_k,y_k,z_k ; μ_k) $\leq \mu_k$
  Choose $\mu_k \in (0, \sigma\mu_k)$
until a stopping test for the nonlinear program 2.1 is satisfied

Here, $\sigma \in (0,1)$ decides how fast the barrier parameter should decrease, and E(x_k,s_k,y_k,z_k ; μ_k) is an error function expressed as

$$E(x_k, s_k, y_k, z_k; \mu_k) = max\{\|\nabla f(x) - A_E^T(x)y - A_I^T(x)z\|, \|SZ - \mu e\|, \|c_E(x)\|, \|c_I(x) - s\|\}, \tag{2.8}$$

where $\|\cdot\|$ is a vector norm.

2.5.2 Genetic Algorithm

In biology, the chromosomes encode the structure of a living organism. Based on the efficiency of each entity of the chromosome, the best suited organisms are selected for reproduction more often. This is known as natural selection or survival of the fittest. Evolutionary algorithms abstract some of the processes occurring in natural selection into algorithms. According to Sivanandam and Deepa (2008) genetic algorithms (GAs) are the most extended group of research techniques concerning evolutionary computation.

An evolutionary algorithm is a stochastic process operating on a set of individuals in an iterative manner. An individual represents a potential solution to the optimization problem, and the set of individuals is referred to as the population. The population ensures diversity in the search for the optimal solution. A fitness function assigns a fitness value to every individual of the population, which represents quantitative information used to guide the search algorithm and evaluate each individual's performance. Then, the best fitted individuals of the population are selected for reproduction and are often referred to as the parent individuals. The selection process is based on physical appearance, also known as the phenotype, while the reproduction recombines the genotypes, i.e., the genes in the chromosome. Traditionally, the offspring individuals that are created in the reproduction replace the parents in the next generation. Figure 2.13 illustrates how an initial population is spread out randomly in the search space, and how the population moves towards the solution with evolving generations. In the final solution all red diamond shapes, representing the phenotype of the individuals, are gathered in the global minimum. In the contour plot this is illustrated by a denser occurrence of red points.

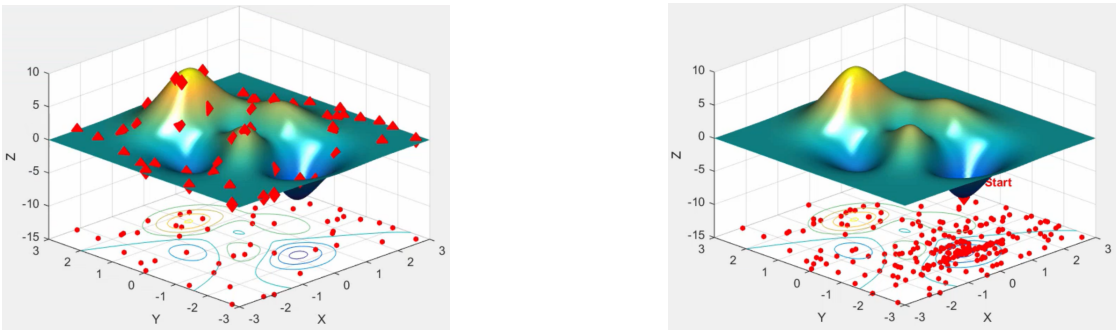

(a) Initial population

(b) Final solution

Figure 2.13: GA optimization (Illustration: Deland (2015))

Holland (1975) was the first to present the GAs as an evolutionary computation technique. The concepts of the algorithms are directly derived from Darwin's theory of natural evolution. In the GAs, a bit-string takes on the role of the chromosome. Hence, the population in a GA is a set of bit-strings. Each position in the string stores a value representing how a feature is expressed in the solution, i.e., a parameter representation. The initial population is randomly generated, representing feasible solutions to the problem. There are multiple operators for reproduction, and the GAs apply the two most common: crossover and mutation. In GAs, the bit-string crossover is the typical crossover operator, as illustrated in Figure 2.14. Bit-string crossover is a reproduction operator where two parent bit-strings produce new offspring by swapping a sub-sequence of the strings. Concerning mutations, the bit-flipping mutation illustrated in Figure 2.15 is widely used. Mutation introduces new information to the population through flipping a single bit-string from the parent. Then, the offspring replace the parents in the next generation. The algorithm will iterate until some predefined termination conditions are satisfied. Termination conditions can be convergence, in terms of number of iterations or a sufficiently low change between iterations.

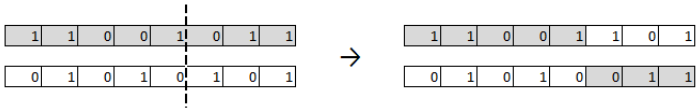

Figure 2.14: Bit-string crossover (Courtesy: Sivanandam and Deepa (2008))

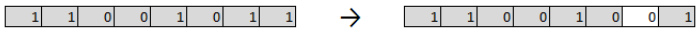

Figure 2.15: Bit-string mutation (Courtesy: Sivanandam and Deepa (2008))

The genetic algorithm's main differences from conventional optimization algorithms are that the optimization is based on a representation of the problem parameters rather than the parameters themselves, instead of a single solution there is rather a population of solutions, and derivatives are replaced with a fitness function. It is important to emphasize that a limitation of the GA is that there is no guarantee for reaching the global optimum.

The GAs have a consequent structure, as presented in Algorithm 2, obtained from Kramer (2017).

Algorithm 2 Basic Genetic Algorithm

```
initialize population
repeat
  repeat
    crossover
    mutation
    phenotype mapping
    fitness computation
  until population complete selection of parental population
until termination condition
```

2.5.3 Model Predictive Control

Model predictive control merges dynamic optimization and feedback control. Dynamic optimization defines the objective function over a prediction horizon, $t = 0$ to $t = N$. Hence, the whole solution is calculated at time $t = 0$ with no feedback control. This is referred to as open-loop optimization. By recomputing the optimal solution at each time instance t, feedback control is ensured (Foss and Heirung, 2016).

According to Mayne et al. (2000):

> *Model predictive control is a form of control in which the current control action is obtained by solving, at each sampling instant, a finite horizon open-loop optimal control problem, using the current state of the plant as the initial state; the optimization yields an optimal control sequence and the first control in this sequence is applied to the plant.*

Further, this basic concept of MPC is illustrated in Figure 2.16. In the figure, t' represents the present sampling instant. The moving prediction horizon $t' + N$ changes correspondingly with each time sample.

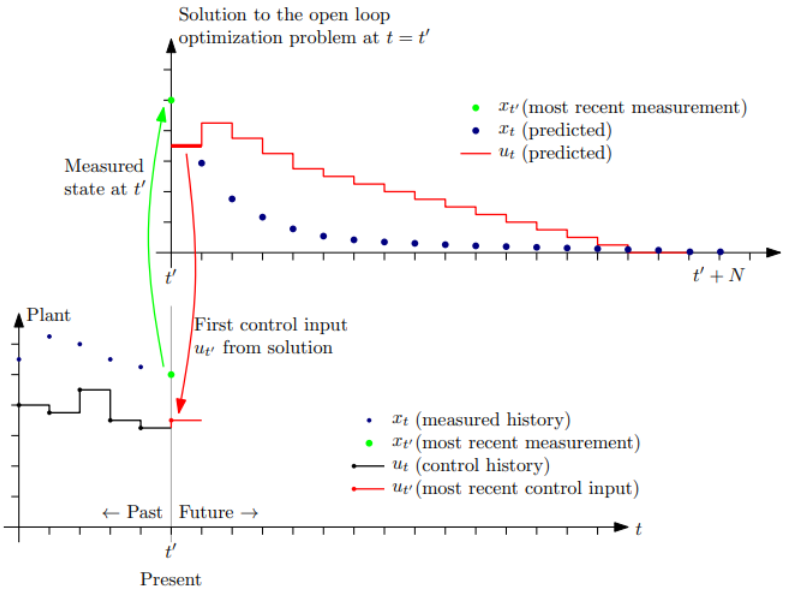

Figure 2.16: Principle of MPC (Illustration: Foss and Heirung (2016))

According to Rawlings et al. (2019), there are two basic concepts of MPC. By utilizing a dynamic model, the system behavior can be forecasted. The behavior forecast is optimized to produce an optimal control action at the current time. The second concept, referred to as the state estimation problem, utilizes the record of past measurements to predict the current state of the system. The need to consider the state estimation problem depends on the quality of the measurement of the current state. If an exact measurement is available, the measurement can be applied directly in the algorithm as described in Algorithm 3. Otherwise, output feedback MPC must be applied, where the state estimate is computed from the control input and the measured output. This concept is described in Algorithm 4. The two algorithms are obtained from Foss and Heirung (2016):

Algorithm 3 State feedback MPC

for i = 0,1,2,... **do**
  Get the current state x_t
  Solve a dynamic optimization problem on the prediction horizon from t to t+N with x_t as initial condition.
  Apply the first control move u_t from the solution above.
end for

Algorithm 4 Output feedback MPC

for i = 0,1,2,... **do**
  Compute an estimate of the current state $\hat{x}_t$ based on the measured data up until time t.
  Solve a dynamic optimization problem on the prediction horizon from t to t+N with $\hat{x}_t$ as initial condition.
  Apply the first control move u_t from the solution above.
end for

Model Predictive Control in Marine Vessel Power Systems

There are multiple examples of MPC applications to marine vessel power systems. Bø and Johansen (2013) proposed a controller to handle requirements for failure scenarios in the power generation. This is relevant for DP vessels of classes 2 and 3, where power loss requirements defined by the class regulations state that a single point failure should not lead to loss of position (DNV GL, 2015a). Therefore, the MPC algorithm was designed to keep the bus frequency within a safety margin, preventing frequency drops that might lead to blackout. The algorithm was tested in a simulation with a fault scenario where one generator was disconnected.

In Stone et al. (2015) a constrained nonlinear MPC approach was proposed to predict the dynamic power source and load demand. By implementing a multi-objective cost function and safety constraints, the controller optimizes the ship performance concerning predicted load disturbances. The cost function encloses a weighted performance optimization of bus voltage deviation, power tracking error, fuel efficiency, ship velocity deviation, droop gain ramp rates, and prime mover ramp rates. This MPC approach was applied to a medium voltage DC testbed, utilizing an interior-point optimizer and sequential quadratic programming to solve the nonlinear optimization problem.

Vu et al. (2017) proposed an MPC-based energy management scheme to optimize the hybrid power source coordination under high-power ramp rate conditions. The hybrid-MPC proposed in the paper aims to solve the fast response requirement for the optimized scheduling of gensets and ESSs to satisfy the high-power ramp rate demands. In the EMS, an energy management scheme optimizes the genset and ESSs scheduling to satisfy the load demands. The methodology utilizes the ESS if the load ramp rate exceeds the capability range of the gensets. Otherwise, the MPC is utilized to recover the ESS's SOC. Hence, the MPC ensures that the ESS is charged and discharged at an optimal ramp rate.

Bø and Johansen (2017) investigated the utilization of an MPC-based optimization to ensure safe operation of a battery. In this case, the battery was installed to smooth out power fluctuations in the gensets. Thus, the load fluctuations exceeding a bandpass filter were set as the reference for the battery. The nonlinear MPC was applied to set the time constants of the band-pass filter, keep the battery temperature below a maximum limit, and keep the SOC within an optimal range.

Dahl et al. (2018) investigated the applicability of the structure preserving model (SPM) for MPC. The SPM for marine vessel power systems was developed by Dahl et al. (2017), based on the SPM for bulk power systems from Bergen and Hill (1981) and Hill and Bergen (1982). The SPM models a power system by utilizing graph theory, where nodes in a graph represent power producers and consumers. The SPM for marine vessel power systems models the causation of changes in engine output torque, considering changes in engine velocity and phase angle, to change in electric load. In this case, the network power flow is from a three-phase, alternating current. By simulation, the viability of MPC for the SPM was tested for three objective functions. The objective functions considered frequency regulation, transient load sharing control, and bustie power control.

2.6 Data for Hybrid-Electric Power Systems

Concerning the relevant units of a hybrid-electric power system, such as diesel engines, fuel cells, ESDs, and power converters, different specifications are important to consider when modeling the power plant. Relevant specifications may be specific fuel consumption, efficiencies, nominal capacity and voltage, and rated power. Here, the typical data concerning diesel engines and diesel-electric power systems are presented. Further, the data specifications related to fuel cells and batteries are defined in detail in Chapter 3 and 4, respectively.

2.6.1 Specific Fuel Consumption

The specific fuel consumption is a measure of the fuel consumed per unit of energy delivered and is typically measured in grams per kilowatt-hour. For diesel engines, a specific fuel consumption curve made from engine trials indicates the engine's performance and optimal operating points. These are typically presented as contour plots concerning engine speed and power output, and the optimum is typically between 60-80% of the maximum continuous rating (MCR). Two different engine curves are shown in Figure 2.17.

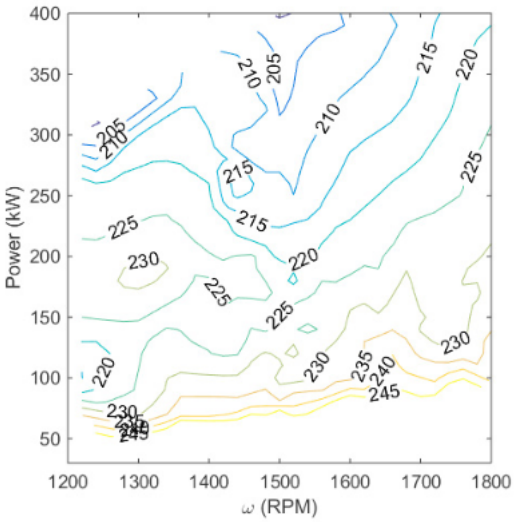

(a) SFC curve (in [g/kWh]) of Perkins 2506C-E15TAG1 engine at NTNU hybrid laboratory (Miyazaki, 2017)

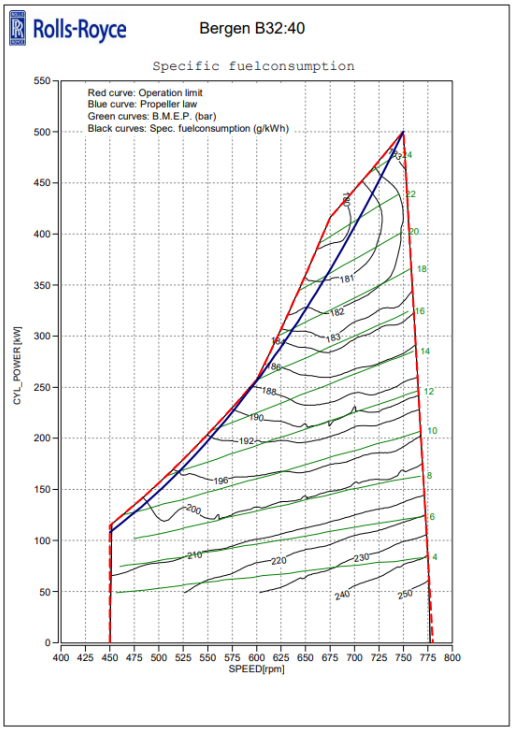

(b) SFC curve of Bergen B32:40 engine (Rolls-Royce, 2016)

Figure 2.17: Specific fuel consumption curves

In Figure 2.17b it can be observed that the optimal operating point is slightly above 80% of MCR.

2.6.2 Typical Losses in Hybrid-Electric Power Plants

When working with hybrid-electric power plants, it is important to consider the losses in the power transition. Figure 2.18 illustrates the power transition in a diesel-electric power plant. The components have different efficiencies, which are approximated to the shown values. However, it should be emphasized that these values, which typically are presented in product specification sheets, are representing the most favorable operation condition.

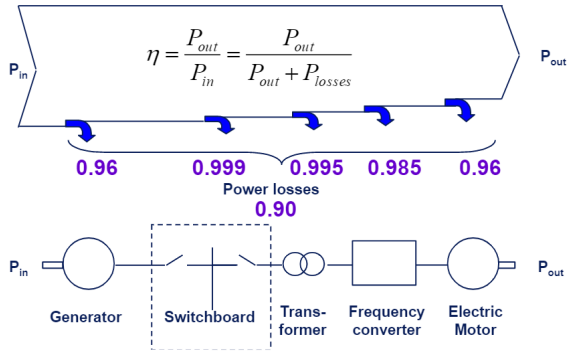

Figure 2.18: Power efficiencies in a DE power plant (Illustration: Zadeh (2020a))

Concerning the power losses on a more detailed level, it is experienced that the efficiency varies with power output. For instance, are power converters quite stable in a wide range of power output but have a rapid decrease in efficiency for low power outputs. This is discussed in Ghimire et al. (2019), and illustrated in Figure 2.19.

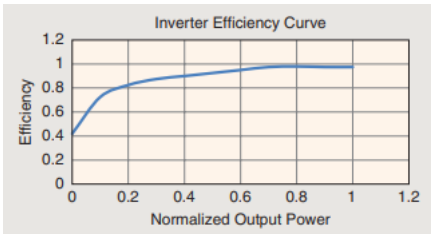

(a) DC-to-AC

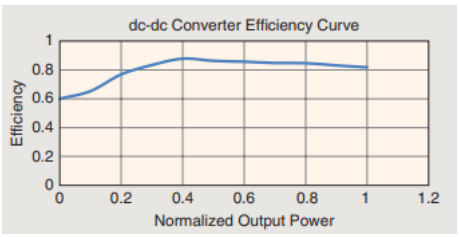

(b) DC-to-DC

Figure 2.19: Converter efficiencies as a function of output power (Courtesy: Ghimire et al. (2019))

Chapter 3

Emerging Zero-Emission Technologies

The state-of-the-art of relevant zero-emission power producers for ship application is outlined, with the main focus on design and control parameters. Parts of this chapter are based on my project thesis (Igland, 2020).

3.1 Internal Combustion Engines

This section is mainly based on information obtained from meetings with Egil Hystad and Kaj Portin in Wärtsilä.

3.1.1 Basic Knowledge

By investing in the development of modular engines and related storage systems, Wärtsilä contributes towards a transition in the shipping industry. With experience from converting diesel engines to dual-fuel, they investigate the feasibility of providing flexible engines with multifuel operation. Internal combustion engines can be modified to operate on any fuel, and Wärtsilä has been investigating hydrogen-containing fuel options, such as ammonia, hydrogen, methanol, and methane.

Focusing on combustion involving ammonia, there are two alternative applications. Either performing small modifications of an existing engine and investigate how much ammonia can be fed into it or designing an engine optimized for ammonia operation. Ammonia has good applicability and can be injected as gas or liquid, depending on the engine. However, ammonia ignites and burns poorly and needs a pilot fuel to ignite.

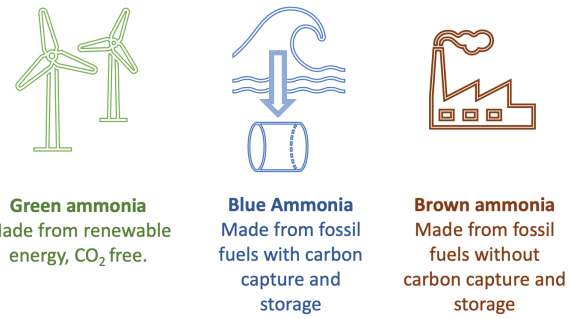

Figure 3.1: Ammonia classifications (DNV GL, 2020)

It is important to emphasize that the ammonia must be green in order to have a zero-emission value chain. Brown ammonia is produced from natural gas without carbon capture and storage. In that case, the natural gas could just as well be utilized directly in the engines. This is also the case for blue ammonia, where LNG could be used with carbon capture instead. Figure 3.1 illustrates the production processes classifying ammonia.

3.1.2 Relevant Projects

As part of the research and development of ammonia as a future fuel, Wärtsilä performed chamber tests in the winter of 2020 to obtain combustion properties. The testbed is located in Vaasa, Finland, and is shown in Figure 3.2.

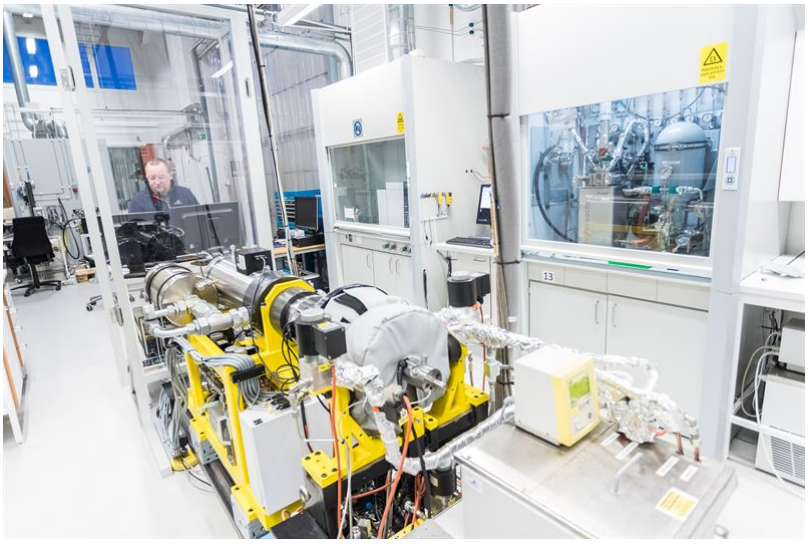

Figure 3.2: Wärtsilä's engine for chamber tests (Courtesy: Wärtsilä (2020d))

Those tests were followed up with short-term tests in a prototype engine (W6L32LG) in Vaasa, January 2021. Further, a full-scale test is scheduled for September 2021 in Sustainable Energy Catapult Centre's facilities at Stord, Norway. The testbed is supposed to consist of 6-cylinder, inline dual-fuel engines (W6L34DF), with a rated power of 3 MW. The engines will be equipped with three nozzles for injection of ammonia, diesel, and natural gas. The diesel will be utilized for ignition, and the natural gas will be mixed with the ammonia to improve the combustion. In the early stages, the engine's fuel flexibility is an important factor, assuring that the vessels can operate even if the access to ammonia is limited in some areas or periods.

3.1.3 Relevant Products and Characteristics

Wärtsilä has four types of engines that all are suitable for combustion involving ammonia.

- The SG engines are gas engines, where a spark plug ignites the combustion. In gas engines, ammonia is mixed with natural gas.
- The DF engines can burn both gaseous and liquid fuels, utilizing diesel as pilot fuel. The ammonia is mixed with natural gas and/or diesel.
- The GD engines are gas engines operating with high pressurized gas. The ammonia is mixed with diesel.
- In diesel engines the ammonia must be mixed with the diesel.

The dynamic response of the engines will depend on the fuel mixture. When faster dynamics are necessary for an engine running on an ammonia-LNG mixture, the fraction of LNG is increased to compensate for the change.

The specifications of the dual-fuel engine that will be utilized for the long-term tests are presented in Table 3.1. The data is obtained from the engine's product guide (Wärtsilä, 2020c).

Table 3.1: Engine specifications of Wärtsilä's 6L34DF engine (Wärtsilä, 2020c)

Rated power [kW]	3000
Engine dimensions (l x w x h) [mm^3]	5335 x 2380 x 3500
Engine weight [tonnes]	35
Frequency [Hz]	50
Speed [rpm]	750
Efficiency [%]	47

A crucial factor for seaborne vessels is the space required to store the fuel. Ammonia is less energy-dense than diesel, which implies that an ammonia-fueled vessel will have reduced cargo capacity if all other operational factors remain the same. Also, the toxicity of the fuel will require additional equipment and space to maintain safety. While considering emissions related to the fuels, weight density is the critical factor. A comparison of ammonia and diesel concerning these two energy densities is presented in Table 3.2.

Table 3.2: Energy density of ammonia compared to diesel

	NH_3	**MGO**
Specific energy [MJ/kg]	18.65	42.70
Energy density [MJ/L]	12.70	36.00

This means that 1 kg diesel is equivalent to 2.3 kg ammonia in terms of energy. Further, 1 L diesel is equivalent to 2.88 L ammonia.

3.1.4 Emissions

The emissions from the ammonia engine depend on the mixing ratio between the fossil fuel and the ammonia. There is little experience concerning emissions of ammonia combustion. In pure ammonia combustion, there will be no CO_2 emissions. However, there are three important scenarios to consider when ammonia is utilized as fuel:

- **NO_x**: In the cylinders of a combustion engine there is $>80\%$ air. Hence, it is believed that the nitrogen in ammonia will not affect the emissions that much. NO_x emissions are mainly dependent on the temperature of combustion. Currently, the NO_x emissions are regulated by IMO's Tier II and Tier III.

- **Unburnt NH_3**: Usually, an SCR catalyst is installed in the exhaust system of an internal combustion engine. The absorbing reductant that bounds down the NO_x in the catalyst is urea, which is a chemical compound of ammonia. Hence, there is a possibility that an amount of unburnt ammonia will result in a self-cleaning effect.

- **N_2O**: A product of combustion of ammonia may be N_2O. This is a critical scenario that should not happen, as N_2O is a GHG that is 200-300 times as potent as CO_2.

3.2 Fuel Cells

Parts of the information in this section are obtained in lectures in the course TMR15 and from a meeting with Tjalve Magnusson Svendsen in Prototech.

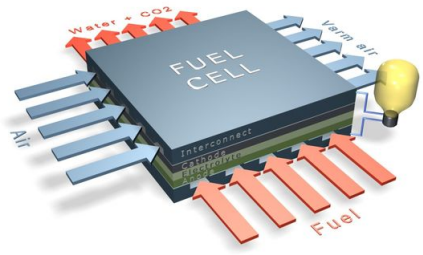

Figure 3.3: Fuel cell illustration (Illustration: Prototech (2020))

3.2.1 Fuel Cell Technology

Fuel cells convert chemical energy to electrical energy directly. The main components consist of an electrolyte, an anode, and a cathode. Fuel is injected at the anode side, and at the cathode there is an air inlet. A general illustration of a fuel cell is shown in Figure 3.3. Further, Figure 3.4 illustrates how the fuel ions move through the electrolyte while the electrons flow through a DC circuit. The exhaust from the fuel cell is water and hot air, and potentially CO_2 dependent on the fuel injected. By connecting multiple fuel cells in series, the voltage and power can be increased. This is referred to as a fuel cell stack.

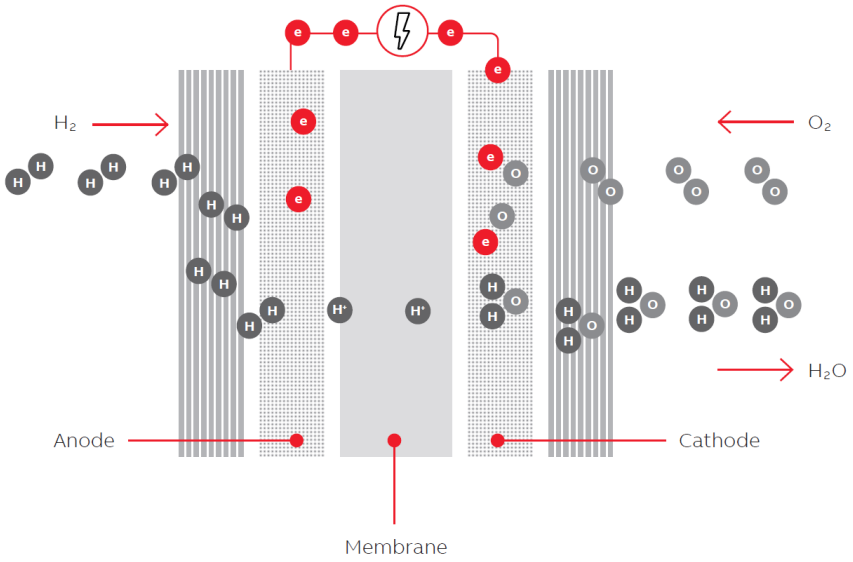

Figure 3.4: Chemical flow in a fuel cell (Illustration: ABB (2020))

Two types of fuel cells relevant to marine applications are solid oxide fuel cells (SOFCs) and proton exchange membrane fuel cells (PEMFCs). SOFCs are high-temperature fuel cells with operational temperatures from 500 to 1000 °C. Due to the high temperature, the fuel can be internally reformed in

the fuel cell. Hence, the fuel cell has a high tolerance for fuel impurity for operation. However, the long start-up and slow dynamics related to the high-temperature requirement are drawbacks of the SOFCs. The SOFC may reach an efficiency of 70% when a gas turbine is included to utilize the excess heat. On the contrary, PEMFCs are low-temperature fuel cells operating at temperatures between 65-85 °C. They have faster dynamics compared to SOFCs and handle transients better. PEMFCs are also less voluminous and cheaper than SOFCs. The main drawback of PEMFCs is that they require pure hydrogen as fuel. Due to the purity of the fuel, the PEMFCs may reach an efficiency of 60% (van Biert et al., 2016).

Table 3.3: Comparison of SOFC and PEMFC

	SOFC	**PEMFC**
Temperature range	500 - 1000 ° C	65 - 85 ° C
Efficiency	45 - 70 %	40 - 60 %
Fuels	LNG, Diesel, NH_3	H_2
Internal reforming	Yes	No

The fuel energy properties of hydrogen are presented in Table 3.4, compared to ammonia and diesel.

Table 3.4: Energy density of hydrogen compared to ammonia and diesel

	H_2 Liquefied	**H_2 Pressurized**	**NH_3**	**MGO**
Specific energy [MJ/kg]	120.00	120.00	18.65	42.70
Energy density [MJ/L]	8.50	4.50	12.70	36.00

3.2.2 Efficiency

The electrical efficiency of a fuel cell is defined as

$$\eta_{FC} = \frac{\text{Energy delivered by the fuel cell}}{\text{Energy content of the supplied fuel}} \times 100\%. \tag{3.1}$$

This theoretical value will not be obtained in a real system due to heat produced as a by-product of the operation (Wenzl, 2009). The electrical energy delivered by the fuel cell refers to the efficiency in applications where only the electrical output of the fuel cell is used, e.g., hybrid electric vehicles. In applications where the excess heat is utilized, i.e., combined heat and power applications, the thermal efficiency must be considered as well. In this case, the total efficiency becomes

$$\eta_{FC} = \frac{\text{Energy delivered by the fuel cell} + \text{Thermal energy supplied}}{\text{Energy content of the supplied fuel}} \times 100\%. \tag{3.2}$$

The total efficiency can be up to approximately 85% in combined heat and power fuel cell systems.

The efficiency is affected by high charge transfer overpotentials, diffusion overpotentials, electrical resistance in system components, and fuel diffusion through the membrane. Temperature effects apply to most of these factors as well. Increasing temperature decreases the theoretical efficiency, while the practical efficiency increases. This is shown in Figure 3.5. Since fuel cells require auxiliary components such as pumps, compressors, and heating and cooling devices, the efficiency must be determined on a system level.

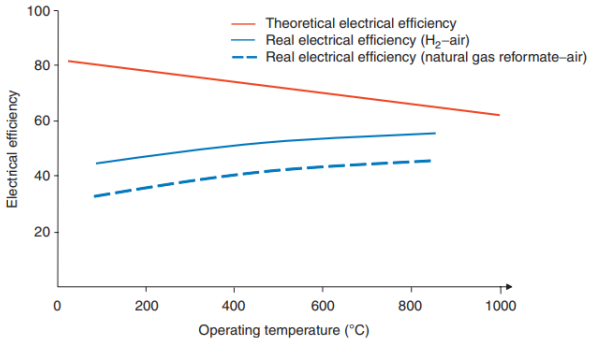

Figure 3.5: Theoretical and real efficiency as a function of temperature for PEMFC systems (Courtesy: Wenzl (2009))

The auxiliary components require a continuous and quite constant energy supply. In standby operation, this results in very low efficiency, but with increasing power the efficiency increases. When the power output increases further, internal losses occur, and the voltage falls. This yields the shape shown in Figure 3.6, where the ICE and the FC stack without auxiliary components are included for comparison.

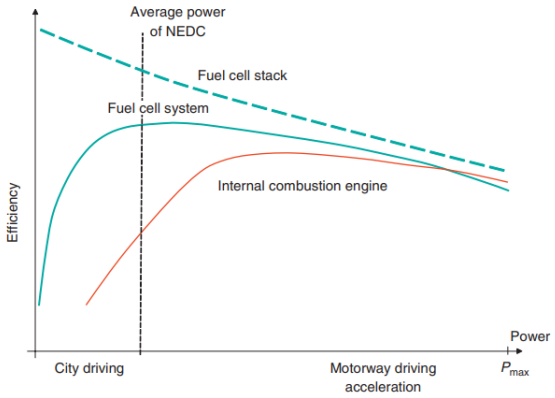

Figure 3.6: PEMFC system efficiency curve compared to an ICE and a single FC stack (Courtesy: Wenzl (2009))

3.2.3 Lifetime

The expected lifetime of a PEM fuel cell for transport applications is approximately 5000 hours (Xing et al., 2021). A realistic operation will involve conditions exposing the fuel cells for stress on chemical and mechanical materials and components. These conditions might be fuel or air impurities, frequent starting and stopping, or humidity, resulting in cell degradation.

The fuel cell stack contains multiple cells, and all components may suffer from degradation. In order to consider degradation effects between components and auxiliaries, the fuel cell degradation is typically considered on stack level. On cell level, the degradation mechanisms can occur in the membrane, electrodes, or gas diffusion layer. The electrolyte, also called the membrane, can be affected by mechanical, thermal, and/or electrochemical degradation due to stress or contamination. The anode and cathode electrodes may suffer from activation and conductivity loss, mass transport decrease, and decreased water management ability. When the gas diffusion layer, which allows the reactant to diffuse to the active sites, experiences carbon corrosion, its structure is decreased. On stack level, degradation may occur in the bipolar plate, which isolates the cells and conducts current between them, and in the sealing gasket, which separates the hydrogen from the air and prevents gas leakage. For both components, mechanical stress and corrosion are the degrading factors (Yue et al., 2019).

Chapter 4

Battery Energy Storage Systems

This chapter gives an overview of battery energy storage systems, their working principles, and important properties for design and operation. Parts of this chapter are based on my project thesis (Igland, 2020).

4.1 Battery Technologies

Marine batteries are secondary batteries, i.e., the transition from chemical to electrical energy is reversible, and the battery is rechargeable. The galvanic cell is the most basic element of the battery, where the chemical process occurs. A module is a parallel or serial connected set of battery cells. Further, a battery pack consists of multiple parallel or serial connected modules.

Table 4.1 shows the characteristics of different battery technologies based on specifications from Mutarraf et al. (2018). The lead-acid battery is a mature technology but has quite low energy density. The nickel-cadmium is required to be implemented only in stationary applications due to the cadmium-toxicity. Sodium-sulfur batteries require a temperature range of 300-350 °C. Thus, the Li-ion battery is favored due to its high power and energy density and its high efficiency. The high cost of Li-ion batteries was a big disadvantage, but the cost has come down due to mass production in recent years.

Table 4.1: Comparison of battery characteristics

	Lead Acid	**Nickel Cadmium (NiCd)**	**Sodium Sulphur (NaS)**	**Lithium-ion (Li-ion)**
Power density [kW/kg]	75-300	150-300	150 - 230	150-315
Energy density [kWh/kg]	30-50	50-75	150-240	75-200
Efficiency [%]	65-80	75-85	75-90	95-97
Life time [years]	3-15	5-20	10-15	5-100

4.1.1 Present Maritime Li-ion Batteries

According to Alnes et al. (2017) the relevance of Li-ion batteries is expected to grow in the maritime sector. The development of battery technology is improving fast, and investment costs are expected to decrease as manufacturing volume increases. As lithium-ion batteries are characterized by both high energy density and high power density, their range of application is wide.

Maritime batteries are quite heavy compared to electric car batteries. One of the main factors to this is power requirements. A fundamental property of batteries is that their weight is directly related to power. If fast charging or discharging is important, it will result in a heavier battery (Godø and Vinje, 2019).

Further, the main challenge of the Li-ion batteries is the reduction in lifetime through deep discharge. Hence, choosing the right battery for a maritime vessel is a trade-off between minimizing weight, high C-rates, and long battery lifetime.

4.1.2 Emerging Solid-State Battery Technology

Another promising battery type is the solid-state battery. Replacing the liquid electrolyte with a solid electrolyte enables improvements in safety, energy density, cycle life, and C-rates (Braga et al., 2017). However, Tvete and Hill (2021) concludes that the spread and commercialization of solid-state batteries is largely dependent on the industry demand and overcoming the high initial costs.

4.2 Battery Working Principles

A battery is characterized by the parameters and variables listed below:

- **SOC [%] :** State of charge. Percentage of the maximum capacity of the battery, typically determined through current counting.
- **DOD [%] :** Depth of discharge. Measure of charge removed from the battery.
- **C-rate [C] :** The rate the battery is discharged relative to maximum capacity.
- **SOA :** Safe operating area. Limited by current, temperature and voltage, as illustrated in Figure 4.2.
- **SOH [%] :** State of health. Remaining capacity of the battery, compared to nominal capacity.
- **Cycle life :** The number of charge/discharge cycles before the battery fails to meet specific performance criteria.
- **OCV [V] :** The open circuit voltage; represents the voltage when no load is applied.
- **Cut-off voltage [V] :** Minimum allowable voltage of the battery.
- **Nominal voltage [V] :** Voltage with load applied between the battery terminals. Dependent on current and SOC.
- **Nominal capacity [Ah] :** The dischargeable capacity from 100% SOC to the cut-off voltage at a specific C-rate.
- **Nominal energy [Wh] :** The energy capacity from 100% SOC to the cut-off voltage at a specific C-rate.
- **Specific energy [Wh/kg] :** Gravimetric energy density. Nominal battery energy per unit mass.
- **Specific power [W/kg] :** Maximum available power per unit mass.
- **Energy density [Wh/L] :** Volumetric energy density. Nominal battery energy per unit volume.
- **Power density [W/L] :** Maximum available power per unit volume.

4.2.1 State of Charge

The state of charge of a battery is expressed in percent and represents the available charge. The ratio is expressed as

$$SOC = \frac{C}{C_{nom}} = \frac{Q}{Q_{nom}}. \tag{4.1}$$

Here, C is the available dischargeable capacity in the battery, while C_{nom} is the battery's nominal capacity. Further, Q and Q_{nom} is the available and nominal energy capacity, respectively. The charge capacity has unit ampere-hours (Ah) while the energy capacity has unit kilowatt-hours (kWh). The difference is whether the nominal voltage is considered. The energy capacity is the product of the charge capacity and the nominal voltage,

$$Q[Wh] = C[Ah] \cdot V_{nom}[V]. \tag{4.2}$$

There are no direct measurements to monitor the SOC, and it is typically estimated by current counting,

$$SOC_t = SOC_0 + \frac{1}{C_{nom}} \int_0^t i_{bat} dt, \tag{4.3}$$

where SOC_0 is the initial SOC. Due to battery degradation over time, the SOC estimate will not remain accurate if the nominal capacity is kept constant over time. This is further discussed in the subsection on the battery's state of health.

4.2.2 Depth of Discharge

Depth of discharge is another measure of the battery's charge relative to maximum capacity. DOD is the complement of SOC and thus describes how much charge has been removed from the battery.

The utilization of the battery affects the cycle life of the battery. Figure 4.1 shows how the cycle life is reduced when a nickel-manganese-cobalt (NMC) battery is deeper discharged. This is further discussed in the subsection on the state of health.

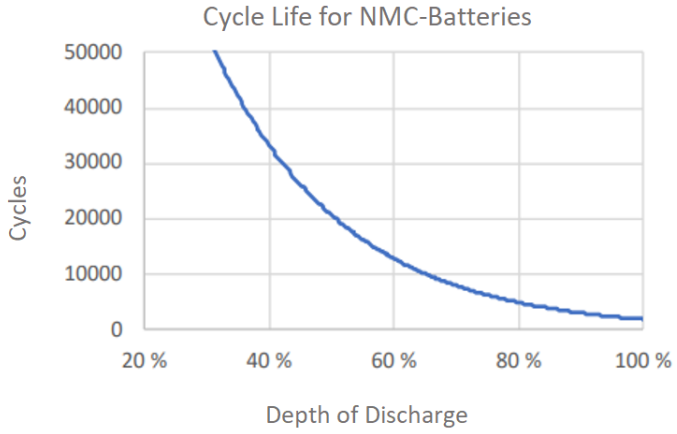

Figure 4.1: Cycle life as function of DOD for NMC-batteries (Courtesy: Godø and Vinje (2019))

4.2.3 C-rate

The C-rate is a measure of the rate the battery is discharged relative to maximum capacity. It is either characterized as a ratio of current through the battery to the capacity or as a ratio of power to energy

capacity:

$$C\text{-}rate[C] = \frac{I}{C_{nom}} \frac{[A]}{[Ah]} \tag{4.4a}$$

$$C\text{-}rate[C] = \frac{P}{Q_{nom}} \frac{[kW]}{[kWh]} \tag{4.4b}$$

Thus, given a C-rate of 1C means that the discharge current/power will fully discharge the battery in 1 hour. The C-rate unit, C, is equivalent to h^{-1} and must not be confused with the unit for electric charge, coulomb.

4.2.4 Safe Operating Area

Figure 4.2 illustrates the limitations of the safe operating area of a battery, operation outside this range will speed up the battery degradation processes and potentially permanently damage the battery. The battery's lifetime depends on temperature, voltage, and charge/discharge current, and as illustrated, the limitation is stricter for charging than discharging. Through discharge below the lower voltage limit, the battery can be damaged. Further, overvoltages may lead to cell ignition. Too high C-rates are also a lifetime reducing factor of the battery.

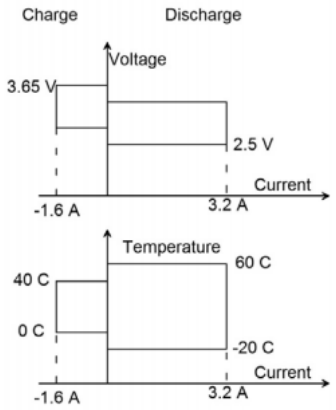

Figure 4.2: Battery SOA (Andrea, 2010)

A Recommended Operating Area (ROA) can be introduced as a subset of the SOA, ensuring a safety buffer through less extreme limits. By operating the battery within a well-defined ROA, the life expectancy of the battery is enhanced (Gulsvik, 2017).

4.2.5 State of Health

The state of health is a measure of battery degradation, and indicates how much of the original maximum capacity is remaining of the battery. This can be expressed as the ratio between total and nominal capacity,

$$SOH = \frac{C_{total}}{C_{nom}}. \tag{4.5}$$

Here, C_{total} represents the maximum capacity as a variable depending on the battery degradation.

The degradation over time affects the battery energy and power and is characterized by loss in cell capacity and increased internal impedance, respectively (Allam and Onori, 2020). SOH cannot be measured as an exact physical quality, and the most common values used to estimate SOH in the BMS are

the history of temperatures and charge/discharge cycles.

In order to estimate the SOC and SOH, there are two main groups of model-based SOC- and SOH-algorithms. These are characterized by the battery model used in the estimation, either the equivalent circuit model and the electrochemical model. The equivalent circuit model is easy to implement but does not provide any insight into the battery's internal dynamics. On the contrary, the electrochemical model provides physical insight into the battery dynamics but at a computational expense important for the real-time performance (Allam et al., 2020).

Li-ion batteries have an end of life defined as a reduction of 20-30% relative to the initial battery capacity. However, this does not imply that the battery is damaged; there is still a value to the remainings. The battery can be used in other applications for a second-life purpose, or the battery can be recycled (Godø and Vinje, 2019).

4.2.6 Efficiency

Li-ion batteries are both energy and charge efficient. Li-ion batteries can practically be considered 100% charge efficient, meaning that all electrons supplied to the cell during charging can be depleted through discharging. This is due to the small side reactions, i.e., corrosion reactions and electrolyte decomposition, in Li-ion batteries. Charge efficiency is not the same as energy efficiency. Since the voltage is decreased during discharge compared to charging, all energy will not be recovered. In specification sheets, the charge efficiency may not account for fully charged/discharged batteries. Hence, the 100% charge efficiency is, in many instances, a pure academic property (Andrea, 2010).

The energy efficiency of a Li-ion battery depends on charging and discharging conditions, and is directly related to power wasted to heat inside the Li-ion cells. This waste heat will increase with increasing current. The efficiency represents the energy utilization rate and can be defined in three ways (Li and Tseng, 2015) depending on which state is considered. It is typically evaluated during discharging, described as

$$\eta_D = \frac{\Delta E_{out}}{\Delta E_{bat}}, \tag{4.6}$$

where ΔE_{out} is the energy discharged from the battery, and ΔE_{bat} is the net energy of the battery, i.e. the chemical energy stored. Otherwise, the charge efficiency can be measured as

$$\eta_C = \frac{\Delta E_{bat}}{\Delta E_{in}}. \tag{4.7}$$

Here, ΔE_{in} is the energy from a power source extracted to charge the battery. Considering the whole charge-discharge cycle, the energy efficiency can be calculated as

$$\eta_{cyc} = \frac{\Delta E_{out}}{\Delta E_{in}}. \tag{4.8}$$

Further, the energy efficiency, also called electrical efficiency, can in more detail be determined by the product of the voltage and coulombic efficiency (Wenzl, 2009). The coulombic efficiency is the same as the charge efficiency. Considering the voltage efficiency, it can easily be obtained as long as the current is constant. The voltage efficiency is the ratio of average voltage during discharge to average voltage during charge. The voltage efficiency is dependent on the internal resistance of the cell. Cells designed for high rates have lower internal resistance and thus higher voltage efficiency.

In addition to the internal resistance of the battery cells, the temperature, battery age, charging characteristics, and other aspects of application have an impact on the efficiency. The power electronics will also affect the efficiency when the whole system is considered.

Chapter 5

Power Plant Models and Optimization Methods

An introduction to the models and optimization problem formulations used to optimize the loadsharing in different power plant configurations is given. The aim is to reduce fuel consumption. The models established are high-level, simplified models concerning power transmission. The optimization problems concern both linear SFOC-optimization and nonlinear FOC-consumption, and are defined for both a single load instance and multiple instances over a horizon. Parts of this chapter are based on my project thesis (Igland, 2020).

5.1 Genset Model

To begin with, a power system consisting of M gensets is considered. The model is based on the genset optimization model derived in Skjetne (2017).

In the genset model the control variable is a vector representing each genset's provided power as a percentage of maximum continuous rating,

$$p = \{p_1, ..., p_M\}, \tag{5.1}$$

where $p_j \in [0, 1]$, and j is the genset index, $j \in \mathcal{I} = \{1, ..., M\}$.

The control input parameters defining the system characteristics and limitations are represented in Table 5.1.

Table 5.1: Control input parameters

Input parameter	**Symbol**
Number of gensets	M
Connection vector	c
Genset rated base power [kW]	P_b
Genset rated ramp-up rate [%MCR/s]	Δp

Here, P_b and Δp are vectors of dimension M, including all genset's rated power and ramp-up rates.

Assuming all gensets are connected to the bus at all time instances, i.e., $c = 1_M$, the optimization concerns loadsharing between all gensets.

5.1.1 Piecewise Linear SFOC Curve

Every diesel engine, j, has its distinctive specific fuel oil consumption curve. Based on a large number of datapoints, m_j, from engine trials at a fixed speed, the specific fuel oil consumption is presented as a piecewise linear (PWL) curve with genset power on the x-axis.

$$y_j = \{y_{j,0}, y_{j,1}, ..., y_{j,m_j}\}, y_{j,i-1} < y_{j,i}, \tag{5.2}$$

$$z_j = \{z_{j,0}, z_{j,1}, ..., z_{j,m_j}\}. \tag{5.3}$$

Here, an engine test of genset j has resulted in the dataset y_j of power inputs as a percentage of MCR and correspondingly the SFOC set z_j.

Utilizing these datapoints, the SFOC curve for a genset j can be derived from an assumption of linearity between two datapoints.

$$h_{j,i}(p_j) = a_{j,i}p_j + b_{j,i}, \tag{5.4}$$

where $a_{j,i}$ and $b_{j,i}$ are curve coefficients representing the linear curve between i and $i-1$, defined as

$$a_{j,i} = \frac{z_{j,i} - z_{j,i-1}}{y_{j,i} - y_{j,i-1}}, \tag{5.5}$$

$$b_{j,i} = z_{j,i-1} - a_{j,i}y_{j,i-1}. \tag{5.6}$$

Here, $i = 1, 2, ..., m_j$.

Since the piecewise linear curves are convex, the corresponding curve fit for p_j is the maximum value of the linearizations,

$$f_{SFOC} = h_j(p_j) = \max_{i=1,...,m_j} h_{j,i}(p_j) = \|h_{j,i}(p_j)\|_\infty \tag{5.7}$$

Hence, the specific fuel consumption of the gensets can be collected in a vector,

$$h(p) = \left[h_1(p_1), h_2(p_2), ..., h_{m_j}(p_{m_j})\right] \tag{5.8}$$

5.1.2 Piecewise Quadratic FOC Curve

Further, from the relation

$$FOC = P \cdot SFOC, \tag{5.9}$$

the fuel consumption for a genset j can be expressed by piecewise quadratic curves by multiplying the piecewise linear SFOC curves by $P_{b,j}p_j$. This gives

$$g_{j,i}(p_j) = P_{b,j}(a_{j,i}p_j^2 + b_{j,i}p_j), \tag{5.10}$$

where a_j and b_j are the curve coefficients vectors defined for the SFOC curves. As for the SFOC curve, the FOC curve is expressed as

$$f_{FOC} = g_j(p_j) = \max_{i=1,...,m_j} g_{j,i}(p_j) = \|g_{j,i}(p_j)\|_\infty. \tag{5.11}$$

This is valid since in general $a\|x\|_\infty = \|ax\|_\infty$ for a constant $a > 0$. It should be noted that the fuel consumption curve generally becomes nonconvex (Skjetne, 2021).

5.2 Fuel Cell Model

The fuel cell can be modeled in a similar way as the gensets. Thus, the same control variable and input parameters presented in Table 5.1, with maximum rated power instead of MCR, are used for the fuel cell system.

The hydrogen consumption of a fuel cell system can be calculated as

$$\text{Hydrogen consumption [kg]} = \frac{\text{Hydrogen effect required [kW]} \cdot \text{Duration [h]}}{\text{Hydrogen energy density [kWh/kg]}} \tag{5.12a}$$

$$= \frac{\text{Fuel cell effect required [kW]} \cdot \text{Duration [h]}}{\text{Fuel cell efficiency [-]} \cdot \text{Hydrogen energy density [kWh/kg]}}. \tag{5.12b}$$

Hence, by letting the fuel cell effect and duration be the model variables, the specific hydrogen consumption curve can be obtained from the fuel cell system's efficiency curve. That is,

$$SHC = \frac{1}{\eta_{FC} \cdot U}, \tag{5.13}$$

where η_{FC} is the fuel cell efficiency and U is the specific energy of hydrogen. Since the efficiency curve has a concave shape, as illustrated in Figure 3.6, the inverse yields a convex specific hydrogen consumption curve. By sampling the efficiency curve into a dataset, the specific hydrogen consumption can be converted into a piecewise linear or quadratic curve in a similar manner as the gensets. Hence, by changing the input parameters and the dataset of the genset model, the fuel cell model is obtained.

5.3 Battery Model

From the theory explained in Chapter 4, a battery model was derived based on the SOC dynamics. The variables and limiting parameters in the initial model are:

- Charge/Discharge rate
- Nominal energy and nominal voltage
- SOC

Here, the charge/discharge efficiency, which is included in the list related to the ESD model described in Miyazaki (2017), is not accounted for. The typical power losses of the modeled components will be considered subsequently in Chapter 7.

Assuming the battery energy is constant, i.e., battery degradation is not considered, the power delivered/consumed by the battery is modeled as

$$P_{bat} = Q_{nom} \cdot C\_rate, \tag{5.14}$$

where the C_rate variable is negative during charging and positive when discharging.

Assuming constant current through the battery for each time instance, the SOC can be modeled from current counting as

$$\begin{aligned} SOC &= SOC_0 - \frac{1}{C_{nom}} \int_0^t I_{bat} dt && (5.15a) \\ &= SOC_0 - \frac{I_{bat}}{C_{nom}} \Delta t && (5.15b) \\ &= SOC_0 - C\_rate \Delta t. && (5.15c) \end{aligned}$$

This shows that the relation between the SOC and C-rate, and the SOC can be expressed by the C-rate variable or reversely. This reduces the number of variables, which is beneficial when working with large optimization problems. Henceforth, only the C-rate is considered a variable.

The performance limits of the battery are expressed as two sets of upper and lower bounds,

$$\begin{aligned} C\_rate_{min} &\leq C\_rate &&\leq C\_rate_{max}, && (5.16a) \\ SOC_{min} &\leq SOC_0 - C\_rate \Delta t &&\leq SOC_{max}. && (5.16b) \end{aligned}$$

5.4 Instantaneous Optimization

The instantaneous optimization concerns a single load instance, and no information about the future is considered.

5.4.1 Genset Optimization

When optimizing the loadsharing among gensets on a bus, different approaches can be applied. If minimizing the specific fuel consumption is the objective, the optimization stays linear, while optimization with respect to fuel consumption yields a nonlinear problem. Both these optimization approaches have the same state vector, defined as

$$x = \begin{bmatrix} p_1 & p_2 & \dots & p_M & \mu_1 & \mu_2 & \dots & \mu_M \end{bmatrix}^T \quad (5.17)$$

where μ_j is a scalar auxiliary variable representing SFOC or FOC, respectively.

Specific Fuel Consumption Optimization

According to Ferris et al. (2007), the linear programming optimization problem for a PWL SFOC curve of an online genset j is expressed as

$$\begin{aligned} \min_{p_j, \mu_j} \quad & \mu_j && (5.18a) \\ \text{s.t.} \quad & a_{j,i} p_j + b_{j,i} \leq \mu_j, && (5.18b) \\ & P_{b,j} p_j = P_{load}, && (5.18c) \\ & p_j^- - \Delta p \leq p_j \leq p_j^- + \Delta p, && (5.18d) \\ & y_{j,0} \leq p_j \leq y_{j,m_j}. && (5.18e) \end{aligned}$$

where p_j^- is the initial power value.

Considering all gensets yields the optimization problem

$$\begin{aligned}
\min_{p,\mu} \quad & c^T \mu && \text{(5.19a)}\\
\text{s.t.} \quad & Ap + E\mu \leq -b, && \text{(5.19b)}\\
& (c \circ P_b)^T p = P_{load}, && \text{(5.19c)}\\
& c \circ (p^- - \Delta p) \leq p \leq c \circ (p^- + \Delta p), && \text{(5.19d)}\\
& c \circ p_{min} \leq p \leq c \circ p_{max}, && \text{(5.19e)}
\end{aligned}$$

where $\circ$ is the Hadamard product. The matrices are defined as

$$A := \begin{bmatrix} a_1 & 0_{m_1\times 1} & \cdots & 0_{m_1\times 1} \\ 0_{m_2\times 1} & a_2 & \dots & 0_{m_2,1} \\ \vdots & \vdots & \ddots & \vdots \\ 0_{m_j\times 1} & 0_{m_j\times 1} & \cdots & a_M \end{bmatrix}, \quad E := \begin{bmatrix} -1_{m_1} & 0_{m_1\times 1} & \cdots & 0_{m_1\times 1} \\ 0_{m_2\times 1} & -1_{m_2} & \dots & 0_{m_2,1} \\ \vdots & \vdots & \ddots & \vdots \\ 0_{m_j\times 1} & 0_{m_j\times 1} & \cdots & -1_{m_M} \end{bmatrix},$$

$$b := \begin{bmatrix} b_1 \\ \vdots \\ b_M \end{bmatrix}, \quad p_{min} := \begin{bmatrix} p_{1,0} \\ \vdots \\ p_{M,0} \end{bmatrix}, \quad p_{max} := \begin{bmatrix} p_{1,m_1} \\ \vdots \\ p_{M,m_M} \end{bmatrix}.$$

Here, each a_j on the diagonal of A, is a vector $a_j \in \mathbb{R}^{m_j}$, and each b_j in b, is a vector $b_j \in \mathbb{R}^{m_j}$.

As presented in Thorat and Skjetne (2018), the constraints in the linear programming optimization problem are included because,

- (5.19b) together with the objective function (5.19a), ensures minimization of the specific fuel consumption at each instance.
- (5.19c) ensures that enough power is provided by the connected gensets to satisfy the load demand.
- (5.19d) ensures that the rate of power change is within an accepted range.
- (5.19e) ensures that the connected gensets are within the power limitations and that disconnected gensets provide zero power.

Fuel Consumption Optimization

When considering the piecewise quadratic fuel consumption curve, the optimization problem becomes nonlinear. As presented by Skjetne (2021), when modifying the constraint in Equation 5.19b, the nonlinear optimization problem with objective to minimize fuel consumption becomes

$$\begin{aligned}
\min_{p,\mu} \quad & c^T \mu && \text{(5.20a)}\\
\text{s.t.} \quad & A(P_b \circ p \circ p) + B(P_b \circ p) + E\mu \leq 0, && \text{(5.20b)}\\
& (c \circ P_b)^T p = P_{load}, && \text{(5.20c)}\\
& c \circ (p_j^- - \Delta p) \leq p \leq c \circ (p_j^- + \Delta p), && \text{(5.20d)}\\
& c \circ p_{min} \leq p \leq c \circ p_{max}, && \text{(5.20e)}
\end{aligned}$$

where the constraint in (5.20b) together with the objective in (5.20a) ensures the minimization of the piecewise quadratic FOC curves. The matrix B is defined as

$$B := \begin{bmatrix} b_1 & 0_{m_1 \times 1} & \cdots & 0_{m_1 \times 1} \\ 0_{m_2 \times 1} & b_2 & \dots & 0_{m_2,1} \\ \vdots & \vdots & \ddots & \vdots \\ 0_{m_j \times 1} & 0_{m_j \times 1} & \cdots & b_M \end{bmatrix}.$$

5.4.2 Hybrid-Electric Optimization

When considering a hybrid-electric power plant consisting of either a configuration with gensets and battery or fuel cell and battery, the state vector of the problem becomes

$$x = \begin{bmatrix} p_1 & p_2 & \dots & p_M & \mu_1 & \mu_2 & \dots & \mu_M & C\_rate \end{bmatrix}^T. \tag{5.21}$$

To obtain the SFOC-optimization problem for the hybrid-electric model, (5.19) is combined with the battery limitations in (5.16). The optimization problem becomes

$$\begin{aligned}
\min \quad & c^T \mu && \text{(5.22a)} \\
\text{s.t.} \quad & Ap + E\mu \leq -b, && \text{(5.22b)} \\
& (c \cdot P_b)^T p + Q_{nom} C_rate = P_{load}, && \text{(5.22c)} \\
& c \circ (p_j^- - \Delta p) \leq p \leq c \circ (p_j^- + \Delta p) && \text{(5.22d)} \\
& c \circ p_{min} \leq p \leq c \circ p_{max}, && \text{(5.22e)} \\
& C_rate_{min} \leq C_rate \leq C_rate_{max}, && \text{(5.22f)} \\
& \frac{SOC_0 - SOC_{max}}{\Delta t} \leq C_rate \leq \frac{SOC_0 - SOC_{min}}{\Delta t}. && \text{(5.22g)}
\end{aligned}$$

Here, the extra term in 5.22c is the power delivered/consumed by the battery, 5.22f represents the C-rate limits, and 5.22g represents the SOC limits derived from the relation between SOC and C-rate. In Appendix A, the matrices of an example system as Equation 5.22 are written out.

Correspondingly, the FOC optimization becomes

$$\begin{aligned}
\min_{p,\mu} \quad & c^T \mu && \text{(5.23a)} \\
\text{s.t.} \quad & A(P_b \circ p \circ p) + B(P_b \circ p) + E\mu \leq 0, && \text{(5.23b)} \\
& (c \circ P_b)^T p + Q_{nom} C_rate = P_{load}, && \text{(5.23c)} \\
& c \circ (p_j^- - \Delta p) \leq p \leq c \circ (p_j^- + \Delta p), && \text{(5.23d)} \\
& c \circ p_{min} \leq p \leq c \circ p_{max}, && \text{(5.23e)} \\
& C_rate_{min} \leq C_rate \leq C_rate_{max}, && \text{(5.23f)} \\
& \frac{SOC_0 - SOC_{max}}{\Delta t} \leq C_rate \leq \frac{SOC_0 - SOC_{min}}{\Delta t}. && \text{(5.23g)}
\end{aligned}$$

Note that the genset and hybrid-electric optimizations can be used for a fuel cell by changing the genset input parameters to correspond to the characteristics of the fuel cell.

5.5 Optimization Over a Horizon

Concerning a load profile that is divided into sequences of constant load with a corresponding time interval, the instantaneous optimization may lead to a deterioration of fuel consumption for the subsequent interval. This encourages optimizing over a horizon, N, where the optimized values at each instance concern the fuel consumption over the whole horizon.

5.5.1 Genset SFOC-Optimization

When concerning the horizon, it is best from a programming view to collect the states in time-instant vectors,

$$\mathbf{p} := \text{col}(p_{1,1}, p_{1,2}, \dots, p_{1,M}, p_{2,1}, p_{2,2} \dots, p_{2,M}, p_{N,1}, p_{N,2} \dots, p_{N,M}) \in \mathbb{R}^{MN} \tag{5.24a}$$

$$\boldsymbol{\mu} := \text{col}(\mu_{1,1}, \mu_{1,2}, \dots, \mu_{1,M}, \mu_{2,1}, \mu_{2,2} \dots, \mu_{2,M}, \mu_{N,1}, \mu_{N,2} \dots, \mu_{N,M}) \in \mathbb{R}^{MN} \tag{5.24b}$$

$$\boldsymbol{\xi} := \text{col}(\xi_1, \xi_2, \dots, \xi_N) \in \mathbb{R}^{(2M)N} \tag{5.24c}$$

$$\boldsymbol{\tau} := \text{col}(\Delta t_1, \Delta t_2, \dots, \Delta t_N) \in \mathbb{R}^{N} \tag{5.24d}$$

$$\mathbf{c} := \text{col}(c_{1,1}, c_{1,2}, \dots, c_{1,M}, c_{2,1}, c_{2,2} \dots, c_{2,M}, c_{N,1}, c_{N,2} \dots, c_{N,M}) \in \mathbb{R}^{MN} \tag{5.24e}$$

$$\mathbf{P}_{Load} := \text{col}(P_{Load,1}, P_{Load,2}, \dots, P_{Load,N,M}) \in \mathbb{R}^{N} \tag{5.24f}$$

$$\tag{5.24g}$$

where $\xi_k = (p_k, \mu_k) \in \mathbb{R}^{2M}$ is the transposed state vector for each time instance. In the optimal solution ξ_k^*, the optimal total fuel consumption is expressed by $c_k^T \mu_k^* \Delta t_k$. The cost function, $c^T \mu$, is expressed as the sum of each instant over the horizon, i.e.,

$$\min f(\boldsymbol{\xi}) = \min \sum_{k=1}^{N} c_k^T \mu_k \Delta t_k = \mathbf{c}^T (diag(\boldsymbol{\tau}) \otimes I_M) \boldsymbol{\mu}. \tag{5.25}$$

The constraints must also be defined over the horizon. Here, it is important to note that the genset rate-constraints become dependent on the previous load instance. Starting with the first constraint in the SFOC-optimization, it can be expressed as

$$(A \otimes I_N)\mathbf{p} + (E \otimes I_N)\boldsymbol{\mu} \leq -b \otimes 1_N \tag{5.26}$$

where $\otimes$ is the Kronecker product.

Further, the constraints are similarly defined for both approaches. The load balance constraints are defined as

$$(I_N \otimes P_b^T) diag(\mathbf{c})\mathbf{p} = \mathbf{P}_{Load}, \tag{5.27}$$

for genset optimization. The genset limiations can be expressed as

$$diag(\mathbf{c})(1_N \otimes p_{min}) \leq \mathbf{p} \leq diag(\mathbf{c})(1_N \otimes p_{max}). \tag{5.28}$$

Since the rate constraint is dependent on the previous state, the easiest way to define the constraint over the horizon is in matrix form. Hence, the constraints can be expressed as

$$\begin{bmatrix} -I_M & 0 & \dots & 0 \\ diag(c_2) & -I_M & \dots & 0 \\ \vdots & \ddots & \ddots & 0 \\ 0 & 0 & diag(c_n) & -I_M \end{bmatrix} \mathbf{p} \leq \begin{bmatrix} c_1 \circ (\Delta p \Delta t_1 - p_0) \\ c_2 \circ \Delta p \Delta t_2 \\ \vdots \\ c_N \circ \Delta p \Delta t_N \end{bmatrix}, \tag{5.29}$$

$$\begin{bmatrix} I_M & 0 & \dots & 0 \\ -diag(c_2) & I_M & \dots & 0 \\ \vdots & \ddots & \ddots & 0 \\ 0 & 0 & -diag(c_n) & I_M \end{bmatrix} \mathbf{p} \leq \begin{bmatrix} c_1 \circ (\Delta p \Delta t_1 + p_0) \\ c_2 \circ \Delta p \Delta t_2 \\ \vdots \\ c_N \circ \Delta p \Delta t_N \end{bmatrix}. \tag{5.30}$$

5.5.2 FOC-Optimization

The constraints related to the piecewise linear curves in Equation 5.26 in the SFOC-optimization are the only constraints that are different for the FOC-optimization. Here it is expressed as a nonlinear constraint concerning the piecewise quadratic FOC-curves instead,

$$(A \otimes I_N)(\mathbf{p} \circ \mathbf{p} \circ (P_b \otimes 1_N)) + (B \otimes I_N)(\mathbf{p} \circ (P_b \otimes 1_N)) + (E \otimes I_N)\boldsymbol{\mu} \leq 0. \tag{5.31}$$

5.5.3 Hybrid-Electric Optimization

If the optimization over a horizon concerns a hybrid-electric power plant, the C-rate must be defined as the other vectors, the load balance must include the battery power and the battery constraints must be defined. Thus,

$$\mathbf{C\_rate} := \text{col}(C\_rate_1, C\_rate_2, \dots, C\_rate_N) \in \mathbb{R}^N, \tag{5.32a}$$

$$\boldsymbol{\xi} := \text{col}(\xi_1, \xi_2, \dots, \xi_N) \in \mathbb{R}^{(2M+1)N}, \tag{5.32b}$$

where $\xi_k = (p_k, \mu_k, C\_rate_k) \in \mathbb{R}^{2M+1}$ is the transposed state vector for each time instance.

The load balance constraints are then defined as

$$(I_N \otimes P_b^T) diag(\mathbf{c})\mathbf{p} + Q_{nom}\mathbf{C\_rate} = \mathbf{P}_{Load}, \tag{5.33}$$

for the hybrid-electric case. The rate limitations are defined as

$$1_N \otimes C\_rate_{min} \leq \mathbf{C\_rate} \leq 1_N \otimes C\_rate_{max}. \tag{5.34}$$

The state of charge limitations are dependent on the previous state and can be expressed as

$$T_1\mathbf{C\_rate} \leq 1_N \otimes (SOC_{max} - SOC_0) \tag{5.35}$$

$$T_2\mathbf{C\_rate} \leq 1_N \otimes (SOC_0 - SOC_{min}), \tag{5.36}$$

where T_1 and T_2 are two matrices containing the time intervals such that all SOC limits can be expressed with SOC_0 as the limitation. The matrices are expressed as

$$T_1 := \begin{bmatrix} -\Delta t_1 & 0 & 0 & \dots & 0 \\ -\Delta t_1 & -\Delta t_2 & 0 & \dots & 0 \\ -\Delta t_1 & -\Delta t_2 & -\Delta t_3 & \dots & 0 \\ \vdots & \vdots & \vdots & \ddots & \vdots \\ -\Delta t_1 & -\Delta t_2 & -\Delta t_3 & \dots & -\Delta t_N \end{bmatrix}, T_2 := \begin{bmatrix} \Delta t_1 & 0 & 0 & \dots & 0 \\ \Delta t_1 & \Delta t_2 & 0 & \dots & 0 \\ \Delta t_1 & \Delta t_2 & \Delta t_3 & \dots & 0 \\ \vdots & \vdots & \vdots & \ddots & \vdots \\ \Delta t_1 & \Delta t_2 & \Delta t_3 & \dots & \Delta t_N \end{bmatrix} \tag{5.37}$$

In Appendix A, the hybrid-electric FOC-optimization problem over a horizon is exemplified, and the corresponding Matlab code used in subsequent calculations is attached in Appendix B.

5.5.4 Slack Variables

When having an optimization problem with strict constraints, a slack variable can be included to find a suboptimal solution. To avoid infeasibility if the load increases faster than the power source dynamics, a slack variable is included in the load balance-constraint. The use of the slack variable is penalized in the objective function to ensure that the engines deliver the load demand when needed, without exploiting the slack. The objective function then becomes

$$f(\xi) = \mathbf{c}^T(diag(\boldsymbol{\tau}) \otimes I_M)\boldsymbol{\mu} + w^T\mathbf{s}. \tag{5.38}$$

Here, $\mathbf{s} \in \mathbb{R}^N$ is the slack variable vector, and $w \in \mathbb{R}^N_{\leq 0}$ is a vector of weights penalizing the use of slack. Further, the load balance constraint becomes

$$(I_N \otimes P_b^T)diag(\mathbf{c})\mathbf{p} + Q_{nom}\mathbf{C\_rate} + s = \mathbf{P}_{Load}. \tag{5.39}$$

Chapter 6

Case Study: Trondheimsfjord I

A case study is defined in terms of a high-speed passenger ferry with a fixed voyage schedule. The vessel Trondheimsfjord I is chosen for the case study, with diesel-mechanical propulsion as a basis. First, the design properties are presented, and the route-specific load profiles are synthesized. Then, the power configuration is presented in an SLD. Based on the load profile, an engine speed profile is defined to enable fuel consumption calculations. In the subsequent chapters, alternative power plants are suggested and compared to the diesel-mechanical solution.

6.1 Trondheimsfjord I

Trondheimsfjord I is a high-speed catamaran operating passenger voyages between Trondheim and Brekstad, Norway. It is owned by FosenNamsos Sjø AS and was built in the year 2008. The vessel is shown in Figure 6.1, and its design parameters are listed in Table 6.1. The original propulsion system consisted of two MAN diesel engines, each mechanically connected to a propeller through a servogear. In 2013/2014, the propellers were replaced with waterjets, and the MAN engines were replaced with two MTU engines.

Figure 6.1: Trondheimsfjord I (Marine Traffic, 2021)

Table 6.1: Trondheimsfjord I: Design parameters (Brødrene Aa (2021), MTU (2019))

Length [m]	24.5
Width [m]	8.0
Service speed [kn]	32.5
Engine	MTU 12V 2000 M72
Gearbox type	ZF 3050
Waterjet	Rolls-Royce Kamewa 50 A3
Fuel oil capacity [L]	4000

In 2017 the MTU diesel engines were the most common power sources onboard high-speed passenger ferries around the world (Dietrich, 2017). The main specifications of the MTU 12V 2000 M72 engine are listed in Table 6.2 and the engine's specific fuel consumption is obtained from MTU (2006).

Table 6.2: MTU 12V 2000 M72 Specifications (MTU, 2019)

Engine dimensions (l x w x h) [mm^3]	3240 x 1360 x 1460
Dry engine with gearbox weight [kg]	3680
Engine rated power [kW]	1080
Engine speed [rpm]	2250
Engine ramp-up rate [1)] [kW/s]	135

[1)] This parameter is not given in the specification sheet and is based on the assumption that the engine can go from 0-100% of MCR within 8 seconds.

6.2 Route and Load Profile

The geographic route operation of Trondheimsfjord I is illustrated in Figure 6.2, and the voyage schedule is presented in Table 6.3. With the information from the voyage schedule and assumptions concerning engine load in different operation modes, an approximate load profile was synthesized.

Figure 6.2: Route of operation for Trondheimsfjord I (Marine Traffic, 2021)

Table 6.3: Voyage schedule for Trondheimsfjord I (AtB, 2021)

Trondheim	Lensvik	Hasselvika	Brekstad	**Brekstad**	Hasselvika	Lensvik	Trondheim
06:20	-	07:05	07:20	**07:30**	07:40	07:55	08:35
10:20	-	-	11:10	**11:20**	-	-	12:10
14:45	15:20	15:40	15:55	**16:05**	16:15	-	17:05
18:45	19:20	-	19:45	**20:00**	-	-	20:50

In order to obtain a load profile close to reality, the crew of the vessel was contacted to establish how much time is used for each operating mode. Based on the conversation, the maneuvering time was set to two minutes in Trondheim and Brekstad, and one minute in Lensvik and Hasselvika. Further, the acceleration phase takes 30 seconds when the engines are hot. The short stops in Lensvik and Hasselvika were set to 60 seconds. Assuming the engines are operated at the optimal operating point during transit, i.e., when the specific fuel consumption is at its minimum, 70-75% of MCR was chosen for this operation mode. Based on Wu (2017) the load in port was set to 9% of MCR. During acceleration, the load is typically close to MCR and was therefore set to 90%. Table 6.4 outlines the assumed MCRs for the load conditions. For the given voyage schedule and previously mentioned assumptions, Figure 6.3a and Figure 6.3b illustrate the synthetic operational load profile for a whole day and a specific voyage, respectively.

Table 6.4: Load profile characteristics

Load condition	[% of MCR]
Maneuvering	20
Acceleration	90
Transit	70- 75
In port	9

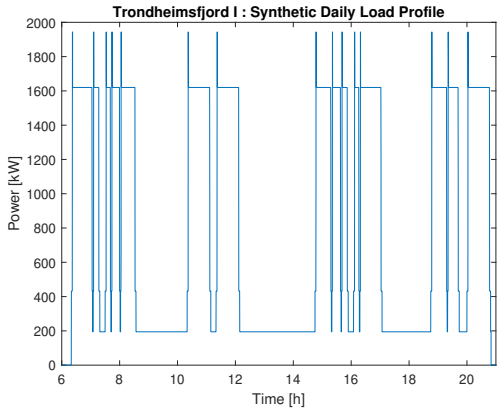

(a) Synthetic load profile for daily operation

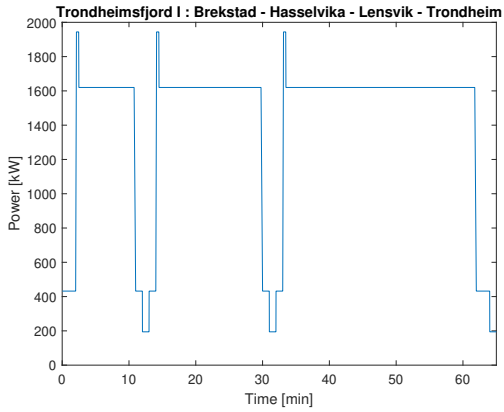

(b) Synthetic load profile for a specific route

Figure 6.3: Synthetic load profiles

These load profiles are, however, not completely realistic as they do not consider the dynamic fluctuations in typical load profiles. On a mission guidance level, these fluctuations can be reasonably neglected as this can be considered the task of the local PMS. The main task working with the VMMS and EEMS is to optimally satisfy the overall energy demand, and even the short-term acceleration phase can in some cases be neglected for more stable optimization. On the mission guidance level, the load profiles could consider longer time horizons, which is applied by increasing the sampling time. Figure 6.4 shows a load profile over 56 minutes, concerning a single-stage load with a sampling frequency of 2 minutes.

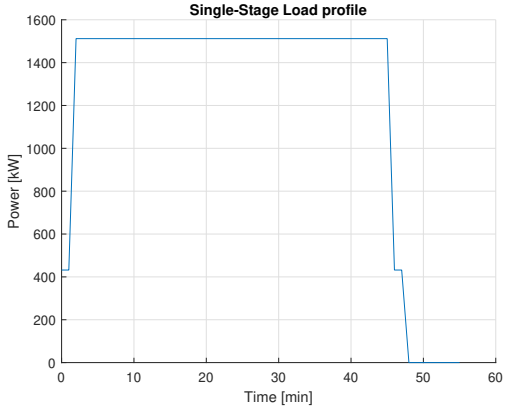

Figure 6.4: Single-stage load profile for mission guidance

6.3 Key Performance Indicators

Key performance indicators (KPIs) are used as a measurement to evaluate and analyze how good a result is. When the KPIs are well-defined, it is easy to compare the solutions to different problems. Examples of typical KPIs concerning hybrid power plants are:

- Fuel consumption
- Emissions
- Total cost
- Running hours of gensets
- Energy supplied by the battery

The KPI on fuel consumption is the main consideration in this thesis.

6.4 Diesel-Mechanical Power System

The baseline model of the case study is a diesel-mechanical power system obtained from specifications from Trondheimsfjord I. The single-line diagram for the power configuration is shown in Figure 6.5. When there are two diesel engines, each directly connected to a propulsor, the common practice is to run these engines at the same speed. This is due to the direct relation to the thrust and thus the propulsion efficiency of the vessel. The worst-case scenario with unequal loadsharing on the engines might be a counteract between the two propulsors, resulting in a reduction of thrust. Hence, equal loadsharing is the baseline for a high-speed catamaran with separate power systems in each hull.

In a diesel-mechanical power plant, the engine's rotational speed and the rotational speed of the waterjet impeller are directly connected. An engine speed profile should therefore be included in addition to the load profile in order to calculate the fuel consumption. This speed profile was approximated from a diagram plotting the relation between vessel speed, engine speed, and engine power. With known power and vessel speed, the engine speed is chosen. The diagrams used were from another Kamewa waterjet, Kamewa 71SII, and approximations were conducted from scaling relations. The diagrams were obtained from the waterjet contractors, protected by confidentiality agreements, and are thus not replicated here. A short load profile considering all operation modes and the resulting engine speed profile corresponding are shown in Figure 6.6.

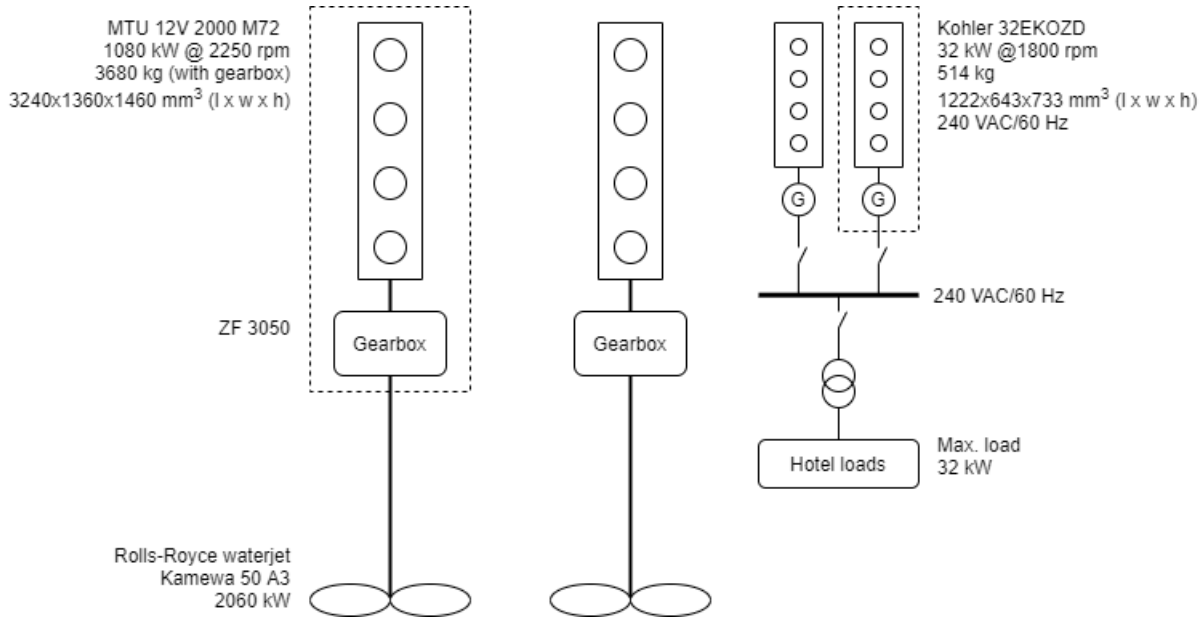

Figure 6.5: SLD of diesel-mechanical configuration

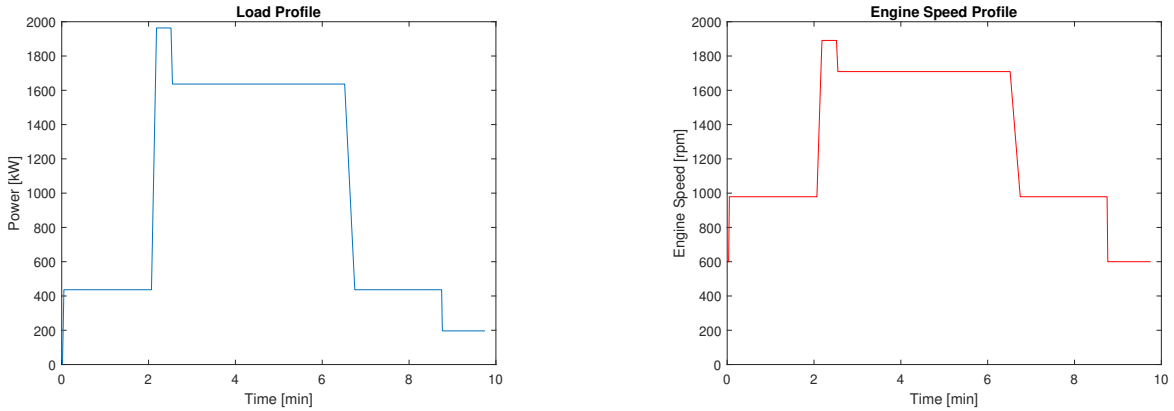

(a) Short load profile considering all operation modes

(b) Corresponding engine speed profile

Figure 6.6: Load and engine speed profiles

A diesel-mechanical power system is a configuration with few components. From engine to propulsor, the only component is the gearbox, which imposes a loss of approximately 1% (Moghadam and Nejad, 2020). This is included in the engine load profile in Figure 6.6.

From the load and speed data, the specific fuel consumption for each instance and the corresponding total fuel consumption can be calculated. The specific fuel consumption curve for the engines is specified in the performance diagram from the manufacturer (MTU, 2006). This diagram is confidential and not replicated here. From the diagram, a lookup table with engine speed and power as input values can be made. Since the performance diagram has three intersecting sections dependent on the sequential turbocharging, three separate lookup tables were synthesized. These look-up tables will not be exact enough to reproduce the performance diagram and are presented in Appendix C.

Due to the lack of independence to optimize the loadsharing, it is reasonable to investigate how the results change when the diesel engines are put on a grid in a diesel-electrical configuration. This solution

will detach the direct connection to the propulsors, allowing the engines to share the load to achieve optimal fuel consumption. However, a DE solution will include more components, possibly increasing the weight and losses in the system. This motivates an evaluation of how these two factors impact the total fuel consumption compared to the conventional solution.

Chapter 7

Suggested Power System Alternatives for Trondheimsfjord I

A presentation of the alternative power plant configurations suggested to replace the conventional DM solution in Trondheimsfjord I is given, including the power transmission losses related to these.

7.1 Diesel-Electric Power System

The diesel engines from the baseline case in Chapter 6 are placed on a DC bus in a diesel-electric configuration to enable optimization of the loadsharing, with aim to reduce fuel consumption. The single-line diagram for the diesel-electric power system is shown in Figure 7.1. The three separate systems from the diesel-mechanical configuration are merged onto an electrical switchboard. The two auxiliary engines from the diesel-mechanical power system are neglected, assuming that the two main engines can handle the increased power demand from the hotel loads.

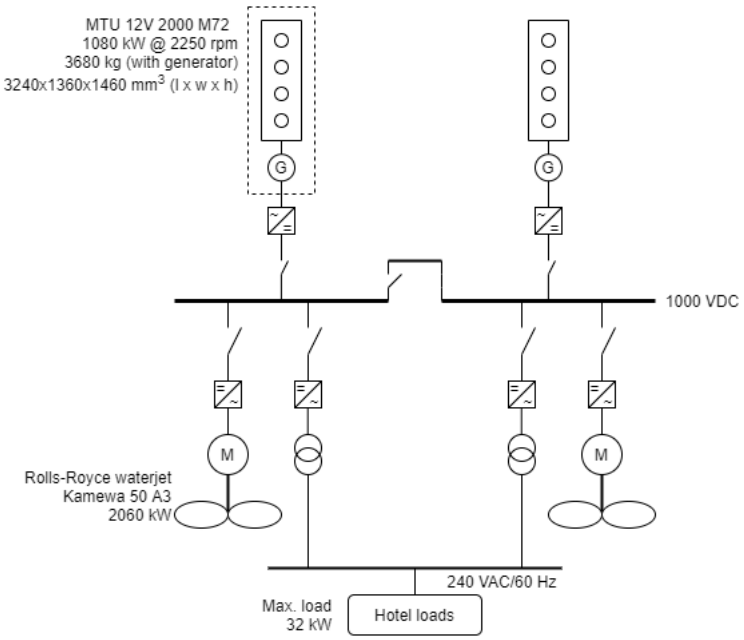

Figure 7.1: SLD of diesel-electric configuration

It should be noted that the weight and volume specifications of the genset are based on a rough assump-

tion that the generator will contribute with a weight and volume similar to the gearbox. Also, the weight and volume of the remaining power converting devices are neglected.

The parameter values important for modeling the power system are presented in Table 7.1.

Table 7.1: Case specific parameter values for DE power system

Parameter	Value
M	2
c	$[1\ 1]^T$
$P_{b,j}$	[1080 1080]
Δp	[0.125 0.125]

7.1.1 SFOC- and FOC-curves

First, a known SFOC-curve for a fixed-speed solution is presented. Fixed-speed solutions are the common case for AC grid solutions, where the grid requires a constant frequency. Since the two engines in Trondheimsfjord I are equal, they also have the same specific fuel consumption curves, which simplifies the optimization problem. Due to the known characteristics of the SFOC-curve, the optimization algorithm should return an equal loadsharing solution for load instances above the inflection point, and return a solution where one engine delivers the whole load when the load is within the engine's MCR and below the inflection point. This curve can be used as an example for comparing the results when using different solvers, such as the interior-point algorithm and genetic algorithm, as the expected result is known. The specific fuel consumption and fuel consumption curves for each engine are shown in Figure 7.2.

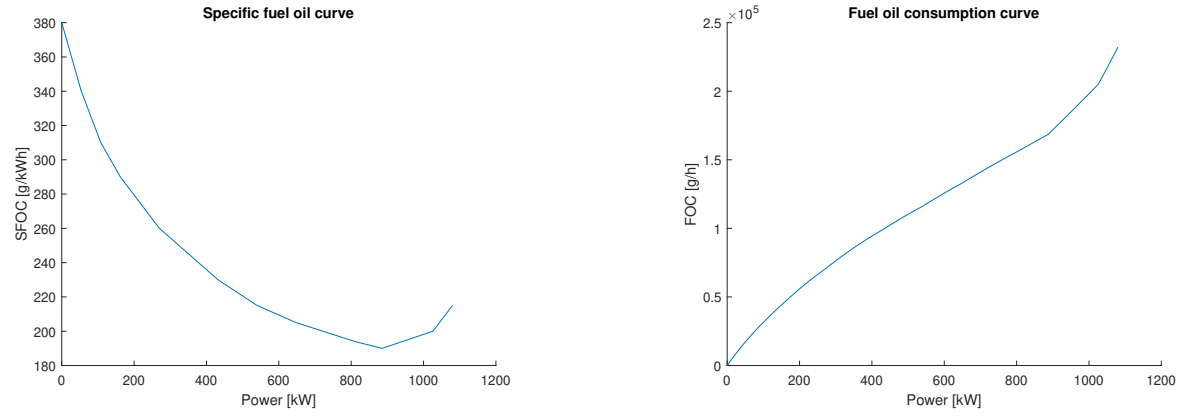

(a) Specific fuel consumption curve

(b) Fuel consumption curve

Figure 7.2: Fixed-speed fuel consumption curve

From Figure 7.2, it can be observed that the inflection point of the fuel consumption curve corresponds to the minimum specific fuel consumption. Hence, the inflection point is at 82% MCR, at 885.6 kW. A contour plot, as in Figure 7.3, illustrates this well. Here fuel consumption increases as the colors go from purple to yellow.

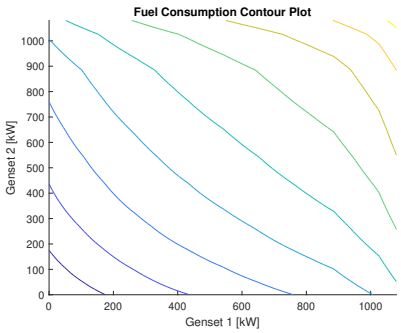

Figure 7.3: Contour plot illustrating loadsharing for fixed speed SFOC-curve

In order to compare the diesel-electric power plant to the conventional diesel-mechanical solution, the performance diagram and the engine's actual specific fuel consumption must be considered. By looking at a variable-speed configuration, the power delivered to the switchboard is independent of the propulsors' rotation speed. This is the common case for a DC grid solution. In order to simplify the optimization, it is assumed that the lowest SFOC for a given engine load will be selected, and the engine speed will always be satisfied. Hence, we obtain three convex SFOC-curves from the three different states. These SFOC-curves, and the corresponding FOC curves, are shown in Figure 7.4. An illustration of an SFOC-curve for variable-speed compared to fixed-speed is also shown in Zahedi et al. (2014).

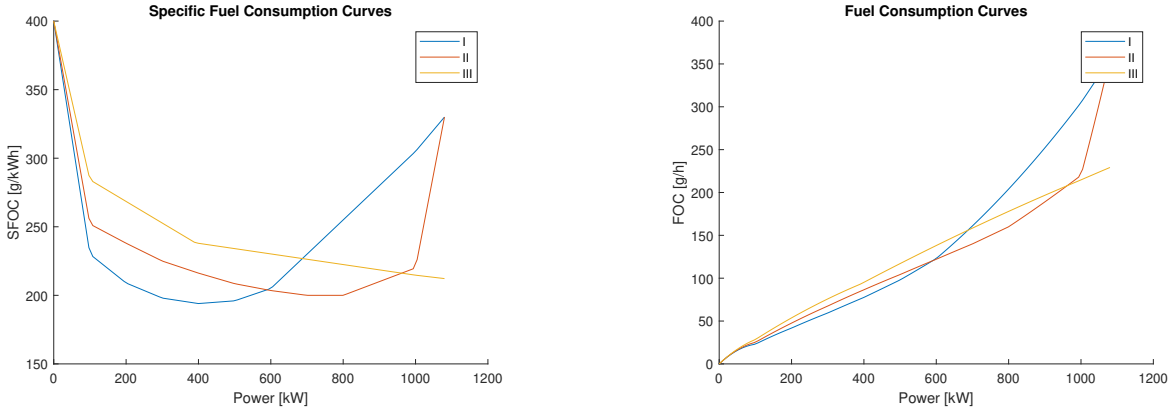

(a) Specific fuel consumption curves

(b) Fuel consumption curves

Figure 7.4: Variable speed SFOC- and FOC-curves

The datasets corresponding to the fixed-speed and variable-speed SFOC-curves are presented in Appendix C.

7.1.2 Power Transmission Losses

Since there are many additional components when considering diesel-electric propulsion, the losses must be included to have a realistic foundation for comparison with the diesel-mechanical solution. The efficiency of the components varies depending on the power flow. The variations are, however, disregarded in this thesis, and the efficiencies are considered constant factors. This is considered a reasonable assumption as the change in efficiency typically is small. The general efficiencies for diesel-electric power plants, as shown in Figure 2.18, are used as a basis to determine the efficiencies for the components in the diesel-electric power plant. Rounding up the switchboard efficiency to 1, the load profile observed by the diesel engine is

$$P_{Load,DE} = \left(\frac{P_{Load}}{\eta_{El} \cdot \eta_{conv}} + \frac{P_{HotelLoad}}{\eta_{tr} \cdot \eta_{conv}} \right) / \left(\eta_G \cdot \eta_{conv} \right). \tag{7.1}$$

Here, η_{El} is the electric motor efficiency, η_{conv} is the converter efficiency, η_{tr} is the transformer efficiency and η_G is the generator efficiency. The values are presented in Table 7.2.

Table 7.2: Component losses in DE power system

η_{El}	0.96
η_{conv}	0.985
η_{tr}	0.995
η_G	0.96

7.2 Battery-Electric Power System

In order to design a power configuration for battery-electric operation, it is required that the battery can satisfy the load profile demands. This problem differs from the other configurations as the objective is to find a suitable configuration based on the load profile, rather than optimizing the use of a predefined power plant. In other words, the aim is to find the right battery setup.

7.2.1 Battery Dimensioning Limiting Factors

The limiting factors when choosing a battery-electric system are energy and power demands. Since the battery dynamics are much faster than the diesel engine, it is assumed that there are no ramp up-limitations on the battery. By integrating the load profile over time, the energy demand is obtained. Further, the maximum power demand is defined by the baseline model's MCR, by requiring that the battery should be able to deliver the same power as the conventional solution.

The limitations on the SOC must be considered, and the battery must be dimensioned to satisfy the energy demand within the allowed SOC range. With SOC_{max} and SOC_{min} set to 80 and 20%, respectively, the energy demand should represent 60% of the nominal energy capacity of the battery. Also, the energy capacity and maximum power should cover the hotel loads of the system, and this energy should be available at all times.

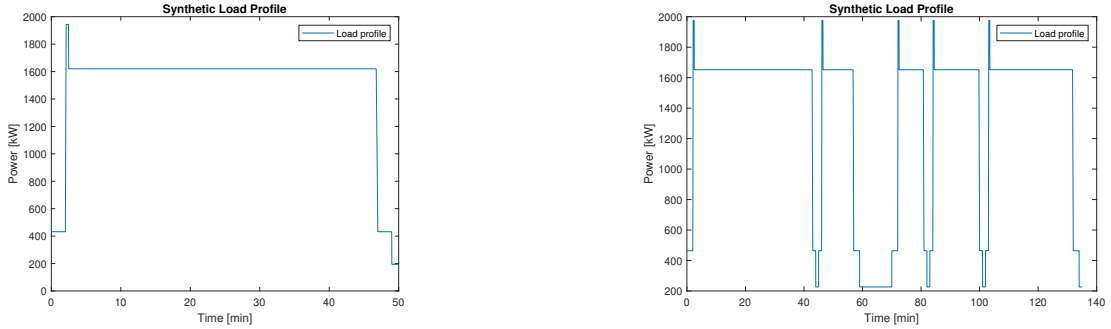

(a) Synthetic single-stage load profile

(b) Synthetic multi-stage load profile

Figure 7.5: Load profiles for battery dimensioning

By calculating the energy demand needed to satisfy the most demanding single- and multi-stage synthetic load profiles, the battery dimensions can be selected. The most demanding single-stage load profile

is the voyage from Trondheim to Brekstad of 50 minutes, as shown in Figure 7.5a. Figure 7.5b shows the most demanding multi-stage load profile which is based on a department from Trondheim with a stop in Hasselvika before reaching Brekstad. In Brekstad, the vessel stays for 10 minutes before it returns to Trondheim via Hasselvika and Lensvik. The whole voyage takes 2 hours and 15 minutes.

Since the synthetic load profile is constructed based on assumptions of a sampling frequency of one second, the minimum energy capacity of the battery can be calculated by summarizing the load at each time instance,

$$Q_{nom,min} = \frac{1}{3600} \sum_{t} P_{Load}(t) \cdot \frac{1}{SOC_{max} - SOC_{min}}, \tag{7.2}$$

where 1/3600 is introduced to convert the unit from kilowatt-seconds to kilowatt-hours. These calculations are based on the assumption that all the energy stored in the battery can be delivered to the propulsor. In other words, neglecting power transmission losses. The power losses are defined and accounted for at the end of this subsection. When considering the power demand, the basis is that the battery should at least deliver the same power as the baseline DM configuration.

Further, the multi-stage load profile involves a period of 10 minutes in port in between two voyages, where it is assumed that charging infrastructure is available. Hence, the total energy demand is reduced. The minimum energy capacity can then be calculated by adding the increase of SOC from charging,

$$SOC_{charge} = C\_rate_{charging} \cdot dt, \tag{7.3}$$

to the SOC-denominator of Equation 7.2.

Two different BESS options are presented as alternatives to satisfy the limiting factors from the load profile. Both BESSs are designed by Corvus Energy, the Dolphin Power ESS, and the Dolphin Energy ESS. The technical specifications of the BESSs are obtained from Corvus Energy (2020a) and Corvus Energy (2020b), and are presented in Table 7.3.

Table 7.3: BESS specifications

	Corvus Dolphin Power	**Corvus Dolphin Energy**
$\mathbf{Q}_{nom}$ (pack) [kWh]	54.6	77.0
C-rate$_{discharge}$ [C]	2.2	0.5
C-rate$_{charging}$ [C]	1.6	0.4
Weight (pack) [kg]	436.0	436.0
Volume (pack) (h x w x d) [mm^3]	2380 x 655 x 500	2380 x 655 x 500

Based on the battery pack specifications, the battery dimensions can be calculated based on energy or power demand. When concerning the energy demand, the number of packs needed to satisfy the energy demand is calculated by dividing the total energy demand by the nominal energy of one pack. By rounding up the result, the number of packs is defined. The maximum power the battery can deliver is the maximum C-rate multiplied by the total energy capacity. These results might, however, not satisfy the power demand, and thus the battery dimensions should be calculated based on power demand as well. Here, the total energy capacity is calculated from the power demand, as the maximum power divided by the maximum C-rate. The number of packs needed to satisfy the power demand is calculated as the ratio of total energy capacity by the pack energy capacity. Based on the calculations, the weight and volume of the solutions can be analyzed. The total weight is the product of the weight of a single pack and the number of packs, and the total volume is the product of the volume of a single pack and the number of packs, expressed as an increase in width.

The calculations should result in a power plant configuration as presented in Figure 7.6 or 7.7. The selection of BESS depends on which alternative yields the lightest and least voluminous configuration. In the SLD the constant M represents the number of packs needed, which is defined from the energy and power demands. This should not be confused with the M used in the genset model.

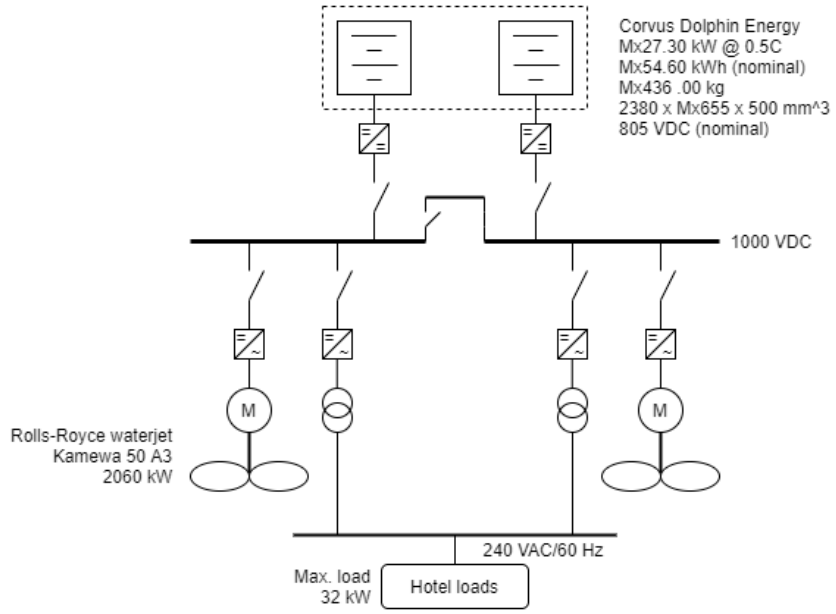

Figure 7.6: SLD of battery-electric configuration with Corvus Dolphin Energy packs

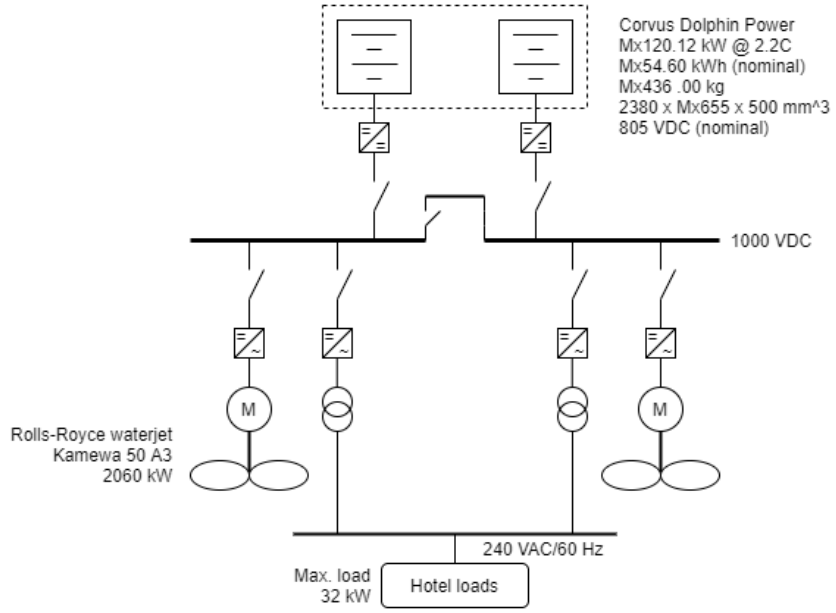

Figure 7.7: SLD of battery-electric configuration with Corvus Dolphin Power packs

7.2.2 Power Transmission Losses

The losses in a battery-electric configuration are similar to those in the DE solution, which are used as a basis to determine the efficiencies for the components in the battery-electric power plant. In addition, the charge and discharge energy efficiency of the battery must be considered. The load profile observed by the battery is

$$P_{Load,bat} = \left(\frac{P_{Load}}{\eta_{El} \cdot \eta_{conv}} + \frac{P_{HotelLoad}}{\eta_{tr} \cdot \eta_{conv}} \right) / \left(\eta_D \cdot \eta_{conv} \right). \tag{7.4}$$

Here, η_D is the discharge energy efficiency of the battery. Concerning the multi-stage case, the losses when charging the battery must also be considered. This can be done by including the charging efficiency, η_C, as a multiplicator to Equation 7.3. The efficiency values are presented in Table 7.4

Table 7.4: Component losses in BE power system

η_{El}	0.96
η_{conv}	0.985
η_{tr}	0.995
η_D	0.96
η_C	0.96

7.3 Hybrid-Electric Power System

When the power system involves a switchboard, the diesel engines can be combined with batteries in a hybrid configuration. The single-line diagram of the hybrid-electric power system is shown in Figure 7.8. In the suggested alternative, the diesel engines remain the same as the conventional and the BESS consists of three Corvus Dolphin Power packs. Concerning the battery dimensions, the power demand is the most important factor since the engines can charge the battery. This differs from the battery-electric vessel which is dependent on the shore power for charging.

The parameter values for modeling the hybrid-electric power system are presented in Table 7.5.

Table 7.5: Case specific parameter values for BE power system

Parameter	**Value**
M	2
c	$[1\ 1]^T$
$P_{b,j}$	[1080 1080]
Δp	[0.125 0.125]
Q_{nom}	360.60
C_rate$_{min}$	-1.6
C_rate$_{max}$	2.2

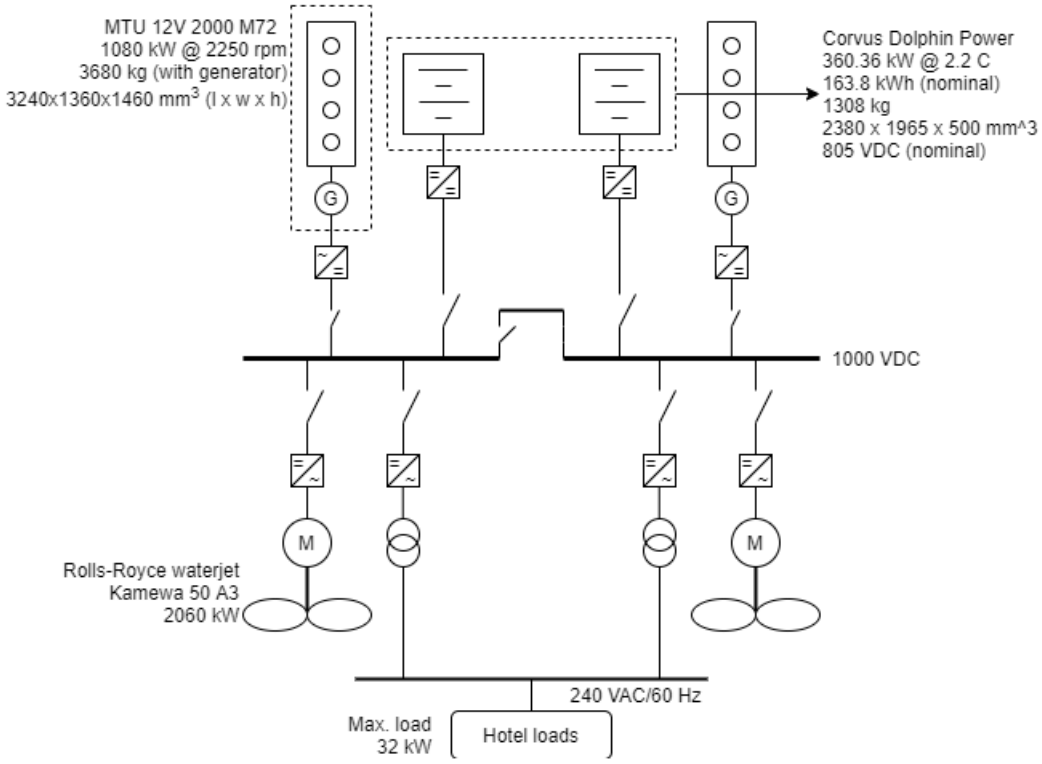

Figure 7.8: SLD of hybrid-electric configuration

7.3.1 Power Transmission Losses

When concerning hybrid-electric power systems involving batteries, it is important to consider the switch in efficiency when the battery changes from charging to discharging or vice versa. The efficiencies are presented in section 7.1 and 7.2. When the battery is charged, the main power flow becomes:

$$P_{bat} = \eta_C \cdot \eta_{conv} \cdot P_{C,fromgenset} \tag{7.5}$$

$$\begin{aligned} \frac{P_{Load}}{\eta_{El} \cdot \eta_{conv}} + \frac{P_{HotelLoad}}{\eta_{tr} \cdot \eta_{conv}} &= (P_G \cdot \eta_G \cdot \eta_{conv} + P_{C,fromgenset}) && (7.6a) \\ &= (P_G \cdot \eta_G \cdot \eta_{conv} + P_{bat} \cdot 1/(\eta_C \cdot \eta_{conv}) , && (7.6b) \end{aligned}$$

where, $P_{C,fromgenset}$ is the extra power the engines must deliver in order to charge the battery. Here, P_{bat} is negative. During discharge the main power flow becomes:

$$P_{bat} \cdot \eta_D \cdot \eta_{conv} = P_{D,toSWB} \tag{7.7}$$

$$\begin{aligned} \frac{P_{Load}}{\eta_{El} \cdot \eta_{conv}} + \frac{P_{HotelLoad}}{\eta_{tr} \cdot \eta_{conv}} &= (P_G \cdot \eta_{generator} \cdot \eta_{rectifier} + P_{D,toSWB}) && (7.8a) \\ &= (P_G \cdot \eta_{generator} \cdot \eta_{rectifier} + P_{bat} \cdot \eta_D \cdot \eta_{conv}) . && (7.8b) \end{aligned}$$

where, $P_{D,toSWB}$ is the power the batteries deliver during discharge. Here, P_{bat} is positive.

7.4 Zero-Emission Hybrid-Electric Power System

The zero-emission power source chosen to replace the diesel engines in this configuration is a PEM fuel cell. It should be noted that another option could be looking into ammonia engines, but since the technology of PEMFCs is better established, the fuel cell fueled on hydrogen was chosen as the zero-emission power system.

A Ballard FCWave fuel cell is selected. The technical specifications are obtained from Ballard (2020), and are replicated in Table 7.6.

Table 7.6: Ballard FCWave specifications

P$_{Rated}$ [kW]	200
Weight (Module) [kg]	875
Volume (Module) [mm^3]	1220 x 738 x 2200
Fuel type	Gaseous hydrogen

Based on these specifications, nine fuel cell modules are selected and combined with three Corvus Dolphin Power battery packs. This yields the SLD presented in Figure 7.9 for the zero-emission hybrid-electric power system.

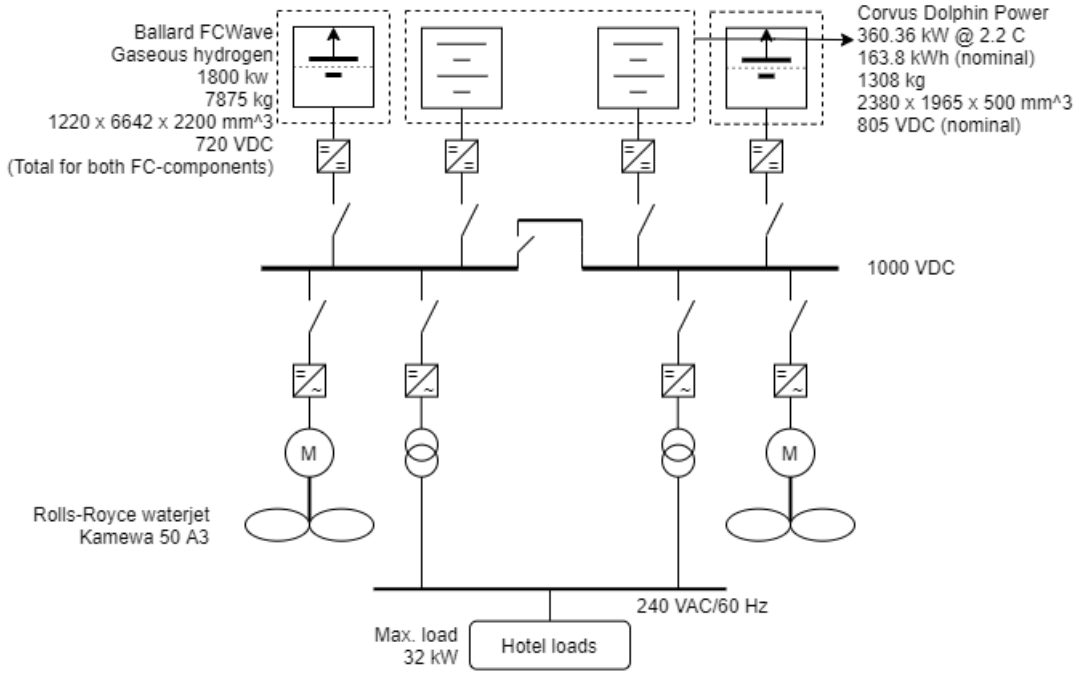

Figure 7.9: SLD of Zero-Emission Hybrid-Electric Configuration

The parameter values for modeling the hybrid-electric power system are presented in Table 7.7.

Table 7.7: Case specific parameter values for ZEHE power system

Parameter	Value
M	1
c	1
$P_{b,j}$	1800
Δp	1/30
Q_{nom}	360.60
C-rate$_{min}$	-1.6
C_rate$_{max}$	2.2

Here, M is equal to one due to the fact that the efficiency curve can be linearly scaled and all fuel cell modules can be modeled as one unit. The ramp-up rate is set to an approximate value, satisfying the theory of slower dynamics concerning fuel cells compared to diesel engines.

7.4.1 Power Transmission Losses

In a similar manner as in the hybrid-electric power system with diesel engines, the switch in efficiency when the battery changes from charging to discharging or vice versa must be considered. The efficiencies are presented in section 7.1 and 7.2. When the battery is charged, the main power flow becomes:

$$P_{bat} = \eta_C \cdot \eta_{conv} \cdot P_{C,fromFC} \tag{7.9}$$

$$\begin{aligned} \frac{P_{Load}}{\eta_{El} \cdot \eta_{conv}} + \frac{P_{HotelLoad}}{\eta_{tr} \cdot \eta_{conv}} &= (P_{FC} \cdot \eta_{conv} + P_{C,fromgenset}) && (7.10a) \\ &= (P_{FC} \cdot \eta_{conv} + P_{bat} \cdot 1/(\eta_C \eta_{conv}), && (7.10b) \end{aligned}$$

where P_{bat} is negative. During discharge the main power flow becomes:

$$P_{bat} \cdot \eta_D \cdot \eta_{conv} = P_{D,toSWB} \tag{7.11}$$

$$\begin{aligned} \frac{P_{Load}}{\eta_{El} \cdot \eta_{conv}} + \frac{P_{HotelLoad}}{\eta_{tr} \cdot \eta_{conv}} &= (P_{FC} \cdot \eta_{conv} + P_{D,toSWB}) && (7.12a) \\ &= (P_{FC} \cdot \eta_{conv} + P_{bat} \cdot \eta_D \cdot \eta_{conv}). && (7.12b) \end{aligned}$$

Here, P_{bat} is positive.

Chapter 8

Results

The results from the different methods of optimization and the results from the design calculations for battery-electric configuration are presented. First, the instantaneous FOC-optimization was run for the diesel-electric power system with two different solvers to test their performance. The best performing solver was selected for the other optimizations. Then, the fuel consumption of the conventional configuration and the diesel-electric power system were calculated for a short, single-stage load profile. Subsequently, the battery dimensions were calculated for the battery-electric power system concerning both a single-stage and a multi-stage load profile. Lastly, the SFOC- and FOC-optimization results over a horizon for the DE, HE, and ZEHE configurations with a fixed-speed SFOC-curve were calculated.

8.1 Interior-Point Method versus Genetic Algorithm

In this section, the results from the instantaneous FOC-optimization using interior-point and genetic algorithm solvers are presented. The optimization concerns the diesel-electric configuration, with the fixed speed SFOC-curve as input. Further, the best performing solver was used to calculate the fuel consumption of the diesel-electric configuration and the conventional power system, using the SFOC-data from the performance diagram. The load profile used in this section is the short load profile with all operation modes with a sampling time of 1 second from Section 6.4. The results from the interior-point optimization and the genetic algorithm optimization are shown in Figure 8.1 and Figure 8.3, respectively.

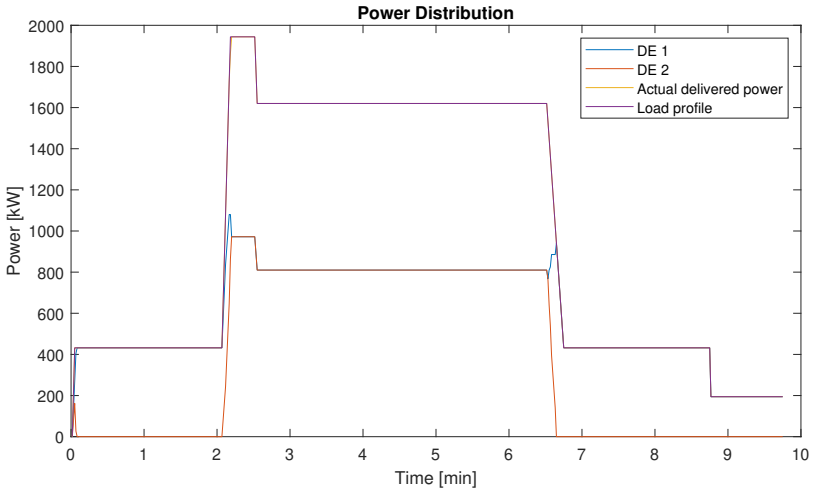

Figure 8.1: Fixed-speed optimization with interior-point algorithm

It can be observed that the interior-point optimization matches the SFOC-curve characteristics, ensuring that one genset delivers the entire load in the low-load maneuvering operation. Further, the load is shared equally when the load exceeds the inflection point in the acceleration and transit phase. A zoomed view of the second minute from the interior-point optimization is shown in Figure 8.2. This illustrates how the slack variable ensures that the optimization does not terminate if the previous state makes the change in power to the load demand too high. It also illustrates how the slack variable is not exploited.

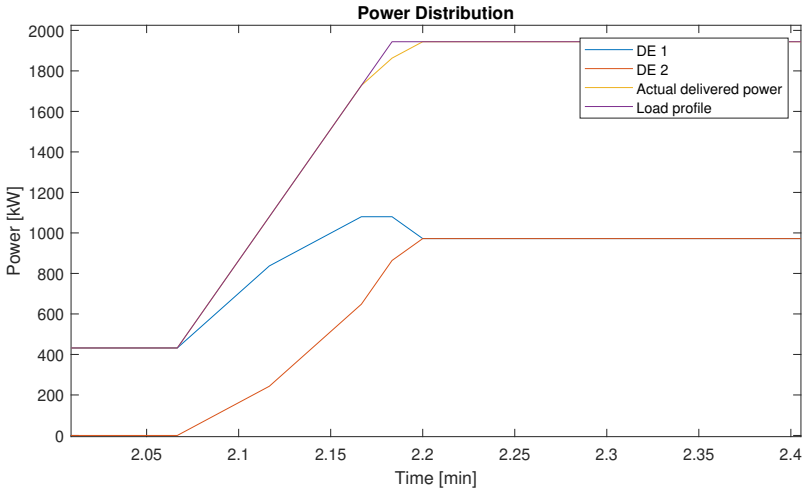

Figure 8.2: Zoomed in view of fixed-speed optimization with interior-point algorithm

As shown in Figure 8.3, the genetic algorithm optimization did not reach the most demanding load requirement in the acceleration phase. Hence, the slack variable was exploited. After the error accumulated for approximately 30 seconds, the algorithm terminated since it could not find a feasible point when the load demand decreased.

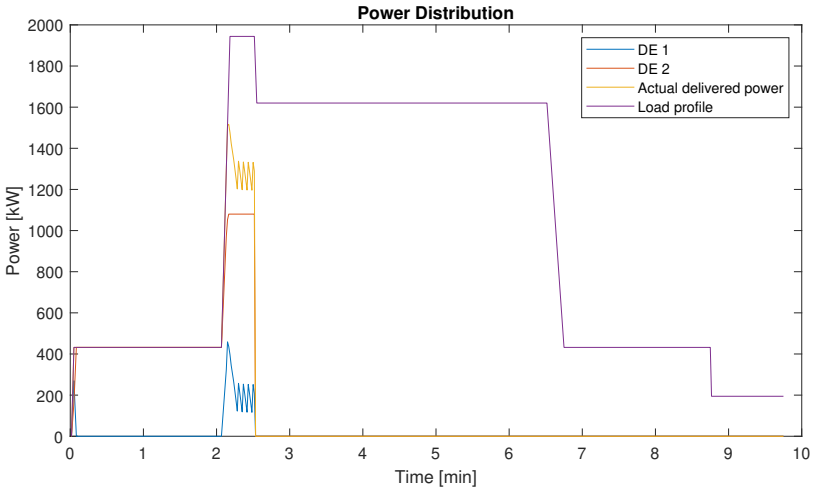

Figure 8.3: Fixed-speed optimization with genetic algorithm

The performance of the two algorithms considering a fixed-speed configuration with known SFOC-curve characteristics shows that the interior-point method performs as expected and that the GA does not satisfy the expectations. Thus, the interior-point method was chosen for further optimization problems.

8.2 Instantaneous Optimization Concerning DM and DE Power Systems

Concerning the instantaneous FOC-optimization for the case-specific performance diagram, the resulting fuel consumption for the DM solution and the DE configuration is presented.

8.2.1 Equal Loadsharing

For the DM configuration, the SFOC was calculated from each lookup table by double interpolation, for each load instance. Then, the lowest SFOC among the three was selected. The resulting total fuel consumption considering the short load profile and multi-stage load profile are presented in Table 8.1. The multi-stage load profile synthesizes a route from Trondheim to Brekstad via Lensvik and Hasselvika. The corresponding power distribution plots are shown in Figure 8.4.

Table 8.1: Total fuel consumption for diesel-mechanical power system

	Duration [min]	**Total fuel consumption [kg]**
Short load profile	9.75	33.17
Synthetic load profile (T-L-H-B)	70.00	345.49

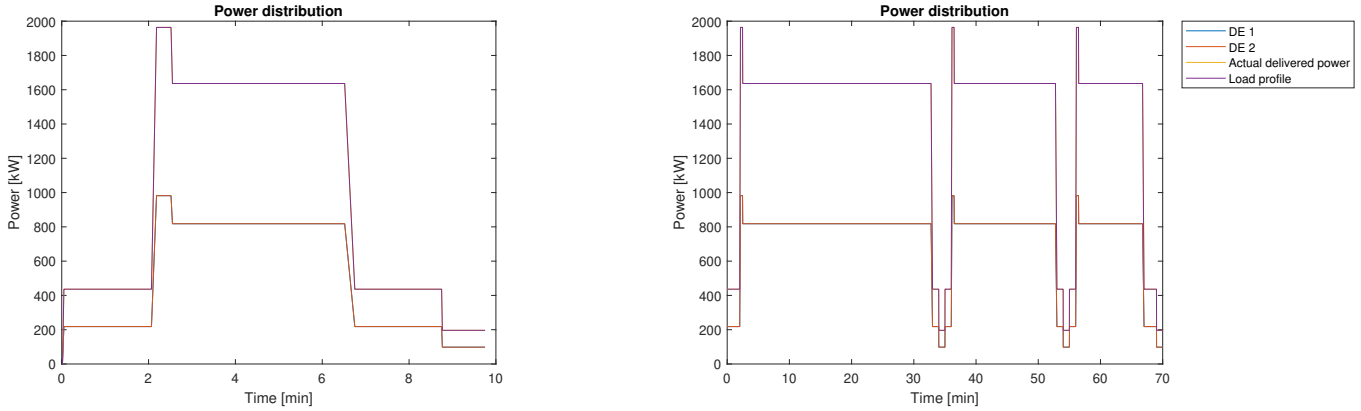

(a) Single-stage load profile

(b) Multi-stage load profile

Figure 8.4: Equal loadsharing concerning single- and multi-stage load profiles

8.2.2 Variable Speed Optimization

In the diesel-electric configuration, the instantaneous FOC-optimization, with the interior-point method and the previous state as input, was solved for each of the three variable-speed curves at each load instance. Then, the minimum specific fuel consumption value of the three states became the chosen state for the current instance and input to the next. This yielded the power distribution shown in Figure 8.5 for the short load profile.

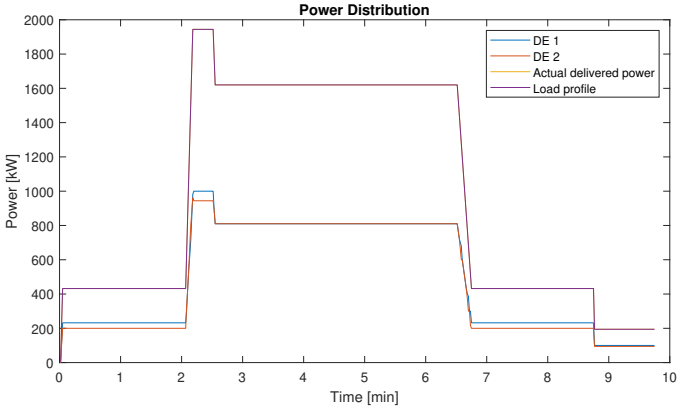

Figure 8.5: Variable speed optimization with interior-point algorithm

It is observed that the variable-speed optimization yields another loadsharing than for the fixed-speed optimization. The resulting fuel consumption is presented in Table 8.2. There, the result from the optimization run for the synthetic load profile is also presented. The result is not plotted due to the similar behavior for each stage as in the single-stage.

8.2.3 Variable-Speed Optimization Considering Component Losses

In the previous case, the hotel loads and component losses were neglected. In order to have a foundation for comparison with the diesel-mechanical solution, these factors must be included. Including the hotel loads and component losses yielded the power distribution shown in Figure 8.6.

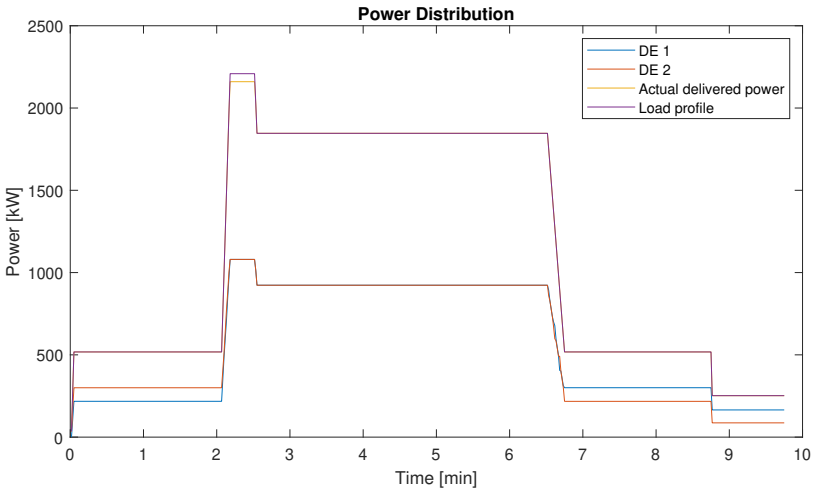

Figure 8.6: Variable speed optimization considering losses

It can be seen that the engines cannot provide enough power to satisfy the load demand in the acceleration phase when the losses are included. The resulting fuel consumption is presented in Table 8.2.

Table 8.2: Total fuel consumption for diesel-electric power system

	Duration [min]	**FOC [kg]** Lossless	**FOC [kg]** Incl. Losses and hotel loads
Short load profile	9.75	32.12	38.17
Synthetic load profile (T-L-H-B)	70.00	333.94	412.40

Comparing the results with the diesel-mechanical power system, the lossless optimization yielded a reduction of 3.2% and 3.3% for the single-stage and multi-stage load profiles, respectively. On the contrary, when the hotel loads and losses were included, the fuel consumption was increased by 15.1% for the single-stage load profile and 19.4% for the multi-stage load profile.

8.3 Battery-Electric Power System Dimensions

The battery-electric power system was dimensioned based on the most demanding single- and multi-stage load profiles.

8.3.1 Single-Stage Load Profile

The results presented in this subsection define the battery dimensions needed to satisfy the most demanding single-stage route of the vessel, presented in section 7.2.

Lossless Power Transmission

Based on the load profile the lossless battery configuration should have an energy capacity of 2120 kWh and deliver 2192 kW power that corresponds to the MCR in the diesel-mechanical solution. The specifications presented in Table 7.3 were used to calculate the necessary number of packs, nominal capacity, weight, and volume for each solution concerning energy and power demand.

In Table 8.3, the results from calculating the battery dimensions based on energy demand are presented. It can be observed that the Dolphin Energy ESS is lighter and less voluminous than the Dolphin Power ESS. However, the Dolphin Energy ESS does not satisfy the power demand when the dimensions are calculated from the energy demand.

A calculation based on the power demand was performed as well, and the results are presented in Table 8.4. Here, it is observed that the Dolphin Power ESS requires significantly fewer packs to satisfy the power demand. This, however, is not a solution for BE-operation as the energy demand is not satisfied. The Dolphin Energy ESS satisfies both limiting factors when the calculations are based on power demand. In Figure 8.7 the SOC of the two feasible solutions are plotted with respect to the load profile.

Table 8.3: Battery systems satisfying energy demand

	Corvus Dolphin Power	**Corvus Dolphin Energy**
M	39	28
Q$_{nom}$ (total) [kWh]	2129.40	2156.00
Max power [kW]	4684.68	1078.00
Total weight [kg]	17004.00	12208.00
Total volume (h x w x d) [mm^3]	2380 x 25545 x 500	2380 x 18340 x 500

Table 8.4: Battery systems satisfying power demand

	Corvus Dolphin Power	**Corvus Dolphin Energy**
Max power [kW]	2192.00	2192.00
$\mathbf{Q}_{nom}$ (total) [kWh]	996.36	4384.00
M	19	57
Total weight [kg]	8284.00	24852.00
Total volume (h x w x d) [mm^3]	2380 x 12445 x 500	2380 x 37335 x 500

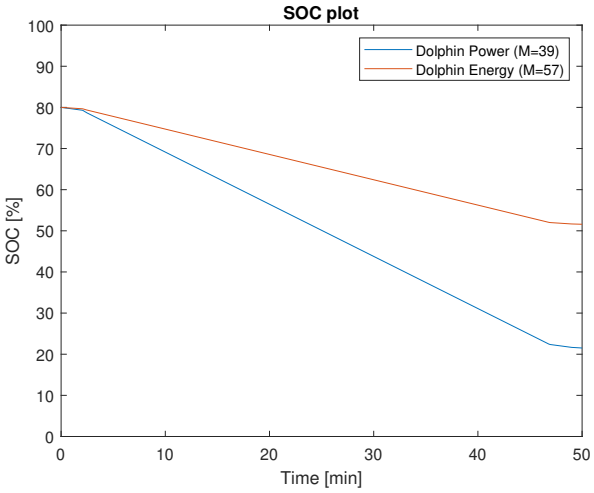

Figure 8.7: SOC-plot of the feasible BESS configurations for single-stage load profile

Compared to the baseline diesel-mechanical power plant, considering the weight of the diesel engines, gearboxes, auxiliary gensets, and the fuel tank, the Dolphin Power configuration results in a weight increase of 44% when neglecting the weight of the power converting components and the electric motor. Further, the volume of the battery solution is 74% larger than the volume of the diesel-mechanical system.

Power Transmission Concerning Component Losses

Including the losses, the minimum nominal capacity is 2369.40 kWh, and the battery should be able to deliver 2318.10 kW. Table 8.5 and Table 8.6 presents the results from calculations related to energy and power demand when losses are included.

Table 8.5: Battery systems satisfying energy demand concerning losses

	Corvus Dolphin Power	**Corvus Dolphin Energy**
M	44	31
$\mathbf{Q}_{nom}$ (total) [kWh]	2402.40	2387.00
Max power [kW]	5285.28	1193.50
Total weight [kg]	19184.00	13516.00
Total volume (h x w x d) [mm^3]	2380 x 28820 x 500	2380 x 20305 x 500

Table 8.6: Battery systems satisfying power demand concerning losses

	Corvus Dolphin Power	**Corvus Dolphin Energy**
$\mathbf{Q}_{nom}$ (total) [kWh]	1053.68	4636.21
M	20	61
Total weight [kg]	8720.00	26596.00
Total volume (h x w x d) [mm^3]	2380 x 13100 x 500	2380 x 39955 x 500

Since the losses included in this case are constant, the results correspond to the lossless case. The main difference is that the energy and power demand is higher, which results in a need for more battery packs. As illustrated in Figure 8.8, the battery's SOC-response concerning losses has the same shape as the response in the lossless configuration. However, when looking closely it can be observed that they are not exactly similar.

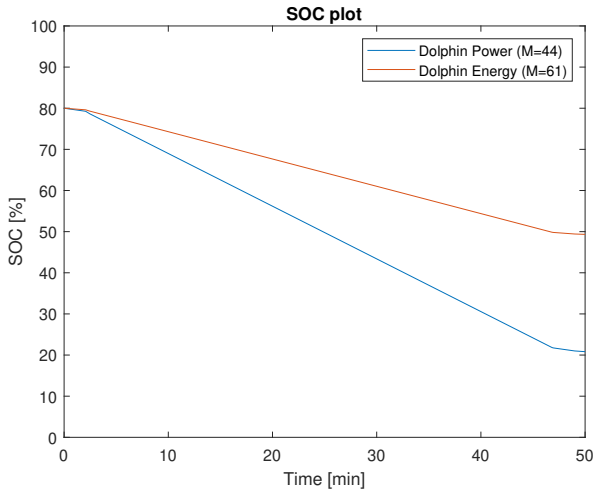

Figure 8.8: SOC-plot of the feasible BESS configurations for single-stage load profile concerning losses

Here, the Dolphin Power configuration result is a 12.8% weight and volume increase compared to the lossless solution. Compared to the DM solution this results in a 64% increase in weight and a 97% increase in volume.

8.3.2 Multi-Stage Load Profile

The results presented in this subsection define the battery dimensions needed to satisfy the most demanding multi-stage route of the vessel, presented in section 7.2.

Lossless Power Transmission

The energy demand of the multi-stage load profile is calculated similarly to the single-stage load profile. The increase in SOC during charging is dependent on the BESS's C-rate, which yields a different energy capacity demand depending on the BESS's specifications. Hence, the minimum energy capacity for the Dolphin Power ESS and Dolphin Energy ESS are 3511.20 and 4564.60 kWh, respectively. The power demand is based on the same assumptions as for the single-stage case, and the batteries should deliver 2192 kW power. Table 8.7 presents the results from calculations related to energy demand. It can be observed that both configurations satisfy the energy and power limits.

Table 8.7: Battery systems satisfying energy demand

	Corvus Dolphin Power	**Corvus Dolphin Energy**
$\mathbf{Q}_{nom,min}$ [kWh]	3511.20	4564.60
M	65	60
$\mathbf{Q}_{nom}$ (total) [kWh]	3549.00	4620.00
Max power [kW]	7807.80	2310.00
Total weight [kg]	28340.00	26160.00
Total volume (h x w x d) [mm^3]	2380 x 42575 x 500	2380 x 39300 x 500

Since the power demand is equal as in the single-stage case, the calculations based on power demand can be found in Table 8.4. This shows that the dimensioning based on power demand does not satisfy the energy demand for the multi-stage load profile. In Figure 8.9 the SOC of the two feasible solutions are plotted with respect to the load profile.

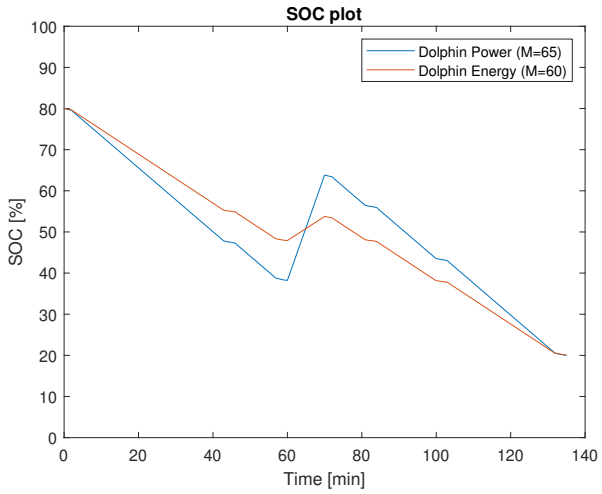

Figure 8.9: SOC-plot of the feasible BESS configurations for multi-stage load profile

Compared to the baseline diesel-mechanical power plant, considering the weight of the diesel engines, gearboxes, auxiliary gensets, and the fuel tank, the Dolphin Energy configuration results in a weight increase of 121% when neglecting the weight of the power converting components and the electric motor. The volume is increased by 168% from the conventional solution.

Power Transmission Concerning Component Losses

Including component losses, the minimum energy capacity for the Dolphin Power ESS and Dolphin Energy ESS are 3967.50 and 5114.70 kWh, respectively. The power demand is based on the same assumptions as for the single-stage case concerning losses, and the batteries should deliver 2318.10 kW power. Table 8.8 presents the results from calculations related to energy demand when losses are included.

The power demand is equal as in the single-stage case including losses, and it can be seen from Table 8.6 that the resulting dimensions do not satisfy the energy demand for the multi-stage load profile concerning losses. As in the single-stage case concerning losses, the losses included are constant, and the difference from the lossless case is that the energy and power demand is higher, which results in a need for more battery packs. Since the battery's SOC-response concerning losses is close to the response in the lossless configuration, the result plot is not presented here.

Table 8.8: Battery systems satisfying energy demand concerning losses

	Corvus Dolphin Power	**Corvus Dolphin Energy**
M	73	67
$\mathbf{Q}_{nom}$ (total) [kWh]	3985.80	5159.00
Max power [kW]	8768.80	2579.50
Total weight [kg]	31828.00	29212.00
Total volume (h x w x d) [mm^3]	2380 x 47815 x 500	2380 x 43885 x 500

Here, the lightest solution, the Dolphin Energy configuration, results in a 12% weight and volume increase compared to the lossless solution. This corresponds to a 148% weight increase, and a 199% volume increase, compared to the DM solution.

8.4 Optimization Over a Horizon Concerning DE, HE, and ZEHE Power Systems

Both the SFOC- and FOC-optimization over a horizon was run for the DE, HE, and ZEHE configurations. The optimization was run for the SFOC-curve concerning a fixed-speed configuration, due to the simpler characteristics compared to the three-staged SFOC-curves. The load profile concerned in the optimization is the single-stage profile with a sample period of 2 minutes, and all optimizations conducted have a horizon considering the whole load profile.

8.4.1 Diesel-Electric

First, the optimizations were run for the diesel-electric power system.

SFOC-Optimization

Figure 8.10 shows the result from the SFOC-optimization. It can be observed that in the transit operation the optimal states of the switches frequently, and diverges from the equal loadsharing which would yield the optimal specific fuel consumption. The total fuel consumption from the SFOC-optimization is 273.67 kg.

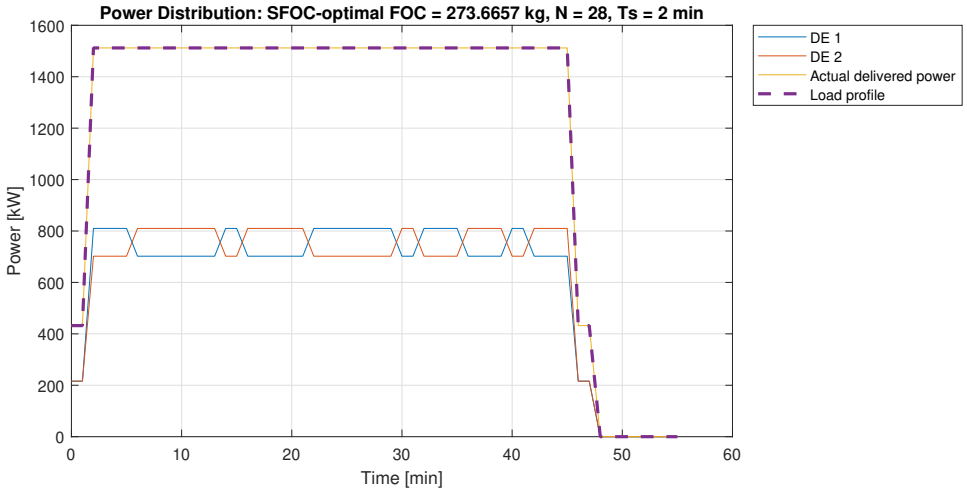

Figure 8.10: Diesel-electric SFOC-optimization over a horizon

FOC-Optimization

Figure 8.11 shows the result from the FOC-optimization. From the plot, it is observed that the solution shares the load equally in the transit phase, as expected when optimizing with respect to FOC and the load is sufficiently high. However, the loadsharing at a low load is not optimal, considering the characteristics of the SFOC-curve. The fuel consumption from the FOC-optimization is 272.10 kg. Comparing the two optimizations, it can be seen that the FOC-solution yields a better fuel consumption than the SFOC-optimized solution.

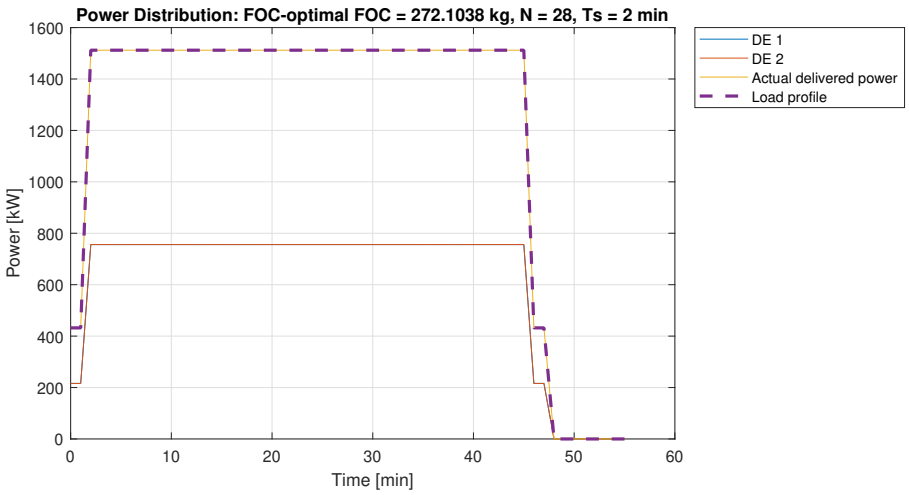

Figure 8.11: Diesel-electric FOC-optimization over a horizon

8.4.2 Hybrid-Electric

By including the battery in the optimization codes, the results of optimizing the loadsharing in the hybrid-electric power system were obtained.

SFOC-Optimization

Figure 8.12 shows the resulting power distribution and the corresponding fuel consumption from the hybrid-electric SFOC-optimization.

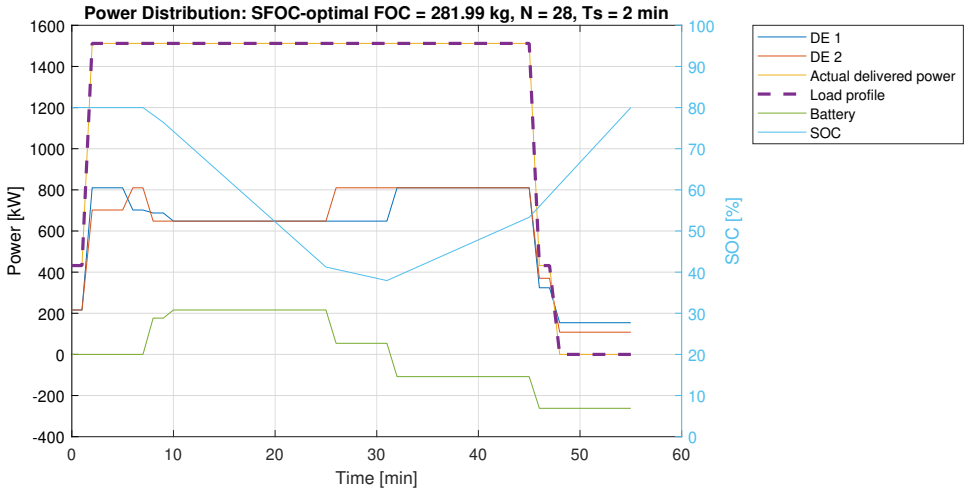

Figure 8.12: Hybrid-electric SFOC-optimization over a horizon

The power distribution shows that the battery is used only in parts of the transit phase, and that the battery is charged in the no-load phase. The resulting fuel consumption from the hybrid-electric SFOC-optimization is 281.99 kg, which is significantly increased from the diesel-electric optimizations.

FOC-Optimization

Figure 8.13 shows the resulting power distribution and the corresponding fuel consumption from the hybrid-electric FOC-optimization. From the plot, it is observed that the solution shares the load equally in the transit phase, as expected when optimizing with respect to FOC and the load is sufficiently high. The fuel consumption from the FOC-optimization is 270.53 kg. Comparing the previous optimizations, it can be seen that the hybrid-electric FOC-solution yields the best fuel consumption.

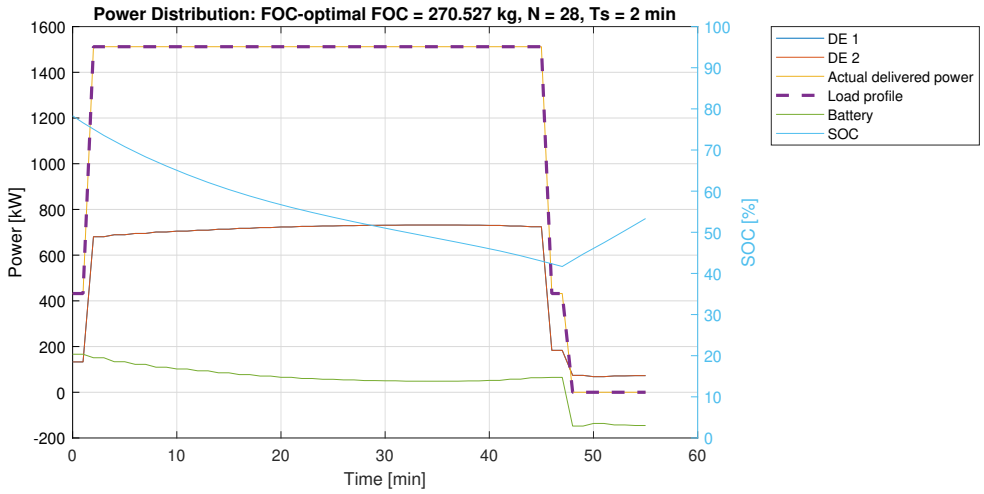

Figure 8.13: Hybrid-electric FOC-optimization over a horizon

8.4.3 Zero-Emission Hybrid-Electric

In the zero-emission HE power plant, the diesel engines from the previous cases are replaced by the PEM fuel cell system.

SFOC-Optimization

Figure 8.14 shows the resulting power distribution and the corresponding hydrogen consumption from the hybrid-electric SFOC-optimization. It is observed that the battery is quite evenly discharged in the transit phase from $\text{SOC}_{max}$to SOC_{min} and correspondingly the fuel cell delivers a quite even load. In the no-load phase, the battery is charged at a maximum C-rate. This results in a hydrogen consumption of 66.39 kg.

FOC-Optimization

Figure 8.15 shows the resulting power distribution and the corresponding hydrogen consumption from the hybrid-electric FOC-optimization. In the result plot, the fuel cell utilization tends to fluctuate. However, the battery utilization seems to have the same trend as in the SFOC-optimization, and the battery is fully discharged in the transit phase. Compared to the zero-emission SFOC-optimization, the hydrogen consumption is reduced in the FOC-optimization, with a hydrogen consumption of 64.54 kg.

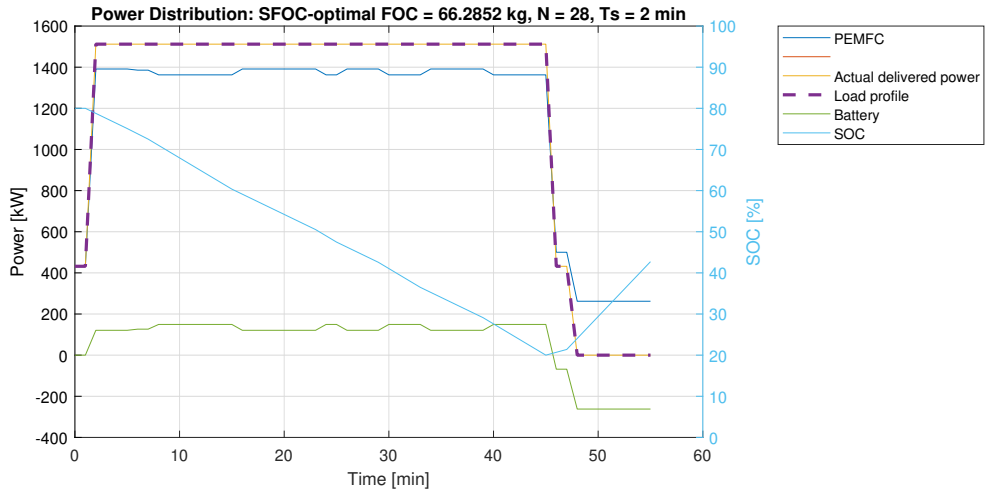

Figure 8.14: Zero-emission diesel-electric SFOC-optimization over a horizon

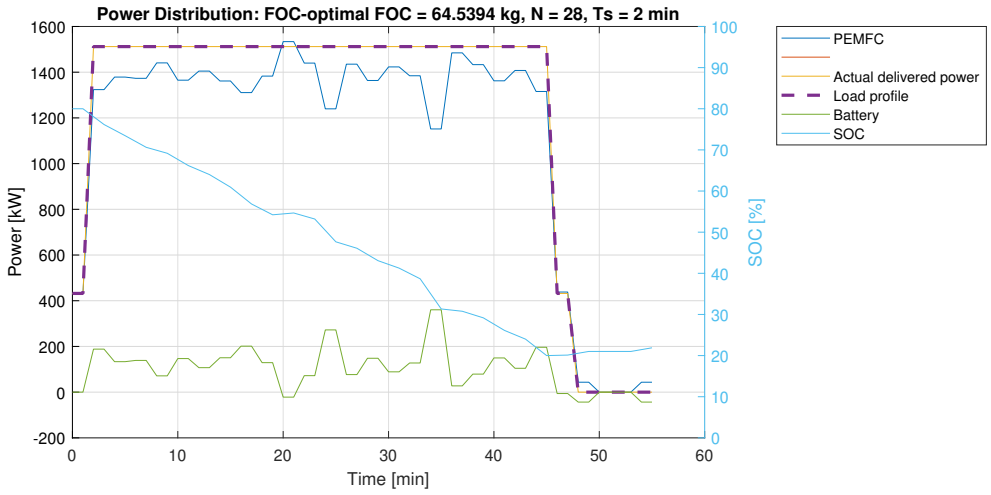

Figure 8.15: Zero-emission hybrid-electric FOC-optimization over a horizon

8.4.4 Total Fuel Consumption

Table 8.9 collects the results from all optimizations over the 56 minutes long load profile.

Table 8.9: Resulting fuel consumption from optimization over a horizon with SFOC-curve for fixed-speed configuration

	SFOC-optimization	**FOC-optimization**
Diesel-electric	273.67 kg	272.10 kg
Hybrid-electric	281.99 kg	270.53 kg
Zero-emission hybrid-electric	66.29 kg	64.54 kg

From the table it can be seen that the FOC-optimization outperforms the SFOC-optimization concerning fuel consumption for all three cases. The best diesel consumption is obtained for the hybrid-electric configuration, while the hydrogen consumed by the zero-emission power plant is significantly lower concerning fuel weight.

8.5 Weight and Volume of the Power Systems

In Table 8.10 the weight and volume of the power systems, and the percent-wise changes with respect to the diesel-mechanical power system are presented.

Table 8.10: Weight and Volume of the Power Systems

	Weight [kg]	**%-change**	**Volume** [m^3]	**%-change**
DM	11748		18.02	
DE	10720	- 8.75	16.9	- 6.39
BE	29212	148.00	52.2	199
HE	12028	2.38	19.2	6.58
ZEHE	9253	-21.23	22.0	22.27

In the zero-emission hybrid-electric configuration, 70 kg of gaseous hydrogen is considered, rounding up the results from the optimization over a horizon. This is included as the fuel tank weight and volume.

Chapter 9

Analysis and Discussion

In this chapter, the results from the previous chapters are analyzed and discussed.

9.1 Solver Selection

Concerning the GA solver in Matlab, *ga*, issues occurred when the load demand was significantly high. This could be due to the reduced number of feasible solutions as the load moves towards the extreme values. Then, if the initial population is too small or not spread enough, the optimization will not find a feasible solution. In the optimization, the genetic algorithms exploited the use of slack variables, despite the penalty in the fitness function. The algorithm also requires a lot more computation time which is unsatisfactory considering large optimization problems.

Even though the interior-point solver outperformed the genetic algorithm, it also has its weaknesses. The major challenge of the interior-point solver in Matlab, *fmincon*, is the local minima in the nonlinear functions, where the solver may find a solution satisfying all constraints within the solver options. The solver options, such as the step size and constraint violence tolerance, could be modified. Applying this mostly resulted in a slower solver and similar, or even worsened results. The need to fine-tune the solver was not considered the main task of the thesis, and the default solver was used only increasing the limits on number of iterations and function evaluations.

9.2 Conversion to Diesel-Electric High-Speed Passenger Ferries

In the instantaneous, lossless FOC-optimization considering the variable speed optimization, the load-sharing in the low-load and acceleration phase did not yield an optimal solution. If the result at a specific instance of maneuvering-load is compared with the fuel consumption if one engine delivers the whole power demand at the same turbocharging status, it can be shown that the optimal fuel consumption is obtained when one genset handles the whole load. Hence, the optimization did not return the globally optimal fuel consumption. It should also be noted that one limitation of the optimization algorithm implemented with these three curves was that the optimization could not choose to operate the engines in two different turbocharging states. Even though all these factors affected the result, and the global optimum was not reached, the fuel consumption was reduced compared to the DM power system.

When including the hotel loads, the fuel consumption became slightly higher than in the conventional solution. But in the conventional solution, the fuel consumption from the auxiliary engines serving the hotel loads was neglected. Therefore, it is assumed that the increased fuel consumption from the hotel

loads does not result in higher fuel consumption than the conventional system.

When the losses were included, the engines were not able to deliver the maximum load demand. Hence, bigger or extra engines must be installed in order to satisfy the load demand. These load conditions also yielded an increased fuel consumption, which confirms that it is not necessarily effective to put the diesel engines directly on a switchboard without changing any other design parameters. Even though this enables optimization of the loadsharing, the negative effects of having more components with losses did, in this case, deteriorate the fuel consumption. This motivates further exploration of different optimization strategies, which could yield a larger reduction in fuel consumption.

Since the three-stage performance diagram yielded a lot more complex optimization, this was not considered in the subsequent optimizations.

9.3 Analysis of Battery Dimensions

For the single-stage load profile, the Corvus Dolphin Energy solution was significantly heavier and more voluminous than the Corvus Dolphin Power solution. The energy demand is low due to the short duration, and fewer battery packs are needed. The sizing affects the battery's ability to deliver power, which depends on C-rate and the nominal energy. Hence, for the single-stage load profile, the battery with the highest C-rate yielded the best solution. From the SOC plots, it is observed that the Dolphin Energy solution has a much larger energy capacity than necessary for this load profile, with a SOC of over 50% at the end.

For the multi-stage load profile, the Corvus Dolphin Energy batteries yielded the best solution concerning weight and volume when the energy and power demand was satisfied. This implies that the energy demand is more extensive than the power demand for the multi-stage load profile. This is logical since the load profile extends over a longer time, yielding larger energy demands. With a large energy capacity, the required power can be achieved for lower C-rates. In the SOC plots, it can also be observed that the Dolphin Power configuration has larger fluctuations in SOC within the load period. This is an important factor when considering the SOH and lifetime of the battery. Recall that number of charge-discharge cycles affects the battery's state of health.

The main concern when considering the losses is the increased weight and volume due to larger energy and power demand. From all battery dimension calculations, the weight was significantly increased from the conventional power configuration. The solution needed to satisfy all voyages concerning losses was the Corvus Dolphin Energy ESS with 67 packs. This is critical for the weight- and volume-sensitive high-speed passenger ferries.

9.4 Performance of the Optimization Over a Horizon

In the optimization, the fixed-speed SFOC curve was applied due to the well-known characteristics of the curve. This made it easier to recognize if the optimizations yielded sensible results.

In the diesel-electric and hybrid-electric SFOC-optimization, it was observed that the loadsharing fluctuates. This is due to the piecewise linearity of the SFOC-curves. The power fluctuates between 648 and 810 kW, which is 60% and 75% of MCR, respectively. As shown in Appendix C, these loads are within the same sequence of the piecewise linear curve. The linear property yields the same SFOC-value when the load is shared unequally within the sequence as when it is shared equally. This yields two

different fuel consumptions, which the SFOC-optimization does not account for.

Concerning the diesel-electric FOC-optimization, the optimal loadsharing was obtained in the transit operation, yielding both minimum specific fuel consumption and fuel consumption. In the low-load conditions, the solution yields equal loadsharing as well. This differs from the theory associated with the SFOC-curve, where one of the engines should have handled the whole load. The initial state was set to equal loadsharing, which may be the cause of these results. This indicates that the optimization has found a local minimum at equal loadsharing. Since optimizing with a zero-vector as the initial state yielded a worse result, the initial state was kept at equal loadsharing.

In the hybrid-electric SFOC-optimization, it can also be observed that the battery is charged in the zero-load condition. This is because the SFOC-optimization strives to move the genset's power delivery towards the minimal SFOC at 82% of MCR. This results in a battery charging at maximum C-rate, and the engines share the load within the same piecewise linear SFOC-sequence. Due to the non-optimal battery utilization in the solution, the hybrid-electric SFOC-optimization yields a significantly higher fuel consumption compared to the diesel-electric solution.

Analyzing the hybrid-electric FOC-optimization, it is observed that also here, the load is shared equally in the low-load conditions, yielding a non-optimal result. In addition, the battery is charged in the no-load condition even though the battery does not need the energy for any subsequent loads. The optimization problem concerning a horizon of 28 load instances yields 168 optimization variables and a highly nonlinear problem. Thus, the optimization could find numerous solutions to the problem, and the interior-point optimization could be stuck in a local minimum. Despite the global optimum not being obtained, the nonlinear optimization including the battery yielded the lowest fuel consumption among the loadsharing optimizations involving a diesel engine.

Studying the results from the zero-emission hybrid-electric SFOC-optimization, it is observed that the battery is charged at no-load in a similar manner as for the hybrid-electric SFOC-optimization. In the transit phase, the solution shows an even utilization of the battery. The summarized specific hydrogen consumption is the lowest when the fuel cell is utilized evenly, ensuring that all battery capacity is utilized to drive the specific hydrogen consumption towards its minimum. Due to the higher specific energy of hydrogen, the weight of the fuel consumed is significantly reduced from the optimizations involving diesel engines.

In the zero-emission hybrid-electric FOC-optimization, the result is fluctuating in the transit phase. This is due to the high sampling frequency of the efficiency curve, resulting in a large dataset for the specific hydrogen consumption and many short sequences in the piecewise linear curve. This yields a lot more entries in the matrices generated in the piecewise linearization, which again leads to a larger number of constraints. The result is a lot more local minima in which the solver might get stuck. In spite of this, the battery utilization trend is the same as in the SFOC-optimization, and the battery is kept close to a C-rate of 0 in the no-load condition.

It is observed that the FOC-optimization outperforms the SFOC-optimization, with a KPI fuel consumption, in all power system optimizations. This correlates to the theory, which states that the optimal specific fuel consumption does not necessarily yield the optimal fuel consumption. For instance, will the SFOC-optimization drive the diesel engine away from no-load as this yields maximum specific fuel consumption, even though it yields a fuel consumption of zero.

Since the load during transit is 70% of MCR, it is reasonable to think that the optimal power distribution would be to use the batteries at maximum power during the low-load operations where the

specific fuel consumption is higher, and rather charge the battery during transit which would drive the engine operation closer to the minimum specific fuel consumption. Further, since the load profile in the optimization mainly consists of loads where equal loadsharing is preferred for the fixed-speed SFOC-curves, the optimization will yield a solution close to the equal loadsharing from the diesel-mechanical configuration. Thus, the main contribution to reduced fuel consumption in the hybrid-electric optimization would be due to the battery utilization more than the loadsharing among the gensets. However, the fixed-speed optimization is not further comparable to the DM solution due to the utilization of different SFOC-curves. Also, the losses must be included in the optimizations in order to have a realistic fuel consumption value.

9.5 Weight and Volume Considerations

In all power systems suggested, the weight and volume of the power converting devices were neglected. This is a very rough estimate. The weight should be included when considering the hydrodynamic effects due to the counteractive effect a weight increase has on the ship resistance, and followingly the power system. In addition to considering the weight when the resistance effects are considered, the volume of the components decreases the cargo/passenger-carrying capacity. This is an important factor to consider when working with emission-related problems in high-speed passenger ferries, as the emissions per passenger distance would increase if the passenger capacity is reduced.

From the rough estimates, the weight and volume of the diesel-electric power system are slightly reduced compared to the DM solution. Hence, it is reasonable to assume that there exist other diesel-electric configurations that stay within the same weight and volume range as the conventional system. Even when the weight of the power converting devices is included, and the losses are concerned.

Analyzing the results from calculating the battery-electric power system dimensions based on the multi-stage load profile, the selected configuration satisfies all single- and multi-stage voyages of the vessel. However, the weight and volume are increased tremendously compared to the baseline configuration, resulting in an infeasible solution. This encourages further evaluation of other batteries or hybrid battery configurations. The need for heavy and voluminous batteries to satisfy loads of a high-speed passenger ferry encourages investigation of the ship resistance as well. If the load demand is decreased, fewer batteries are needed. High-speed hydrofoil vessels may be one option to reduce the resistance.

Concerning the hybrid-electric power system, the battery packs contribute to a small increase in weight. This encourages studying the resistance effects as well, due to the small improvement in fuel consumption compared to the diesel-electric solution. There is no guarantee that the hybrid-electric solution presented in this thesis will result in an actual reduction in fuel consumption when all factors are included.

The zero-emission hybrid-electric solution yields a significant weight reduction. The fuel cell weight is an estimate from the manufacturer, and it is reasonable to assume that the realistic weight would be slightly higher. The weight includes auxiliary systems such as cooling systems and electrical panels. Taking all these factors into account, it is still reasonable to consider the power system a viable solution with respect to weight. However, the system is significantly more voluminous compared to the conventional power system, resulting in less space for passengers and thus higher fuel consumption per passenger distance. The focus of this thesis has not been ship design, and it might be possible to redesign the vessel to make this solution feasible. Also, other fuel cell-battery configurations might yield a better result.

Chapter 10

Conclusion

Concluding remarks and recommendations for further work follows.

10.1 Concluding remarks

In this thesis, the fields of zero-emission technologies and optimization of marine power plants have been explored. Ammonia engines, solid oxide fuel cells, and proton exchange membrane fuel cells have been proposed as alternative low- and zero-emission power sources, in addition to the more established battery energy storage technology. Furthermore, through various applications of these components in power systems, different optimization methods have been suggested for optimal loadsharing.

Concerning the different zero-emission technologies, the ammonia engine is a promising alternative. The aim for a multi-fuel solution yields flexibility which is important in the transition towards zero-emission shipping. However, the technologies concerning ammonia as fuel, both in internal combustion engines and solid-oxide fuel cells, are under development, and there are no concrete specifications available. The proton exchange membrane fuel cell technology is more mature, with commercial products available. Based on the availability of information and data specifications, the PEMFC was further investigated in the optimization problems.

Both instantaneous optimization and optimization over a horizon were considered methods for optimizing the loadsharing of different power configurations. Also, two different Matlab solvers were evaluated, both the interior-point solver, *fmincon*, and the genetic algorithm solver, *ga*. The interior-point optimization was selected for further optimization cases and applied in the optimizations over a horizon.

A case study was conducted concerning the high-speed passenger ferry Trondheimsfjord I. The baseline power configuration was compared to four alternative power plant configurations; diesel-electric, battery-electric, hybrid-electric, and zero-emission hybrid-electric. The key performance indicators were considering fuel consumption, weight and volume. The battery-electric dimensioning problem yielded a too large increase in weight and volume. The hybrid-electric power system showed promising results concerning FOC-optimization over a horizon, yielding the best performance among the power systems involving a diesel engine. The zero-emission hybrid-electric power system also showed good results concerning weight, but the low energy density is a major drawback concerning fuel tank volume. Some simplifications have been made, yielding uncertainties in the results. The component losses and the case-specific performance diagram should have been included. This would have enabled a complete comparison of the power system alternatives and the conventional power system. However, the optimization

strategies have shown the potential of fuel reduction through optimal loadsharing.

10.2 Recommendations for Further Work

Several suggestions of improvements were mentioned in the analysis and discussion. A summary of the main recommendations for further work include:

- The field of zero-emission technologies is in continuous development. Hence, further investigation encouraged, especially concerning the Wärtsilä ammonia engines that will undergo full-scale testing in September 2021.
- Including shoreside charging in the optimization code when the ship is at port, through implementing a decision variable for charging as a mixed-integer problem. Thus enabling optimization over a multi-stage load profile which accounts for charging at port.
- Considering an online optimization over a longer load profile, including receding horizon.
- Considering battery- and fuel cell-degradation effects when the components are utilized over longer horizons.
- Considering weight increase effects to thrust and propulsion relations, such that a weight increase of the power system changes the ship resistance and increases the power demand.
- Calculations of CO_2, NO_X, and SO_X emissions corresponding to the engine loads and fuel consumption.

Bibliography

Aarskog, F.G., Danebergs, J., 2020. Estimation of energy demand in the norwegian high-speed passenger ferry sector towards 2030. IFE ISBN: 978-82-7017-926-8.

ABB, 2018. ForSea (formerly HH Ferries Group) completes conversion of the world's largest battery ferries, powered by ABB. URL: https://new.abb.com/news/detail/10434/, Accessed: 09.11.2020.

ABB, 2020. ABB scales up fuel cells for shipping's greener future. URL: https://new.abb.com/news/detail/60295/abb-scales-up-fuel-cells-for-shippings-greener-future, Accessed: 28.10.2020.

ABB, 2020. ABB TechTalks: Hydrogen - fueling the change. URL: https://new.abb.com/marine/ABB-TechTalks/Hydrogen–Fueling-the-change, Accessed: 11.12.2020.

ABB, 2020. Fuel cell systems for ships. URL: https://new.abb.com/marine/systems-and-solutions/electric-solutions/fuel-cell, Accessed: 09.12.2020.

Allam, A., Catenaro, E., Onori, S., 2020. Pushing the envelope in battery estimation algorithms. iScience 23, 101847. doi: https://doi.org/10.1016/j.isci.2020.101847.

Allam, A., Onori, S., 2020. Online capacity estimation for lithium-ion battery cells via an electrochemical model-based adaptive interconnected observer. IEEE Transactions on Control Systems Technology , 1–16doi: 10.1109/TCST.2020.3017566.

Alnes, O., Eriksen, S., Vartdal, B., 2017. Battery-powered ships: A class society perspective. IEEE Electrification Magazine 5, 10–21. doi: 10.1109/MELE.2017.2718823.

Andrea, D., 2010. Battery Management Systems for Large Lithium-ion Battery Packs. Artech House.

Arena Ocean Hyway Cluster, 2020. Hydrogen infrastructure in the maritime industry. URL: https://www.oceanhywaycluster.no/projectlist/hyinfra, Accessed: 11.12.2020.

AtB, 2021. Rutetabeller for hurtigbåt og ferge. URL: https://www.atb.no/bat/, Accessed: 18.03.2021.

Ballard, 2020. Fuel cell solutions: Marine modules. URL: https://www.ballard.com/fuel-cell-solutions/fuel-cell-power-products/marine-modules, Accessed: 28.10.2020.

Bergen, A.R., Hill, D.J., 1981. A structure preserving model for power system stability analysis. IEEE Transactions on Power Apparatus and Systems PAS-100, 25–35. doi: 10.1109/TPAS.1981.316883.

Braga, M.H., Grundish, N.S., Murchison, A.J., Goodenough, J.B., 2017. Alternative strategy for a safe rechargeable battery. Energy Environ. Sci. 10, 331–336. doi: 10.1039/C6EE02888H.

Brødrene Aa, 2021. Trondheimsfjord i. URL: https://www.braa.no/fast-ferries/trondheimsfjord-i, Accessed: 17.03.2021.

Bø, T., Johansen, T., 2013. Scenario-based fault-tolerant model predictive control for diesel-electric marine power plant. OCEANS 2013 MTS/IEEE Bergen: The Challenges of the Northern Dimension , p.1–5, doi: 10.1109/OCEANS-Bergen.2013.6607989.

Bø, T.I., 2016. Scenario- and Optimization-Based Control of Marine Electric Power Systems. NTNU. Ph.D. Thesis. URL: https://ntnuopen.ntnu.no/ntnu-xmlui/handle/11250/2382342.

Bø, T.I., Dahl, A.R., Johansen, T.A., Mathiesen, E., Miyazaki, M.R., Pedersen, E., Skjetne, R., Sørensen, A.J., Thorat, L., Yum, K.K., 2015. Marine vessel and power plant system simulator. IEEE Access 3, 2065–2079.

Bø, T.I., Johansen, T.A., 2017. Battery power smoothing control in a marine electric power plant using nonlinear model predictive control. IEEE Transactions on Control Systems Technology 25, 1449–1456. doi: 10.1109/TCST.2016.2601301.

Corvus Energy, 2020a. Corvus dolphin energy. URL: https://corvusenergy.com/products/corvus-dolphin-energy/, Accessed: 11.11.2020.

Corvus Energy, 2020b. Corvus dolphin power. URL: https://corvusenergy.com/products/corvus-dolphin-power/, Accessed: 11.11.2020.

CPNETZEROSHIP, 2020. Containerized power: The flexible and fuel agnostic pathway to net zero shipping. (Proposal submitted to the European Commission 2020).

Dahl, A.R., Skjetne, R., Johansen, T., 2017. A structure preserving power system frequency model for dynamic positioning vessels. International Conference on Offshore Mechanics and Arctic Engineering doi: 10.1115/OMAE2017-61901.

Dahl, A.R., Thorat, L., Skjetne, R., 2018. Model predictive control of marine vessel power system by use of structure preserving model. IFAC-PapersOnLine 51, 335 – 340. doi: "https://doi.org/10.1016/j.ifacol.2018.09.501".

Deland, S., 2015. What is a genetic algorithm? URL: https://se.mathworks.com/videos/what-is-a-genetic-algorithm-100904.html, Accessed: 15.04.2021.

Dietrich, K., 2017. More than 800 fast ferries operate around the world with mtu power. URL: https://www.mtu-solutions.com/cn/en/stories/marine/commercial-vessels/more-than-800-fast-ferries-operate-around-the-world-with-mtu-power.html, Accessed: 23.03.2021.

DNV GL, 2015a. Dynamic positioning vessel design philosophy guidelines. URL: https://rules.dnvgl.com/docs/pdf/DNVGL/RP/2015-07/DNVGL-RP-E306.pdf, Accessed: 28.10.2020.

DNV GL, 2015b. In focus - the future is hybrid – a guide to use of batteries in shipping. URL: https://www.dnvgl.com/cn/publications/in-focus-the-future-is-hybrid-24771, Accessed: 09.11.2020.

DNV GL, 2018. Assessment of selected alternative fuels and technologies. URL: https://hydrogeneurope.eu/sites/default/files/2018-04/DNV_GL_Complete-Alt-Fuels_guidance_paper_2018-04_web.pdf, Accessed 11.12.2020.

DNV GL, 2020. Ammonia as a marine fuel. URL: https://www.dnvgl.com/publications/ammonia-as-a-marine-fuel-191385, Accessed: 23.02.2021.

Eidesvik, 2020. Viking energy with ammonia driven fuel cell. URL: https://eidesvik.no/viking-energy-with-ammonia-driven-fuel-cell/, Accessed: 28.10.2020.

Faltinsen, O.M., 2005. Hydrodynamics for High-Speed Marine Vehicles. Cambridge University Press.

Ferris, M., Mangasarian, O., Wright, S., 2007. Linear Programming with MATLAB. doi: https://doi.org/10.1137/1.9780898718775.

FLAGSHIPS, 2020. Ferry taking shape in turkey. URL: https://flagships.eu/2020/08/11/flagships-ferry-taking-shape-in-turkey/, Accessed: 28.10.2020.

Foss, B., Heirung, T.A.N., 2016. Merging Optimization and Control. isbn: 978-82-7842-201-4.

Ghimire, P., Park, D., Zadeh, M.K., Thorstensen, J., Pedersen, E., 2019. Shipboard electric power conversion: System architecture, applications, control, and challenges [technology leaders]. IEEE Electrification Magazine 7. doi: 10.1109/MELE.2019.2943948.

Godø, J.M.K., Vinje, J., 2019. Batteridrift på alle hurtigbåtruter i trøndelag. URL: https://www.miljodirektoratet.no/myndigheter/klimaarbeid/kutte-utslipp-av-klimagasser/klimasats/2017/utviklingskontrakt-for-hurtigbat#, Accessed: 12.02.2021.

Gulsvik, K.A., 2017. Battery management system for a lowcost rov. Department of Marine Technology, NTNU .

Gundersen, J.O.L.F.W.B., Hansen, J.F., 2014. Demonstrating the benefits of advanced power systems and energy storage for dp vessels.

Hill, D., Bergen, A., 1982. Stability analysis of multimachine power networks with linear frequency dependent loads. IEEE Transactions on Circuits and Systems 29, 840–848. doi: 10.1109/TCS.1982.1085110.

Hirscher, M., 2010. Handbook of Hydrogen. Wiley-VCH.

Hofstad, K., 2020. Hydrogendrivstoff. URL: https://snl.no/hydrogendrivstoff, Accessed: 11.12.2020.

Holland, J.H., 1975. Adaptation in Natural and Artificial Systems. University of Michigan Press, Ann Arbor, MI.

Igland, B.R., 2020. Prestudy on zero-emission hybrid-electric power systems in ships. (Project Thesis at NTNU, Department of Marine Technology).

IMO, 2020. Greenhouse gas emissions. URL: http://www.imo.org/en/OurWork/Environment/Pollution Prevention/AirPollution/Pages/GHG-Emissions.aspx, Accessed: 22.09.2020.

Karimi, S., Zadeh, M., Suul, J.A., 2020. Shore charging for plug-in battery-powered ships: Power system architecture, infrastructure, and control. IEEE Electrification Magazine 8, 47–61. doi: 10.1109/MELE.2020.3005699.

Kramer, O., 2017. Genetic Algorithm Essentials. Springer, Cham. doi: https://doi.org/10.1007/978-3-319-52156-5.

Li, K., Tseng, K., 2015. Energy efficiency of lithium-ion battery used as energy storage devices in micro-grid. IEEE doi: 10.1109/IECON.2015.7392923.

MAN Energy Solutions, 2020a. Introduction to future fuels. URL: https://www.man-es.com/marine/strategic-expertise/future-fuels?90d86291-9b31-456c-8af0-faaeba3a4edf%5B%5D=7, Accessed: 08.12.2020.

MAN Energy Solutions, 2020b. Man energy solutions to lead danish consortium developing ammonia-fuelled engine for maritime sector. URL: https://man-es.com/docs/default-source/press-releases-new/20201021_man_es_pr-aengine-mes_en.pdf, Accessed: 24.02.2021.

MAN Energy Solutions, 2020c. Two-stroke ammonia engine. URL: https://www.man-es.com/discover/two-stroke-ammonia-engine, Accessed: 09.12.2020.

Marine Traffic, 2021. Trondheimsfjord i. URL: https://www.marinetraffic.com/en/ais/details/ships/shipid:305955/mmsi:257304900/imo:9432177/vessel:TRONDHEIMSFJORD_I, Accessed: 17.03.2021.

Mayne, D., Rawlings, J., Rao, C., Scokaert, P., 2000. Constrained model predictive control: Stability and optimality. Automatica 36, 789–814. doi: 10.1016/S0005-1098(99)00214-9.

Miljødirektoratet, 2019. Utviklingskontrakt for hurtigbåt. URL: https://www.miljodirektoratet.no/myndigheter/klimaarbeid/kutte-utslipp-av-klimagasser/klimasats/2017/utviklingskontrakt-for-hurtigbat#, Accessed: 12.02.2021.

Miyazaki, M., 2017. Modeling and Control of Hybrid Marine Power Plants. NTNU. Ph.D. Thesis. URL: https://ntnuopen.ntnu.no/ntnu-xmlui/handle/11250/2450905.

Moghadam, F.K., Nejad, A.R., 2020. Evaluation of pmsg-based drivetrain technologies for 10-mw floating offshore wind turbines: Pros and cons in a life cycle perspective. Wind Energy 23, 1542–1563. URL: https://onlinelibrary.wiley.com/doi/abs/10.1002/we.2499.

MTU, 2006. Performance Diagram MTU 12V 2000 M72.

MTU, 2019. Diesel Engines 12V/16V 2000 M72. URL: https://www.mtu-solutions.com/content/dam/mtu/products/defense/marine-and-offshore-service-and-supply/main-propulsion/mtu-series-2000/3232231_Marine_spec_12V16V2000M72_1B.pdf/_jcr_content/renditions/original./3232231_Marine_spec_12V16V2000M72_1B.pdf, Accessed: 23.03.2021.

Mutarraf, M.U., Terriche, Y., Niazi, K.A.K., Vasquez, J.C., Guerrero, J., 2018. Energy Storage Systems for Shipboard Microgrids—A Review. Energies 11. doi: 10.3390/en11123492.

Nocedal, J., Wright, S.J., 2006. Numerical optimization. Springer Science+Business Media. ISBN-10: 0-387-30303-0.

Nordic Innovation, 2020. Zero emission energy distribution at sea. URL: https://www.nordicinnovation.org/programs/zero-emission-energy-distribution-sea-zeeds, Accessed 05.12.2020.

Norled, 2020. Product sheet MF Ampere. URL: https://www.norled.no/contentassets/774b856cd8934499a8dbc94b21361878/produktark—mf-ampere.pdf, Accessed: 09.11.2020.

Othman, M.B., Reddy, N.P., Ghimire, P., Zadeh, M.K., Anvari-Moghaddam, A., Guerrero, J.M., 2019. A hybrid power system laboratory: Testing electric and hybrid propulsion. IEEE Electrification Magazine 7, 89–97. Doi: 10.1109/MELE.2019.2943982.

Prototech, 2020. Fuel cell power systems. URL: https://www.prototech.no/applications/power-systems-fuel-cells/, Accessed: 28.10.2020.

Rawlings, J.B., Mayne, D., Diehl, M.M., 2019. Model Predictive Control: Theory, Computation, and Design. Nob Hill Publishing, LLC.

Reddy, N.P., Zadeh, M.K., Thieme, C.A., Skjetne, R., Sorensen, A.J., Aanondsen, S.A., Breivik, M., Eide, E., 2019. Zero-emission autonomous ferries for urban water transport: Cheaper, cleaner alternative to bridges and manned vessels. IEEE Electrification Magazine 7, 32–45.

Rolls-Royce, 2016. Prodct guide bergen engine type b32:40p. URL: https://www.rolls-royce.com/ /media/Files/R/Rolls-Royce/documents/marine-product-finder/Project%20Guide%20B32_40P.pdf, Accessed: 09.04.2021.

Sivanandam, S.N., Deepa, S.N., 2008. Introduction to Genetic Algorithms. Springer, Berlin, Heidelberg. doi: https://doi.org/10.1007/978-3-540-73190-0.

Skjetne, R., 2017. Technical Note: Genset Optimization Model. NTNU .

Skjetne, R., 2021. Technical Note: Hybrid Electric Ship: Fuel optimization. NTNU .

Skjong, E., Johansen, T.A., Molinas, M., Sørensen, A.J., 2017. Approaches to economic energy management in diesel–electric marine vessels. IEEE Transactions on Transportation Electrification 3, 22–35.

Sorensen, A.J., Skjetne, R., Bo, T., Miyazaki, M.R., Johansen, T.A., Utne, I.B., Pedersen, E., 2017. Toward safer, smarter, and greener ships: Using hybrid marine power plants. IEEE Electrification Magazine 5, 68–73.

Stone, P., Opila, D.F., Park, H., Sun, J., Pekarek, S., DeCarlo, R., Westervelt, E., Brooks, J., Seenumani, G., 2015. Shipboard power management using constrained nonlinear model predictive control. IEEE Electric Ship Technologies Symposium (ESTS) , p.1–7, doi: 10.1109/ESTS.2015.7157853.

Thorat, L., Skjetne, R., 2018. Optimal online configuration and load-sharing in a redundant electric power system for an offshore vessel using mixed integer linear programming. International Conference on Offshore Mechanics and Arctic Engineering doi: 10.1115/OMAE2018-77955.

Tvete, H.A., Hill, D., 2021. Are solid-state batteries the holy grail for 2030? URL: https://www.dnvgl.com/to2030/technology/are-solid-state-batteries-the-holy-grail-for-2030.html, Accessed: 18.02.2021.

Ulstein, 2019. Color Hybrid. URL: https://ulstein.com/color-hybrid, Accessed 09.11.2020.

UNFCCC, 2020. What is the paris agreement? URL: https://cop23.unfccc.int/process-and-meetings/the-paris-agreement/what-is-the-paris-agreement, Accessed: 22.09.2020.

van Biert, L., Godjevac, M., Visser, K., Aravind, P., 2016. A review of fuel cell systems for maritime applications. Journal of Power Sources 327, 345 – 364. doi: "https://doi.org/10.1016/j.jpowsour.2016.07.007".

Vu, T.V., Gonsoulin, D., Diaz, F., Edrington, C.S., El-Mezyani, T., 2017. Predictive control for energy management in ship power systems under high-power ramp rate loads. IEEE Transactions on Energy Conversion 32, 788–797. doi: 10.1109/TEC.2017.2692058.

Wenzl, H., 2009. Batteries and Fuel Cells — Efficiency. Elsevier, Amsterdam. URL: https://www.sciencedirect.com/science/article/pii/B9780444527455000472.

Wilhelmsen, 2019. New design makes liquefied hydrogen bunker vessels a reality. URL: https://www.wilhelmsen.com/media-news-and-events/press-releases/2019/new-design-makes-liquefied-hydrogen-bunker-vessels-a-reality/, Accessed: 11.12.2020.

Wu, Z., 2017. Comparison of fuel consumption on a hybrid marine power plant with low-power versus high-power engines. Department of Marine Technology, NTNU .

Wu, Z., Thorat, L., Skjetne, R., 2018. Comparison of fuel consumption on a hybrid marine power plant with low-power versus high-power engines. International Conference on Offshore Mechanics and Arctic Engineering doi: https://doi.org/10.1115/OMAE2018-77959.

Wärtsilä, 2020a. A clean marine future on the horizon. URL: https://www.wartsila.com/norshipping/press/horizon, Accessed: 19.11.2020.

Wärtsilä, 2020b. Wireless Charging. URL: https://www.wartsila.com/marine/build/powersystems/shore-connections/wireless-charging, Accessed: 08.12.2020.

Wärtsilä, 2020c. Wärtsilä 34df. URL: https://www.wartsila.com/marine/build/engines-and-generatingsets/dual-fuel-engines/wartsila-34df, Accessed: 30.10.2020.

Wärtsilä, 2020d. Wärtsilä advances future fuel capabilities with first ammonia tests. URL: https://www.wartsila.com/media/news/25-03-2020-wartsila-advances-future-fuel-capabilities-with-first-ammonia-tests-2670619?utm_source=press-release&utm_medium=org&utm_term=marine&utm_content=1st+Ammonia+test&utm_campaign=Green+Ammonia+engine+tests, Accessed: 09.12.2020.

Xing, H., Stuart, C., Spence, S., Chen, H., 2021. Fuel cell power systems for maritime applications: Progress and perspectives. Sustainability 13. doi: 10.3390/su13031213.

Yara, 2021. Åpner for historisk satsing på grønt hydrogen og grønn ammoniakk i norge. URL: https://www.yara.com/corporate-releases/apner-for-historisk-satsing-pa-gront-hydrogen-og-gronn-ammoniakk-i-norge/, Accessed: 25.02.2021.

Yara Norge, 2020. Produktansvarlighet: En pålitelig partner innen sikkerhet. URL: https://www.yara.no/kjemiske-og-miljomessige-losninger/prosesskjemikalier/ammoniakk/, Accessed 01.11.2020.

Yue, M., Jemei, S., Gouriveau, R., Zerhouni, N., 2019. Review on health-conscious energy management strategies for fuel cell hybrid electric vehicles: Degradation models and strategies. International Journal of Hydrogen Energy 44, 6844–6861. doi: https://doi.org/10.1016/j.ijhydene.2019.01.190.

Zadeh, M., 2020a. Compendium TMR4335 Hybrid Electric Propulsion. NTNU.

Zadeh, M., 2020b. Lectures TMR4290. NTNU.

Zahedi, B., Norum, L.E., Ludvigsen, K.B., 2014. Optimized efficiency of all-electric ships by dc hybrid power systems. Journal of Power Sources 255, 341–354. doi: https://doi.org/10.1016/j.jpowsour.2014.01.031.

ZEVS, 2021. Enabling Zero Emission Passenger Vessel Services.

Appendix

A Example of Hybrid-Electric Power System Model

A.1 Instantaneous optimization

To exemplify the optimization structure concerning the SFOC optimization, three gensets with different datasets are considered. The example parameters are $M = 3$, $m_1 = 3$, $m_2 = 4$ and $m_3 = 2$. The gensets are in a hybrid configuration with a battery. The state vector is given as:

$$x = \begin{bmatrix} p_1 & p_2 & p_3 & \mu_1 & \mu_2 & \mu_3 & C\_rate \end{bmatrix}^T$$

The optimization problem is expressed as:

$$\begin{aligned}
&\min \quad c_1 \cdot x(4) + c_2 \cdot x(5) + c_3 \cdot x(6) \\
&\text{s.t.} \\
&\begin{bmatrix}
a_{11} & 0 & 0 & -1 & 0 & 0 & 0 & \\
a_{12} & 0 & 0 & -1 & 0 & 0 & 0 & \\
a_{13} & 0 & 0 & -1 & 0 & 0 & 0 & \\
0 & a_{21} & 0 & 0 & -1 & 0 & 0 & \\
0 & a_{22} & 0 & 0 & -1 & 0 & 0 & \\
0 & a_{23} & 0 & 0 & -1 & 0 & 0 & \\
0 & a_{24} & 0 & 0 & -1 & 0 & 0 & \\
0 & 0 & a_{31} & 0 & 0 & -1 & 0 & \\
0 & 0 & a_{32} & 0 & 0 & -1 & 0 & \\
1 & 0 & 0 & 0 & 0 & 0 & 0 & 0 \\
0 & 1 & 0 & 0 & 0 & 0 & 0 & 0 \\
0 & 0 & 1 & 0 & 0 & 0 & 0 & 0 \\
0 & 0 & 0 & 0 & 0 & 0 & 0 & 1 \\
0 & 0 & 0 & 0 & 0 & 0 & 0 & -1
\end{bmatrix} x \leq \begin{bmatrix}
-b_{11} \\ -b_{12} \\ -b_{13} \\ -b_{21} \\ -b_{22} \\ -b_{23} \\ -b_{24} \\ -b_{31} \\ -b_{32} \\ \Delta p_1 - x_0(1) \\ \Delta p_2 - x_0(2) \\ \Delta p_3 - x_0(3) \\ (SOC_0 - SOC_{min})/\Delta t \\ (SOC_{max} - SOC_0)/\Delta t
\end{bmatrix}, \\
&\begin{bmatrix} c_1 P_{b,1} & c_2 P_{b,2} & c_3 P_{b,3} & 0 & 0 & 0 & Q_{nom} \end{bmatrix} x = P_{load}, \\
&\begin{bmatrix} c_1 p_{1,min} & c_2 p_{2,min} & c_3 p_{3,min} & 0 & 0 & 0 & C_rate_{min} \end{bmatrix} \leq x \leq \\
&\begin{bmatrix} c_1 p_{1,max} & c_2 p_{2,max} & c_3 p_{3,max} & \infty & \infty & \infty & C_rate_{max} \end{bmatrix}.
\end{aligned}$$

A.2 Example of Optimization Over a Horizon

To exemplify the optimization structure over a horizon, the SFOC optimization with a gensets and a battery is considered. The example parameters are $N = 3$, $M = 1$, and $m_1 = 2$. The state vector is given as:

$$x = \begin{bmatrix} p_{1,1} & p_{2,1} & p_{3,1} & \mu_{1,1} & \mu_{2,1} & \mu_{3,1} & C\_rate_1 & C\_rate_2 & C\_rate_3 \end{bmatrix}^T$$

The optimization problem is expressed as:

$$\begin{aligned} \min \quad & c_1 \cdot x(4) + c_2 \cdot x(5) + c_3 \cdot x(6) \\ \text{s.t.} \quad & \begin{bmatrix} A_{ineq,SFC} \\ A_{ineq,Rate} \\ A_{ineq,SOC} \end{bmatrix} x \leq \begin{bmatrix} b_{ineq,SFC} \\ b_{ineq,Rate} \\ b_{ineq,SOC} \end{bmatrix} \\ & A_{eq} x = b_{eq} \\ & lb \leq x \leq ub, \end{aligned}$$

where

$$A_{ineq,SFC} = \begin{bmatrix} a_1 & 0 & 0 & -1 & 0 & 0 & 0 & 0 & 0 \\ 0 & a_1 & 0 & 0 & -1 & 0 & 0 & 0 & 0 \\ 0 & 0 & a_1 & 0 & 0 & -1 & 0 & 0 & 0 \\ a_2 & 0 & 0 & -1 & 0 & 0 & 0 & 0 & 0 \\ 0 & a_2 & 0 & 0 & -1 & 0 & 0 & 0 & 0 \\ 0 & 0 & a_2 & 0 & 0 & -1 & 0 & 0 & 0 \end{bmatrix}, b_{ineq,SFC} = \begin{bmatrix} -b_1 \\ -b_1 \\ -b_1 \\ -b_2 \\ -b_2 \\ -b_2 \end{bmatrix},$$

$$A_{ineq,Rate} = \begin{bmatrix} -1 & 0 & 0 & 0 & 0 & 0 & 0 & 0 & 0 \\ 1 & -1 & 0 & 0 & 0 & 0 & 0 & 0 & 0 \\ 0 & 1 & -1 & 0 & 0 & 0 & 0 & 0 & 0 \\ 1 & 0 & 0 & 0 & 0 & 0 & 0 & 0 & 0 \\ -1 & 1 & 0 & 0 & 0 & 0 & 0 & 0 & 0 \\ 0 & -1 & 1 & 0 & 0 & 0 & 0 & 0 & 0 \end{bmatrix}, b_{ineq,Rate} = \begin{bmatrix} \Delta p \Delta t_1 - p_0 \\ \Delta p \Delta t_2 \\ \Delta p \Delta t_3 \\ \Delta p \Delta t_1 + p_0 \\ \Delta p \Delta t_2 \\ \Delta p \Delta t_3 \end{bmatrix},$$

$$A_{ineq,SOC} = \begin{bmatrix} 0 & 0 & 0 & 0 & 0 & 0 & -\Delta t_1 & 0 & 0 \\ 0 & 0 & 0 & 0 & 0 & 0 & -\Delta t_1 & -\Delta t_2 & 0 \\ 0 & 0 & 0 & 0 & 0 & 0 & -\Delta t_1 & -\Delta t_2 & -\Delta t_3 \\ 0 & 0 & 0 & 0 & 0 & 0 & \Delta t_1 & 0 & 0 \\ 0 & 0 & 0 & 0 & 0 & 0 & \Delta t_1 & \Delta t_2 & 0 \\ 0 & 0 & 0 & 0 & 0 & 0 & \Delta t_1 & \Delta t_2 & \Delta t_3 \end{bmatrix}, b_{ineq,SOC} = \begin{bmatrix} SOC_{max} - SOC_0 \\ SOC_{max} - SOC_0 \\ SOC_{max} - SOC_0 \\ SOC_0 - SOC_{min} \\ SOC_0 - SOC_{min} \\ SOC_0 - SOC_{min} \end{bmatrix},$$

$$A_{eq} = \begin{bmatrix} P_b & 0 & 0 & 0 & 0 & 0 & Q_n om & 0 & 0 \\ 0 & P_b & 0 & 0 & 0 & 0 & 0 & Q_n om & 0 \\ 0 & 0 & P_b & 0 & 0 & 0 & 0 & 0 & Q_n om \end{bmatrix}, b_{eq} = \begin{bmatrix} P_{Load,1} \\ P_{Load,2} \\ P_{Load,3} \end{bmatrix},$$

$$lb = \begin{bmatrix} p_{min} \\ p_{min} \\ p_{min} \\ 0 \\ 0 \\ 0 \\ C\_rate_{min} \\ C\_rate_{min} \\ C\_rate_{min} \end{bmatrix}, ub = \begin{bmatrix} p_{max} \\ p_{max} \\ p_{max} \\ \infty \\ \infty \\ \infty \\ C\_rate_{max} \\ C\_rate_{max} \\ C\_rate_{max} \end{bmatrix}.$$

B Matlab Code

B.1 Hybrid-Electric Power System: FOC-Optimization Over a Horizon

This Matlab example concerns the nonlinear FOC optimization over a horizon, concerning a hybrid-electric power plant with two equal gensets and a battery. Note that by setting Crate_min and Crate_max to zero, a diesel-electric power system is obtained.

```
%% Data
clear all
tic
global M N C Pb A B E tau
M = 2;          % Number of gensets
c  = [1  1]';  % Connect vector
Pbbus = 0;

% Genset
Pb     = zeros(M,1);
Pb(1,1) = 1080;  % Unit: kW
Pb(2,1) = 1080;  % Unit: kW
Ramp_rate = [1;  1]/8;% Unit: %/s
Ramp_rate = Ramp_rate*3600; % Unit: %/h

%Battery system
Vnom = 805; % Unit: V
Qnom = 54.6*3; % Unit: kWh
Cnom = Qnom*1000/Vnom;

SOC0 = 0.8;
SOC0ref = SOC0;
SOCmin = 0.2;
SOCmax = 0.8;
Crate_min = -1.6; % Unit: [1/h]
Crate_max = 2.2; % Unit: [1/h]

Pbat = Crate_max*Qnom; % Unit: kW

Pbbus = sum(Pb)+Pbat; % Unit: kW

Ttot = 56; % Total time duration in minutes
Ts   = 2.0;  % Sample time in minutes
dt = Ts*ones(1,Ttot/Ts);
N = length(dt);
LoadProfile = zeros(1,N);
sum_dt = 0;
for j = 1:N
    sum_dt = sum_dt + dt(j);
    if sum_dt <= 2
        LoadProfile(j) = 0.2;
    elseif sum_dt <= 4
        LoadProfile(j) = 0.9;
```

```
    elseif sum_dt <= 46
        LoadProfile(j) = 0.7;
    elseif sum_dt <= 48
        LoadProfile(j) = 0.2;
    else
        LoadProfile(j) = 0.0;
    end
end
dt = dt/60;
LoadProfile = LoadProfile*2160;

%% PWL SFOC
dp = 0.01;
pp = 0:dp:1;
fsfoc = zeros(M,length(pp));

% PWL of SFOC
p = {}; z = {};
m = zeros(M+1,2);

%Fra eksempel
p0   = [  0   5  10  15  25  40  50  60  75  82  95 100]/100;
z1   = [380 340 310 290 260 230 215 205 194 190 200 215];

for j = 1:M
    p{j} = p0;
    z{j} = z1;
end

% Configuration of PWL curve coefficients and corresponding
   constraint matrices
aj = {}; bj = {};

for j=1:M
    m(j+1,1) = length(z{j})-1; %Number of SFOC-measurements for
       genset j, column 1
    m(j+1,2) = m(j,2) + m(j+1,1); %Number of SFOC-measurements summed
       , column 2
    for k=1:m(j+1,1)
        aj{j}(k,1) = (z{j}(k+1)-z{j}(k))/(p{j}(k+1)-p{j}(k));
        bj{j}(k,1) =  z{j}(k) - aj{j}(k)*p{j}(k);
    end
end

for i = 1:M
    for j = 1:length(pp)
        fsfoc(i,j) = max(aj{i}(:)*pp(j) + bj{i}(:)); %SFOC curve for
           each genset
        ffc(i,j) = fsfoc(i,j)*Pb(i)*pp(j); %FOC curve for each genset
    end
```

```
end

A = zeros(m(end,2),M);
B = zeros(m(end,2),M);
E = zeros(m(end,2),M);
b = zeros(m(end,2),1);
a = zeros(m(end,2),1);
pmin = zeros(M,1);
pmax = ones(M,1);

for j=1:M
    A(m(j,2)+1:m(j+1,2),j) = aj{j};
    B(m(j,2)+1:m(j+1,2),j) = bj{j};
    E(m(j,2)+1:m(j+1,2),j) = -ones(m(j+1),1);
    b(m(j,2)+1:m(j+1,2),1) = bj{j};
    a(m(j,2)+1:m(j+1,2),1) = aj{j};
end

%% Over a horizon
Nref = N;
xrh_opt = zeros(2*M+2,length(LoadProfile));
fnl_opt = zeros(1,length(LoadProfile));
logx = zeros(N*(2*M+2),N);

i = 1;
x0 = zeros(N*(2*M+2),1);
for j = 1:N
    x0(2*j-1)      = LoadProfile(j)/(c'*Pb);
    x0(2*j)        = x0(2*j-1);
    x0(M*N+2*j-1) = z1(end)*Pb(1)/1.2;
    x0(M*N+2*j)    = z1(end)*Pb(2)/1.2;
end

tau = zeros(1,N); %Ensures that tau and C has correct size when the
    horizon decreases
C = zeros(M*N,1);
tau(1:N) = dt(i:i+N-1);
C = kron(ones(N,1),c);

% Matrices used in SOC limit
T1 = zeros(N);
T2 = T1;
for j = 1:N
    for l = j:N
        T1(l,j) = -tau(j);
        T2(l,j) = tau(j);
    end
end

% Ramp-up limits
```

```
A_ramp = zeros(2*M*N,N*(2*M+2));
A_ramp(1:M*N,1:M*N) = kron(-eye(M),eye(N));
A_ramp(M*N+1:2*M*N,1:M*N) = kron(eye(M),eye(N));
b_ramp = zeros(2*M*N,1);
b_ramp(1:M,1) = Ramp_rate*tau(1)-x0(1:M);
b_ramp(N*M+1:(N+1)*M,1) = Ramp_rate*tau(1)+x0(1:M);
for k = 1:N-1
    A_ramp(k*M+1:(k+1)*M, (k-1)*M+1:k*M) = eye(M);
    A_ramp(M*N+k*M+1:M*N+(k+1)*M, (k-1)*M+1:k*M) = -eye(M);
    b_ramp(k*M+1:(k+1)*M) = Ramp_rate*tau(k+1);
    b_ramp(M*N+k*M+1:M*N+(k+1)*M) = Ramp_rate*tau(k+1);
end

% The SOC limits
A_SOC = zeros(2*N,N*(2*M+2));
A_SOC(1:N,2*M*N+1:(2*M+1)*N) = T1;
A_SOC(N+1:2*N,2*M*N+1:(2*M+1)*N) = T2;
b_SOC(1:2*N,1) = [kron(ones(N,1),SOCmax-SOC0);
                  kron(ones(N,1),SOC0-SOCmin)];

A_ineq = [A_ramp;
          A_SOC];

b_ineq = [b_ramp;
          b_SOC];

% Load balance
A_eq = zeros(N,N*(2*M+2));
A_eq(:,1:M*N) = kron(eye(N),Pb')*diag(C);
A_eq(:,2*M*N+1:(2*M+1)*N) = Qnom*eye(N);
A_eq(:,(2*M+1)*N+1:end) = eye(N);

b_eq = LoadProfile(i:i+N-1)';

% Upper and lower bounds
lb = [diag(C)*kron(ones(N,1),pmin); zeros(M*N,1); kron(ones(N,1),
    Crate_min); kron(ones(N,1),Crate_min*Qnom)];
ub = [diag(C)*kron(ones(N,1),pmax); z1(end)*Pb(1)*ones(M*N,1); kron(
    ones(N,1),Crate_max); kron(ones(N,1),Crate_max*Qnom)];

opt = optimoptions('fmincon','Display','off');
opt.MaxFunctionEvaluations = 1e6;
opt.MaxIterations = 1e6;
[xinl2,fval,exitflag,out] = fmincon(@rh_fun,x0,A_ineq,b_ineq,A_eq,
    b_eq,lb,ub,@mycon,opt);
if exitflag < 0.5
        xinl2 = [ones(M,1); zeros(1,1)];
        toc
        error(['Interior point: ', out.message]);
end
```

```
% logx: Matrix that logs the whole prediction for each iteration
for u = 1:length(xinl2)
    logx(u,i) = xinl2(u);
end

for j = 1:N
    % Resulting states applied and resulting fuel consumption
    xrh_opt(:,j) = [xinl2((j-1)*M+1:j*M); xinl2(M*N+(j-1)*M+1:M*N+j*M
        ); xinl2(2*M*N+j); xinl2((2*M+1)*N+j)];
    frh_opt(j) = ffc(1,floor(xrh_opt(1,j)*100)+1) + (ffc(1,ceil(
        xrh_opt(1,j)*100)+1)-ffc(floor(xrh_opt(1,j)*100)+1))*(xrh_opt
        (1,j)*100-floor(xrh_opt(1,j)*100))...
                + ffc(2,floor(xrh_opt(2,j)*100)+1) + (ffc(2,ceil(
                    xrh_opt(2,j)*100)+1)-ffc(floor(xrh_opt(2,j)*100)
                    +1))*(xrh_opt(2,j)*100-floor(xrh_opt(2,j)*100));
end

% For plotting each second over the whole time sequence
Load = zeros(1,sum(tau*60));
xen = zeros(size(xrh_opt,1),length(Load));
iter = 0;
for i = 1:N
    it = dt(i)*60;
    for j = 1:it
        iter = iter + 1;
        Load(iter) = LoadProfile(i);
        xen(:,iter) = xrh_opt(:,i);
        if iter == 1
            SOC(iter) = SOC0ref - xrh_opt(5,i)*1/60;
        else
            SOC(iter) = SOC(iter-1) - xrh_opt(5,i)*1/60;
        end
        fc(iter) = frh_opt(i);
    end
end

%% Results
disp(['Optimal fuel oil consumption optimizing wrt FOC with receding
    horizon = ',num2str(sum(fc)/60/1000), ' kg, N = ', num2str(Nref)])
    ;

%% Plots
timevec = 1:length(Load);

figure(129); clf;
plot(timevec, Pb(1)*xen(1,:))
hold on
plot(timevec, Pb(2)*xen(2,:))
plot(timevec, Pb(1)*xen(1,:)+Pb(2)*xen(2,:)+Qnom*xen(5,:));
plot(timevec, Load,'--','LineWidth',2)
```

```
229 plot(timevec, Qnom*xen(5,:))
230 ylabel('Power [kW]')
231
232 yyaxis right
233 plot(timevec, SOC*100)
234 ylim([0 100])
235 title('Power Distribution')
236 legend('DE 1','DE 2','Actual delivered power', 'Load profile', '
    Battery','SOC')
237 xlabel('Time [min]')
238 ylabel('SOC [%]')
239 grid on;
240 hold off;
241
242 toc
243
244 function f = rh_fun(x)
245 global M N C tau
246 f = C'*kron(diag(tau),eye(M))*x(M*N+1:2*M*N) + 3.6e2*norm(x(end-N+1:
    end),2);
247
248 end
249
250 function [c,ceq] = mycon(x)
251 global M N A Pb B E
252 c = kron(A,eye(N))*(x(1:M*N).*x(1:M*N).*kron(Pb,eye(N)))...
253     + kron(B,eye(N))*(x(1:M*N).*kron(Pb,eye(N))) + kron(E,eye(N))*x(M
        *N+1:2*M*N);
254 ceq = [];
255 end
```

C Specific Fuel Consumption Data

C.1 Lookup Tables from Performance Diagram

In the tables the x-axis is engine speed in RPM, y-axis is power in kW and the table elements are specific fuel consumption in g/kWh.

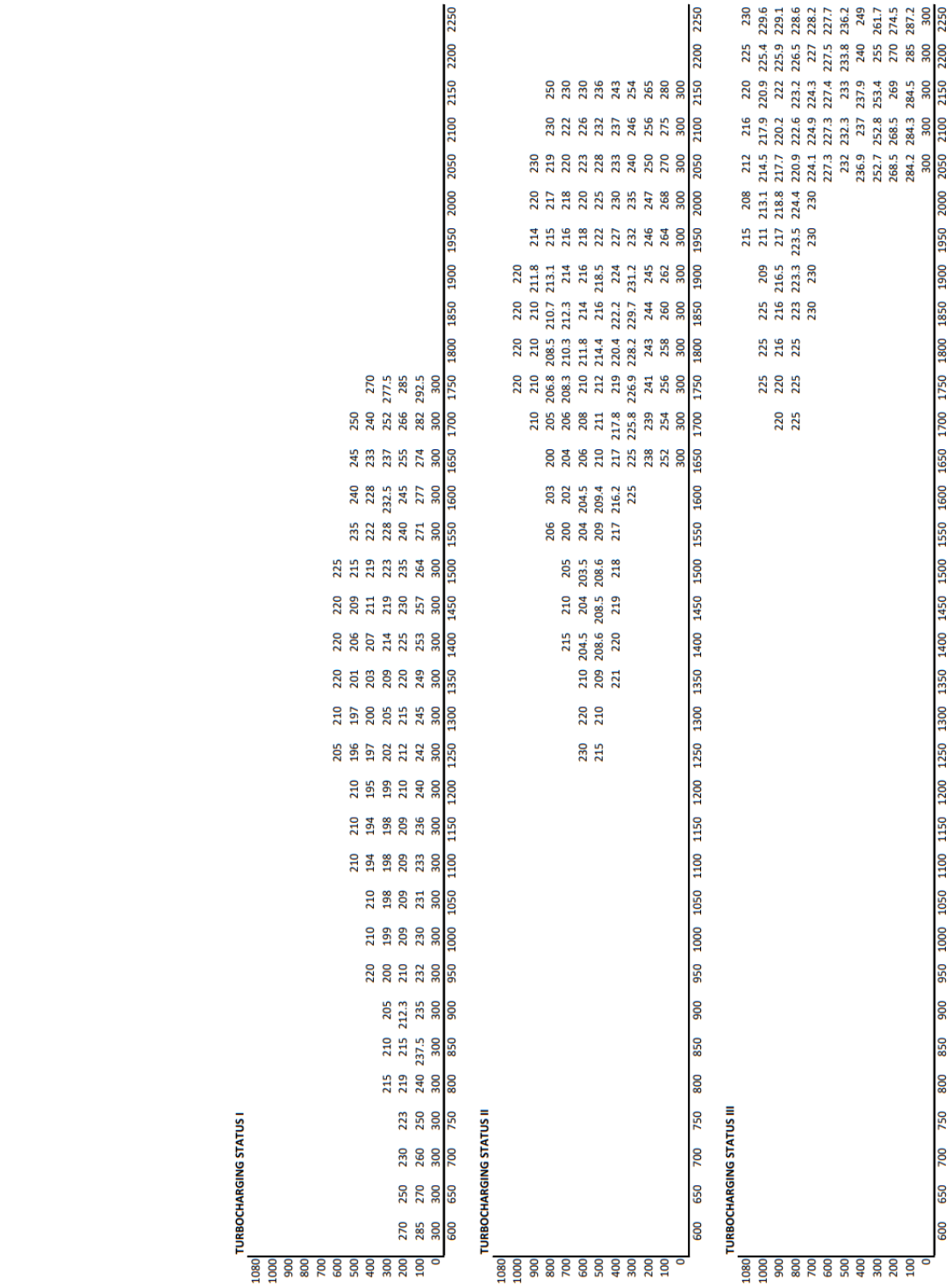

C.2 Fixed Speed SFC Data

Load [%]	SFC [g/kWh]
0.00	380
0.05	340
0.10	310
0.15	290
0.20	274
0.25	260
0.30	248
0.40	230
0.50	215
0.60	205
0.75	194
0.82	190
0.95	200
1.00	215

C.3 Specific Hydrogen Consumption

Load [%]	SHC [g/kWh]	Load [%]	SHC [g/kWh]	Load [%]	SHC [g/kWh]
0.000	0.1521	0.319	0.5338	0.847	0.4696
0.024	0.3522	0.339	0.5335	0.861	0.4665
0.030	0.3909	0.359	0.5327	0.874	0.4625
0.033	0.4053	0.379	0.5317	0.887	0.4586
0.038	0.4317	0.398	0.5305	0.899	0.4544
0.043	0.4501	0.437	0.5280	0.911	0.4503
0.048	0.4672	0.456	0.5263	0.922	0.4459
0.054	0.4808	0.475	0.5241	0.933	0.4417
0.061	0.4916	0.549	0.5155	0.943	0.4373
0.078	0.5072	0.568	0.5134	0.952	0.4327
0.101	0.5173	0.586	0.5111	0.961	0.4283
0.124	0.5225	0.639	0.5039	0.969	0.4234
0.147	0.5261	0.674	0.4987	0.976	0.4186
0.170	0.5284	0.707	0.4937	0.982	0.4135
0.192	0.5300	0.724	0.4912	0.988	0.4080
0.214	0.5312	0.757	0.4861	0.992	0.4025
0.235	0.5323	0.772	0.4835	0.996	0.3970
0.256	0.5332	0.788	0.4810	0.998	0.3911
0.277	0.5338	0.818	0.4754	1.000	0.3868
0.298	0.5338	0.833	0.4727		

Brynhild Resell Igland

Low- and Zero-Emission Hybrid-Electric Power Systems for Passenger Ferries

NTNU
Norwegian University of
Science and Technology